LBL-12883

Lawrence Berkeley Laboratory
UNIVERSITY OF CALIFORNIA

To be published as a book chapter in Heavy Ion Science,
Plenum Press, New York, 1982

STREAMER CHAMBERS FOR HEAVY IONS

Karl Van Bibber and Andres Sandoval

June 1981

NUCLEAR SCIENCE DIVISION

Prepared for the U.S. Department of Energy under Contract W-7405-ENG-48

DISCLAIMER

STREAMER CHAMBERS FOR HEAVY IONS

Karl Van Bibber
Department of Physics
Stanford University
Stanford, California 94305

and

Andres Sandoval
Gesellschaft für Schwerionenforschung, West Germany
and
Nuclear Science Division, Lawrence Berkeley Laboratory
University of California, Berkeley, CA 94720

This work was supported by the Director, Office of Energy Research, Division of Nuclear Physics of the Office of High Energy and Nuclear Physics of the U.S. Department of Energy under Contract W-7405-ENG-48 and the Bundesministerium für Forschung und Technologie, West Germany.

STREAMER CHAMBERS FOR HEAVY IONS

K. Van Bibber, A. Sandoval

1. INTRODUCTION

The history of visual track detectors is as old as the history of nuclear physics itself. Possessing a combination of assets and liabilities peculiar to each technique, visual detectors invariably figured among the first investigations in each new chapter of nuclear and particle physics and frequently made the most significant discoveries. The expansion cloud chamber enabled the discovery of the neutron in 1932, the muon five years later, and the first observations of strange particles in 1947. Such chambers were productive even in the era of modern high energy accelerators such as the Brookhaven Cosmotron in the early 1950s. Emulsion stacks identical to those used in the pioneering studies of cosmic rays in the upper atmosphere are used today in charmed particle decay studies and in investigations of projectile fragmentation systematics, where a potentially very significant mean-free-path anomaly has recently been reported (Fr 80, Fr 82). And without question, no advance in nuclear instrumentation has had such singular impact as the development of the hydrogen bubble chamber, whose accomplishments are too numerous to cite here. Small wonder then that visual techniques have so tenaciously resisted extinction in the face of the onslaught of the electronic revolution. They have yielded ground reluctantly, only to reappear in hybrid experiments and rejuvenated by technical innovation.

Having appeared a decade afterwards, the streamer chamber has necessarily stood in the shadow of the bubble chamber, although it supplants the chief drawback of the bubble chamber, namely, its nonselectivity or lack of triggerability. A brief explanation is in order.

The application of an intense electric field of appropriate duration to a volume of gas through which a charged particle has passed can initiate the growth of luminous filament discharges from the sites of primary ionization along the particle trajectory. These luminous discharges, or streamers, can be sufficiently bright to be photographed directly without image intensification; furthermore, limiting the duration of the applied electric field permits restriction of the streamers to several millimeters or a few centimeters in length, measured along the direction of the field.

Visual track detectors that operate on this principle are termed streamer chambers. Such chambers afford 4π sensitivity, and the spatial localization of the streamers permits three-dimensional track reconstruction by parallax. As the distance between anode and cathode of a large volume chamber may be 30 cm or more, many times the length of an individual streamer, no direct spark channel between anode and cathode is formed. Consequently, unlike the spark chamber, no single track will cause the applied voltage to sag, and, therefore, the streamer chamber is capable of detecting events of arbitrarily high multiplicity with no diminution of light output. Events of up to 150 charged secondaries from the collision of relativistic heavy ions have been recorded at the Bevalac streamer chamber. Most importantly, an electric field may be applied within a few hundred nanoseconds of an event, which is short compared with the recombination time of electron-ion pairs and even with respect to the time that diffusion of primary electrons would seriously impair track localization. Thus, the streamer chamber has the excellent feature that it may be triggered by external detectors and events of interest preselected before recording.

These chambers are normally operated in a magnetic field parallel to the electric field and recording axis, and the magnetic rigidity of tracks thereby determined. Limited particle identification capability has been demonstrated by streamer density measurement, at least among lighter species ($Z \leqslant 3$). The utility of such a visual technique with rigidity measurement for identifying particles with a characteristic decay such as $\Lambda \rightarrow p^+ + \pi^-$ is evident.

Streamer chambers nevertheless have their shortcomings. Apart from the disadvantages of film recording and scanning, there is a practical data-taking limitation of a few events per second beyond which the pulsed high voltage supply, normally a Marx generator, invites difficulty. If the beam traverses the active volume of the chamber, the beam flux is limited by the memory time of the chamber; this flux in the best of cases is $\leqslant 5 \times 10^5\ s^{-1}$. In excess of that limit, every event will invariably be accompanied by unwanted beam tracks. Solid targets within the active volume must be nonconducting or encapsulated in a nonsensitive atmosphere. Last, the passage of the beam and secondaries through the chamber windows, gas, and target imposes a lower limit on incident energy for heavy ion work. Roughly one may estimate this to be 10 MeV/nucleon without taking exceptional measures to reduce energy loss. It should be noted that operation at these low energies requires targets comparable in thickness with the remainder of material along the beam path; otherwise, the fraction of events occurring in the target may become unacceptably small compared with that of interactions in the gas or windows.

1.1. Development of the Streamer Chamber

Not surprisingly, the streamer chamber was the child of high energy physics, specifically an outgrowth of wide-gap spark chamber work. In the case of the wide-gap spark chamber, the electric field is chosen to be parallel to the anticipated trajectory, as it is observed that for a particle whose angle of inclination to the field is not too great (within 45° or so), the spark channel follows the trajectory and not the shortest path between anode and cathode. By the mid-1960s it had been realized that isotropic localization of tracks was possible even for trajectories perpendicular to the applied field, not because of the coalescence of initial avalanches as in the case of the wide-gap spark chamber but rather by stringent control of streamer growth to very short distances. This initial demonstration, as well as much subsequent theoretical and experimental work on streamer formation, was Russian (Ch 63, Ch 64, Do 64).

By the early 1970s, large volume chambers on the order of $0.5 \times 1.0 \times 2.0\ m^3$ were engaged in large-scale data production experiments at most high energy physics facilities around the world, both in fixed target mode (Wa 72, He 75) as well as in colliding-beam experiments, where the streamer chamber must surround the evacuated intersection region (Eg 75). More recently in the field of elementary particle physics, a miniature chamber of novel design has been employed by the Yale group at FNAL to study the decay of charmed particles (Sa 78). Operating with ultrashort high-voltage pulses and extremely high gas pressures permits few micron spatial resolution, which, coupled with a favorable Lorentz factor, makes lifetimes on the order of 10^{-14} seconds accessible in this experiment.

The applications of streamer chamber technology in nuclear science have been more limited. Extremely low count rate experiments frequently motivate the use of a visual technique, particularly if the events possess a characteristic "signature" and electronic coincidence experiments would not be feasible because of background processes. A streamer chamber was employed for this reason in establishing strict upper limits on the rate of double β^- decay of ^{48}Ca (Ba 67, Ul 68), whereas many previous coincidence experiments proved inconclusive. Perhaps the first in-beam application in nuclear physics was the study of the p-^{4}He analyzing power at 800 MeV where helium gas served both as the target and chamber gas; 620,000 pictures were taken in this experiment (St 69).

Nevertheless, a large-scale program in nuclear science did not begin until both an existing streamer chamber and a high energy physics accelerator--the Bevatron--were relinquished by the high energy community. Since the conversion of the accelerator in 1972 to the production of relativistic heavy ion beams--now termed the Bevalac in conjunction with the SuperHILAC injector--more than 900,000 photographs have been taken of nucleus-nucleus collisions with beams of p, ^{4}He, ^{12}C, ^{15}N, ^{20}Ne, ^{40}Ar, and ^{40}Ca from 30-2100 MeV/nucleon. A preliminary review of that work appeared in 1979 (Sc 79). A similar program has been carried out at the SKM-200 2 m streamer chamber at Dubna.

Within the past four years, the feasibility of streamer chambers for heavy ion reaction studies at lower energies ($\leqslant$35 MeV/nucleon) has been demonstrated at the Berkeley 88" cyclotron. This work has been directed towards the development of a hybrid chamber that combines the best features of solid state detectors, event-mode data collection, and visual track recording, and the first production experiments have been completed only within the past year.

1.2. Relevant Aspects of Streamer Formation

The study of avalanche growth, transition to streamer propagation, and eventual formation of a spark discharge is a rich one in its own right, containing a whole complement of atomic and electromagnetic phenomena in a plasma. The interest in these chambers as tools of particle and nuclear science, particularly for differing needs and constraints, has in part prompted a vigorous theoretical and experimental study of streamers in various gases, although some details of their formation still elude us.

Fairly recent comprehensive summaries of these topics do exist, and the work of Rice-Evans we mention in particular as an excellent reference source for the atomic physics involved in electron multiplication in gases and streamer chambers in general (Ri 74). We will not attempt such a broad treatment here but only underline those features of streamer growth that are relevant to understanding the advantages and shortcomings of operating in the streamer regime.

When a charged particle traverses a volume of gas, it loses energy principally by ionization and leaves a trail of electron-ion pairs, which in noble gases represent roughly 30 eV of energy loss each. The electrons and ions will diffuse away from the trajectory but without acceleration in an external electric field will eventually recombine. In gases of sufficient purity, however, the recombination time may be hundreds of microseconds, much longer than necessary for external detectors and conventional electronics to determine that such a charged particle may represent a potentially interesting event. Clearly the diffusion process imposes a much stricter limitation on the delay time permitted before application of an electric field to initiate an electron avalanche in order that the electrons still retain a tolerable proximity to the initial track. As a rule of thumb, the overall delay time between event and high voltage pulse should be no more than a few microseconds. A practical consideration is the reduction of the memory time of the chamber gas to match this value approximately and thus to maximize the acceptable beam rate. Normally, this is accomplished by the admixture of a few parts per million of an electronegative gas such as SF_6.

The requisite field strength for neon-helium chambers at atmospheric pressure is 10-20 kV/cm. While studies have been made of streamers formed by microwaves or laser pulses of suitable intensity (Wa 72), it is fair to say that for all chambers involved in data production in particle and nuclear work, the high voltage source is invariably a Marx generator and Blumlein transmission line terminated in the cathode and anode sandwiching the gas volume. In such an electric field, each free electron gives rise to an avalanche well described by an exponential growth in distance,

$$n = e^{\alpha x} \tag{1}$$

and traveling with the electron drift velocity. Here α is the Townsend first ionization coefficient. While simple considerations predict its behavior to be given in closed form,

$$\alpha/p = Ae^{-B/(E/p)} \quad , \tag{2}$$

where E is the electric field strength and p the gas pressure, it is sufficient for our purposes to note only that α/p is a steeply rising function of E/p over the range relevant for practical chamber operation. The positive ions left behind may be considered to be stationary, at least in the short time scale.

Assuming that the cathode and anode are sufficiently far apart, the exponential growth of equation (1) dictates that at some point the internal space charge field of the avalanche will cancel the applied field and the multiplication will cease, the distance in which this will occur is roughly in inverse proportion to α. At this stage, the total separated charge may be only $\approx 10^7$ free electrons, too few to produce a photographic image without an image intensifier.

It is useful to consider that the space charge field of the avalanche will be essentially dipole in character. Such a field will cause nearly perfect cancellation of the applied field inside the avalanche and lateral to it but--and this is the important feature of streamer growth--a considerable enhancement of the applied field at the head and tail of the avalanche. Partial recombination of electrons and ions at this time will cause the emission of ultraviolet photons, some few of which will escape reabsorption inside the plasma. Because of the strong dependence of α on E, the resulting photoelectrons in the neighboring gas lateral to the original avalanche will have virtually no probability of initiating secondary avalanches, whereas those liberated at the extremities of the original avalanche will give rise to secondary avalanches that will grow with even greater velocity. These in turn after space charge arrest will generate tertiary avalanches, always along the direction of the applied field, and the simultaneous growth of the discharge in both directions by the photoionization process is termed streamer propagation. By the termination of this process the velocity of the streamer may reach a tenth of the speed of light.

If the streamer has grown to a length of more than a few millimeters, the light output should be sufficient to produce a photographic image without image intensification. A schematic view of a track is shown in Fig. 1, both along the direction of the field where the trajectory is delineated by a series of bright points, and perpendicular to the applied field, which has the appearance of a luminous ribbon. (Streamers in neon are easily visible to the naked eye and are orange-red in color.) For discharges on the order of one centimeter in length, two or more views along the direction of the electric field and separated by 15° or so provide adequate parallax to reconstruct the three-dimensional trajectory.

But there is a severe price to be paid for brightness. Three factors conspire to make streamer growth among neighboring sites a highly competitive process: the statistical nature of ultraviolet photon emission, the enormous acceleration of secondary and tertiary avalanches, and the large space charge fields of developing streamers. The result is a suppressed dependence of streamer density with initial ionization, exemplified by the observation that of the 40 initial electron-ion pairs created per centimeter in neon gas at one atmosphere pressure by a minimum ionizing particle, on the average only 2.5 will develop into streamers. As a consequence, streamer density is not proportional to Z^2 and particle identification thus becomes problematic.

While particle discrimination is routinely performed between protons and pions in relativistic heavy ion studies, clearly some different scheme will be necessary for the more general case. The most realistic option is to operate such a chamber in the avalanche regime where space charge effects will be far less important, and in fact the absolute correspondence of avalanche sites and primary electrons has already been demonstrated for minimum ionizing particles (Da 69). This mode of operation should result in the additional benefit of a considerable reduction of "flaring", a phenomenon that will be discussed in section 2.1.

2. STREAMER CHAMBERS IN RELATIVISTIC HEAVY IONS

2.1. The Bevalac 1.2 m Streamer Chamber

2.1.1. Physical Description and Operation

The streamer chamber facility at the Bevalac was built in 1970 as a joint project between UCLA and LBL to study π^- and K^- induced reactions on hydrogen (Gr 72). In 1974 it was used for the first time to explore the interactions of relativistic heavy ions. Since then, more than 900,000 pictures have been taken with beams from protons to ^{40}Ca, energies between 30 MeV/nucleon and 2.1 GeV/nucleon and targets with masses between Li and Pb.

The streamer chamber facility consists of the beam transport line, the chamber body, a dipole magnet in which the chamber is placed, a high voltage Marx generator, a main spark gap, and a Blumlein for shaping the high voltage pulse applied to the chamber, a recirculating and purifying gas system, a set of three 35 mm cameras which record the event, and a series of beam defining and trigger counters and their electronics.

The beam transport system consists of the usual dipole on quadrupole magnets with the peculiarity of having two pitching dipole magnets with opposite polarities right in front of the streamer chamber magnet. This allows one to bring the beam into the chamber at any desired angle, which is necessary in order to focus the beam through trigger scintillators and the target, placed inside the streamer chamber magnet, which is kept at a constant field of 1.32 T irrespective of the beam rigidity.

The chamber itself is a double streamer chamber with a central high voltage electrode and a sensitive volume of 120 cm long x 60 cm high x (2 x 20 cm) deep (Figure 2).

The chamber body is made of epoxy sealed polyurethane foam, which provides sufficient mechanical rigidity and yet has very low mass in order to minimize the secondary interactions in it. The back plane is made of anodized aluminum, and the high voltage electrode in the center of the chamber and the front electrode are made of a 0.22 mm stainless steel wire mesh. The front window, through which the events are photographed, is made of 9 μm mylar.

The whole chamber fits into the gap of a dipole magnet that has both pole pieces removed, one for photography, the other for access to the back plane through which the targets and trigger scintillators are inserted. The dipole produces a 1.32 T field normal to the center electrode, with maximum inhomogeneities of 10% in the chamber volume. The three field components have been mapped and fitted to a 29th order polynomial, which gives typical r.m.s. errors of the order of 10 gauss.

The high-voltage pulsing system consists of a 2 stage Premarx and a 12 stage Marx generator, which provide pulses up to 720 kV (Figure 3). The Premarx and Marx spark gaps are placed in a single column with N_2 insulation at pressures between 12 and 20 psi. The column and capacitors are immersed in transformer oil for insulation. The Premarx is triggered by an 8 kV hydrogen tyratron pulser and the capacitors are charged by ±30 kV regulated power supplies. The main spark gap, which is fed by the Marx generator, controls the actual voltage of the pulse applied to the chamber by variations of the spark gap distance and the pressure of the SF_6 in which it is contained. The output pulse of the main spark gap is shaped with a Blumlein transmission line, which allows the pulse length to be varied between 5 and 15 ns (Figure 4).

The streamer chamber gas used is 90% Ne, 10% He and of the order of 30 ppm SF_6 used as poisoning gas to reduce the memory time to 2 μs. The gas is being recirculated and purified with a liquid nitrogen trap and molecular sieves.

The events are photographed with three 35 mm Flight Research cameras, which are provided with 40-mm lenses and have no shutter. The cameras are positioned with a 15° stereo angle between lenses. A Kodak SO-143 emulsion on an antihalating base is used on all three cameras and is spray developed to have a high contrast.

The nonconducting targets are mounted on lucite frames and inserted in the back half of the chamber. Compounds like LiH, NaF, KCl, BaI_2, Pb_3O_4 have been used. Metallic targets have been used inside a plastic bag in air, which prevents sparking. Targets of Ca and Pb have been used.

In the trigger system (Figure 5) the beam signal is defined by the coincidence between two 150 μm Si surface barrier solid state detectors outside of the chamber (S1, S2) and a 75 μm plastic scintillator (S3) inside the chamber 5 cm upstream from the target. These are in anticoincidence with a plastic scintillator (C) collimator with a 1.2 cm diameter hole in front of the Si detectors. The trigger scintillator (T) is placed 27.8 cm downstream of the target and is used to trigger on events by performing an anticoincidence with a valid beam signal for all pulse heights above a certain threshold. Thus reactions are recorded only for energy deposition in the downstream scintillator falling below a predetermined level. By varying the threshold of the T pulse height at which events are rejected, one can vary the trigger bias from unbiased (threshold above the beam pulse height), to minimum bias (threshold just below the beam pulse height), to central trigger (threshold at ∿10% of beam pulse height) (Figure 6). A summary of the chamber characteristics are given in Table 1.

Under normal running conditions, 600 ns after the event occurs the trigger logic decides if the event is to be taken and, in this case, a pulse is applied to trigger the Marx generator. Approximately 700 ns later a 700 kV, 10 ns long negative pulse is applied to the central electrode. This pulse travels through the chamber and is absorbed at the end by the terminator resistors that are matched to the chamber impedance. During the traversal time of the high voltage pulse, the primary ionization is amplified by a factor of 10^9 as it develops from a Townsend avalanche in streamer formation through the photoionization mechanism. The streamers can only grow along the direction of the electric field (perpendicular to the central electrode) producing along the track of an ionizing particle a ribbon of light, 1 mm in profile and ∿1 cm in width. As the magnetic field is parallel to the electric field, even high energy delta rays are curled into tiny helices along the magnetic field lines. The streamer light decays in ∿3 μs and is recorded by the cameras that view the streamers in profile to obtain the best spatial resolution. The roll and frame number and other fiducial lights are flashed 3 ms later, and the cameras advance the film after 50 ms. The Marx generator is recharged and thus 250 ms after an event the system is ready to record the next.

There are two types of tracks that can appear in an event: the normal ones that are formed by isolated streamers that extend along the field direction and the bridging ones that correspond to particles emitted from the target along the electric field lines towards the cameras crossing the central and the front electrode. For these, the streamers are fused into each other forming an ionization channel through which a spark develops. This makes them a factor of thousand brighter than the normal tracks and correspond to the short bright stubs around the target (Figure 6c). The region in which these bridging tracks form corresponds to a cone from the target to the cameras with an opening angle of 20°.

Another effect that is often seen in the picture is flaring. These are the very bright light patches that sometimes appear along a track, mainly downstream of the target, saturating the film. These appear when the charged particle hits a wire of the central electrode producing a shower of electrons. Figure 7 shows such a flare as it is seen with no confining magnetic field.

2.1.2. Film Scanning, Measuring and Track Reconstruction

Once the events have been recorded and the film developed, the film is first scanned to determine the event topology, counting the number of tracks produced and classifying them into different categories. Such a classification is made according to charge sign, curvature, projected emission angle and occurrence of secondary processes like γ conversion, neutral strange particle decays and secondary interactions. This work is done by scanners who project each view of the event onto a scanning table (Figure 8).

After scanning, events are selected to be measured in order to do a three dimensional track reconstruction to extract momenta and emission angles.

A charged particle describes a helical trajectory in the chamber volume apart from inhomogeneities of the magneticfield and energy loss in the gas. The pitch angle of the helix, also called the dip angle, is given by the angle of the track to the plane normal to the magnetic field (Figure 9). The principle of space reconstruction is based on the fact that each camera records the track in a different projection relative to space fixed fiducial marks. If one measures the projection of one point on two different views, the intersection of the rays from the projected point to the camera gives the point's coordinates in space as seen in Figure 9.

In order to obtain the coordinates on film of any point, one can use an image plane digitizer, which has been developed to digitize bubble chamber film (Figure 10). In this digitizer the operator manually positions the film on the point that she wishes to digitize with an accuracy of 1 μm on the film plane. The coordinates of the digitized point are stored on magnetic tape for further analysis.

In order to reconstruct an event, the following procedure is used:

A) A complete set of fiducials, positioned in the front and the back of the chamber, is carefully measured five times for each view. From this, the mean and standard deviation of the fiducial coordinates on film are extracted, which are used to determine the optical constants of each camera.

B) For each event to be measured the scanner first matches the tracks in the three views so as to measure them in the same order. For each view she then measures a set of four fiducial marks in order to establish a reference frame and then measures the selected tracks in the order established by the match procedure. For each track, the measurement starts from the point nearest to the vertex and digitizing on the average 12 to 20 points along the track. A computer drawing of such a measured event is shown in Figure 11.

C) Once all the tracks are measured in all three views and the coordinates written on tape, this data tape is analyzed by the Three View Reconstruction Program (TVGP) (So 65). Using the optical constants it corrects distortions and transforms the measurements to an ideal plane. From this it generates space points which approximate the true space points of the trajectory. Then, assuming a particular mass of the particle, a space curve is fitted to these points, incorporating the magnetic field variations and the energy loss in the gas. From this, physically interesting quantities, momentum, azimuth and dip angles are calculated for points at the beginning, middle and end of the measured track. For each of these steps a full error analysis is performed, including the effects of multiple scattering.

D) Due to the high track density aound the vertex, most tracks are measured beginning several centimeters from the vertex. It is therefore necessary to extrapolate the tracks back and to determine the point of intersection and recalculate the momentum and emission angles of all the tracks at the vertex, taking into account the energy loss in the target. This procedure and the kinematical fitting to the event topology are performed by the programs SQUAW and Apache (Da 68).

Typical values of the resolution obtainable for different parameters are given in Table II. The final results of the reconstruction are the four-momenta of the measured tracks and their errors. As an example, Figure 12 shows the projections of the particles' momenta in the laboratory corresponding to the event measured in Figure 11. It is a central interaction of ^{40}Ar on KCl at 1.8 GeV/nucleon. The measured momenta can then be transformed to the center of mass frame. In Figure 13 the same event is transformed to the center of mass rapidity and transverse momentum space. The rapidity,

$$Y = \frac{1}{2} \, \mathrm{Ln} \, \frac{E+p_{||}}{E-p_{||}} \quad , \qquad (3)$$

corresponds to the Lorentz invariant velocity. One may then analyze the charged particle exclusive final state of such a reaction, such as the event shape, two particle correlations, degree of thermalization, amount of energy converted into pions, etc. One must remember, however, that about half of the emitted particles, the neutrals, are not detected by the streamer chamber.

2.1.3. Physics

2.1.3a. Study of π^- Production

There is considerable interest in studying pion production and its energy dependence in heavy-ion central collisions. The pions, consisting of a quark antiquark pair, are produced in proton-proton collisions from threshold up to 2 GeV mainly from the decay of the $\Delta(3,3)$ isobar and in a lesser extent from N* production and decay. In the collision of two heavy ions a region of high density, high temperature and large baryon number is formed in which a fraction of the available energy will be converted into matter as Δ's, N*'s and pions. Is the mechanism that transforms the energy into mass in proton-proton collisions the same as in a nucleus-nucleus collision? Are there other effects of a collective nature coming into play? Does the distortion of the vacuum in the high density stage affect the reaction mechanism? What are the properties of a nuclear system with a large percentage of isobars? Can the Δ-Δ interaction be studied in such a system? Are the pions produced only through resonances or can they be created out of the thermal bath as $\pi^+\pi^-$ or $\pi^o\pi^o$ pairs? What is the maximum density and temperature attainable in such a collision? From the study of the pion multiplicity distributions at various energies thermal and cascade models can be tested (Gy 78, Va 78, Ya 79, Mo 79). Also if there is a transition from normal nuclear matter to a pion condensate it might be reflected on the pion yield (St 79).

A first step to try to answer some of these questions has been done by doing a systematic study of π^- production and accompanying nuclear disintegration in the interaction of ^{40}Ar + KCl for bombarding energies from 0.4-1.8 GeV/nucleon. The experiment was performed at the Bevalac using the streamer chamber facility. A near-equal mass projectile and target system was chosen in order to provide a well-defined center of mass and to minimize absorption effects due to cold spectator matter. A nonconducting 3 mm thick KCl target was placed inside the sensitive volume of the chamber permitting 4π exclusive charged particle detection and charge-sign and rigidity determination in a 1.32 T magnetic field.

The streamer chamber trigger technique, developed by Fung et al. (Fu 78) consisting of a beam defining counter-target-downstream scintillator configuration was used. The downstream counter, placed 27.8 cm from the target with a solid angle of 74 msr, was used to detect the projectile spectator fragments. Data were taken at each energy in two trigger modes: an inelastic mode that rejected the noninteracting beam particles and a central mode that selected events with small total charge in leading fragments compared to that of the beam. For each trigger mode 2000 to 5000 events were accumulated at bombarding energies at the target center of 360, 566, 772, 977, 1180, 1385, 1609, and 1808 MeV/nucleon. Each event was classified according to its negative pion multiplicity, total charged particle multiplicity, and number of leading tracks.

Total charged particle (n_{tot}) and negative pion (n_{π^-}) multiplicity distributions are shown in Figure 14 for both trigger configurations at 1.8 GeV/nucleon. For the inelastic trigger, the partial cross section of events with a given multiplicity $\sigma(n_{tot})$ decreases exponentially for low multiplicities and reaches a plateau for $25 < n_{tot} < 40$, which is followed by a sharp cut off at higher multiplicities. The observed shoulder at high multiplicities, which appears at all bombarding energies, is not reproduced by the fireball (Go 78) or cascade (Ya 79, Cu 80) models. In the fireball model this may be ascribed to the clean cut geometry, which neglects dissipation of momentum and energy along the transverse direction, underestimating the number of participants.

The total cross section observed for the inelastic trigger is $\sigma = 1.78 \pm 0.03$ b. The effect of the trigger bias, which suppresses events with charge multiplicities $n_{tot} \leqslant 5$, is estimated to be a 6% correction yielding $\sigma_R = 1.9 \pm 0.1$ b. This value agrees well with a geometrical reaction cross section that fits the systematics of the available experimental data. The central trigger mode was used to enrich the sample of high multiplicity events. The resulting n_{tot} distributions are Gaussian as shown in Figure 14. The total cross section observed for the central trigger is $\sigma_C = 180 \pm 5$ mb, which corresponds to $b \leqslant 2.4$ fm in the geometrical model. In order to maintain the same range of impact parameters for the study of the energy dependence of central collisions, the trigger bias was adjusted to maintain a constant cross section at all bombarding energies.

A detailed examination of the correlation between n_{π^-} and n_{tot} provides a more exclusive picture of the interaction. Figure 15 shows a contour plot of the reaction cross section as a function of n_{π^-} and n_{tot} in the inelastic trigger mode. The reaction products are confined to a smooth distribution about a narrow ridge with no discernible signature of anomalous pion production. The dash-dot curve, representing $\langle n_{\pi^-} \rangle$ as a function of n_{tot} shows a monotonic increase with no discontinuities, a feature common to the other bombarding energies. For high multiplicities, the interaction approaches the total disintegration limit, which correponds to the maximum number of observable charges; in this case,

$$n_{tot}^{max} = \overline{Z}(Ar) + Z(K \text{ or } Cl) + 2n_{\pi^-} \quad , \tag{4}$$

which is given by the straight lines in Figure 15.

In addition to the mean, considerable information is contained in the dispersions of these distributions. However, the correlation between n_{tot} and n_{π^-} is not directly suitable for theoretical analysis. Instead, a correlation in terms of the number of participant nucleons is more appropriate. From the streamer chamber data, a good estimate of the number of projectile and target participant protons (Q) can be obtained. The participants may be defined as all nucleons outside the projectile and target fragmentation Fermi spheres (Hü 77). To estimate the number of participant charged nuclei in each collision, the charges created ($2\ n_{\pi^-}$) and the number of observed projectile (n^s_{proj}) and target (n^s_{tgt}) spectator fragments were subtracted from n_{tot}:

$$Q = n_{tot} - 2n_{\pi^-} - (n^s_{proj} + n^s_{tgt}) \quad , \tag{5}$$

where n^s_{proj} is the number of leading fragments traveling with the projectile velocity in a 4° forward cone and n^s_{tgt} is the number of positive tracks observed with $p_{lab} \leqslant 200$ MeV/c. The resultant Q is identified as the number of participant protons, assuming that all these participant nuclei are singly charged. In Figure 16 the data of Figure 15 are transformed into the n_{π^-} vs Q space. As shown by the dots in Figure 16, the mean π^- multiplicity $\langle n_{\pi^-}(Q)\rangle$ increases linearly with Q. Such a linear dependence of $\langle n_{\pi^-}(Q)\rangle$ on Q is also found at all bombarding energies (Figure 17). The resulting π^- distributions are such that, for a given Q, the square of the dispersion is equal to the mean,

$$D^2_{\pi^-}(Q) = \langle n_{\pi^-}(Q)\rangle \quad , \tag{6}$$

as shown in Figure 16b. This extends the results of Bartke et al. (Ba 79) for central collisions to all impact parameters, if the distributions are classified according to the number of participants. There are two main contributions to these dispersions: (a) the dispersion in the number of negative pions produced in a N-N collision at the relevant energy and (b) the fluctuations of the number of pion-producing and absorbing interactions. It is observed that the elementary process (a) has a broader distribution, $D_{\pi^-} = \langle n_{\pi^-} \rangle$, broader than that from Poisson statistics alone (Ak 80). However, for heavy ion reactions at these energies the second contribution is the dominant factor. The observed Poisson distributions suggest that the fluctuations are statistical.

The excitation function for the central trigger was measured maintaining a constant $\sigma_c = 180$ mb. The results for the mean multiplicities and their dispersions are summarized in Table III. The mean number of participants $\langle Q \rangle$ is relatively constant above 800 MeV/nucleon, below which a decrease in $\langle Q \rangle$ is observed, most likely due to an increase in cluster formation. The mean pion multiplicities $\langle n_{\pi^-} \rangle$ are shown in Figure 18 as a function of the c.m. energy/nucleon. A linear dependence of $\langle n_{\pi^-} \rangle$ with the c.m. energy is observed above 150 MeV/nucleon, but there is no evidence of a discontinuity in the excitation function that could be ascribed to a phase transition.

2.1.3b. Two Pion Correlation Measurement

A group from the University of California Riverside has made unique contributions in triggered streamer chamber studies of relativistic heavy ion collisions at the Bevalac for several years. The preliminary work of this group focused on topological studies of charged particle multiplicities and negative pion yield and transverse momenta as a function of trigger mode, projectile and target mass, and beam energy. More recently, they reported the first observation of the Hanbury-Brown-Twiss effect (intensity interferometry) in the production of identical pions and thus made inferences concerning the space-time structure of the pion-emitting source.

The tracks of negative pions (easily distinguished from electrons) were measured on Micrometric scanner-digitizer tables, and the geometric reconstruction performed with a One View Fitting Program (OVFP), a modified version of TVGP. In the OVFP, depth information on any particle is obtained by observation of the track endpoint on the walls of the fiducial volume. The resolution achieved with this procedure is better than 1° in polar angle, 3°-5° in azimuthal angle, and under 10% in momentum, averaged over all angles.

As suggested by Kopylov, the signature of pion interferometry would be evident in the normalized ratio of the number of pairs of identical pions from the same event to the number of pairs of identical pions from different events, as a function of their relative momentum $q = |p_i - p_k|$ and energy difference $q_0 = |E_i - E_k|$ (Ko 73, Ko 74). Figure 19 displays the first data that conclusively showed this effect, for incident ^{40}Ar at 1.8 GeV/nucleon, with targets of BaI_2 (inelastic triggering mode) and Pb_3O_4 (inelastic, central triggering modes) (Fu 78a). In all three cases, a clear peak is seen at low relative pion momenta, manifesting the statistics of identical bosons.

Although the existence of the effect is clearly established, the extraction of physical parameters of the pion-emitting source depends on the shape and magnitude of the correlation function at low q, through the specific assumptions made about the source. For example, Yano and Koonin derive the following form for the case of a Gaussian space-time distribution:

$$R^{S--}_{D--} = K \left\{ 1 + \exp\left[-\left(\frac{\tau^2 q_0^2}{2}\right) - \left(\frac{r_0^2 q^2}{2}\right) \right] \right\} , \qquad (7)$$

where r_0 and τ are its characteristic space-time parameters and K an arbitrary normalization constant (Ya 78). Coulomb final state interactions between the two pions and the pions and the spectator nucleons undoubtedly modify any such analysis; nevertheless, straightforward fitting of the data with two such models suggested a source radius on the order of 3-4 fm.

Since the original report, the experimental situation has been refined by the accumulation of greater statistics, thus allowing a subdivision of the data according to pion multiplicity. It was hypothesized that the number of pions emitted in any event may provide a more direct measure of the centrality of the collision or the volume of overlap between the projectile and target nucleons, even after selection of events according to energy deposition in the downstream detector. This hypothesis was tested by repeating the correlation analysis for each set of data corresponding to a particular range of pion multiplicity, and the results are summarized in Table IV. The qualitative trend is as predicted, the radius parameter varying from 3.1 fm to 5.6 fm as the pion multiplicity varies from 2 to 15 per event (Lu 81). Keeping in mind the previous comments concerning the modifications imposed by final state interactions, the comparison with a strict Thermodynamic Fireball Model (TFM) is not at all satisfactory, unless the "freeze-out density", ρ_c (the density at which the particles in thermodynamic equilibrium are permitted to be observed asymptotically without further interaction) is increased from one-third to one times normal nuclear density.

2.1.3c. Strange Particle Production

In the study of high energy nucleus-nucleus collisions it is difficult to extract information about the initial stage of the reaction where high baryon densities may occur. Studies of nucleon and cluster emission (Sa 80a) are consistent with a development towards chemical equilibrium in the final stages of the reaction preempting information about the primary stages. Λ production near threshold is expected to occur either in the first generations of binary nucleon nucleon collisions or from a localized collective high temperature, high density system and, in any case, to reflect the first stages of the interaction. Although rescattering of particles in the nuclear medium is expected to be important, the absorption of Λ's is minimal. Therefore, the study of Λ production would provide a new way to examine the interpenetration phase of nucleus-nucleus collisions.

Strange baryon production near threshold in nucleus-nucleus collisions is interesting since it provides an opportunity to test the effect of an extended nuclear field on the production mechanism (Bj 69). In the elementary $NN \rightarrow \Lambda KN$ process, a strange-antistrange quark pair must be produced from the sea (Ho 77). The existence of strange-antistrange quark admixtures in the nucleus (Gr 79, Va 79a) may enhance the strange baryon production near threshold.

Λ production was studied in central ^{40}Ar + KCl collisions at 1.8 GeV/nucleon incident energy using the streamer chamber at the Bevalac. The streamer chamber was operated in both inelastic and central trigger modes. The central trigger selects events with small total charge in projectile fragments. This trigger, which corresponds to 10% of the reaction cross section (σ_c = 1.8 b), is associated with impact parameters $b \leqslant 2.4$ fm in a geometric model. The open channels for production of strange particles in this energy regime are $NN \to \Lambda KN$ (1.58 GeV), $\to \Sigma KN$ (1.79 GeV), and $\to \Lambda KN\pi$ (1.96 GeV). Neutral strange particles were detected by their charged-particle decay in the active volume of the chamber ($K^\circ \to \pi^+\pi^-$, $\Lambda \to p\pi^-$) since their lifetimes are large enough to decay outside the primary vertex. The Σ° decays immediately into $\Lambda\gamma$ with 100% branching ratio and therefore cannot be differentiated from the directly produced Λ's. In Figure 20 an event is presented corresponding to a central interaction of an ^{40}Ar on KCl in which a Λ particle was produced that decayed 59.7 cm from the target into a proton and a π^-.

In this experiment the film was scanned for secondary vertices that could correspond to either

a) a gamma converting in the chamber
   $\gamma \to e^+e^-$

b) a K° decay
   $K^\circ \to \pi^+\pi^-$

c) a Λ decay
   $\Lambda \to p\pi^-$

d) a neutron interaction resulting in two observable tracks, a positive and a negative.

The events were measured and reconstructed and a 3-constraint kinematical fit was performed to the different possibilities. The gamma conversions can easily be isolated due to the 0° opening angle between e^+ and e^- and their invariant mass. The rest of the events are shown in Figure 21 in the invariant mass plane $M(p\pi^-)$ vs $M(\pi^+\pi^-)$, in which each event is represented by a dot corresponding to the calculated invariant mass if one assumes the pair is a $p\pi^-$ or a $\pi^+\pi^-$. One clearly sees the two distinct bands corresponding to the Λ and K° masses.

The detection efficiency is intrinsically a function of the branching ratio for charged particle decay, the momentum of the decaying neutral particle, its lifetime, and the fiducial volume of the detection apparatus. To eliminate efficiency problems due to the high track density near the primary reaction vertex, only neutrals decaying farther than 10 cm from the target center were accepted. The low number of K° decays observed is due to the mismatch between the effective fiducial volume of the chamber and the lifetimes of the K° ($c\tau$ = 2.68 cm) and K° ($c\tau$ = 1554 cm).

The identified Λ's are displayed in Figure 22 as a function of $p_{\parallel}$ and $p_{\perp}$ in the nucleus-nucleus c.m. system. The solid curve in Figure 22 represents the kinematic limit for Λ momenta produced in the elementary NN $\rightarrow \Lambda KN$ reaction at 1.8 GeV. Most of the Λ's are observed beyond the kinematical limit indicating the necessity to include Fermi motion and/or collective multiparticle interactions.

A calculation in which the Fermi distribution of the nucleons inside the projectile and target is considered fails to account for the large momenta of the Λ's, indicating that in their production there is more than independent nucleon-nucleon collisions.

A much more detailed information of the reaction mechanism can be obtained by measuring the Λ polarization.

Since the Λ decay is self-analyzing for polarization in the parity violating weak decay $\Lambda \rightarrow p\pi^-$, the distribution of decay protons in the frame relative to the Λ spin direction (Cu 73) is $dW/d\theta = (1 + \alpha P\cos\theta)/4\pi$ where P is the Λ polarization, $\alpha = -0.642$ (Br 78), and θ is the angle between the decay proton and the unit vector normal to the reaction plane.

Using the relation $\alpha P = \langle \cos\theta \rangle / \langle \cos^2\theta \rangle$ (Ba 79), the polarization extracted from the present experiment was found to be $P = -0.10 \pm 0.05$. A polarization has been observed at higher energies in p-p reactions. This polarization has been ascribed to the spin features of the SU(6) quark wavefunctions whereby the spin of the Λ is determined by that of the produced strange quark (Fa 79, He 78). The polarization is observed to increase with $p_\perp$ and has the same values for incident energies between 24-400 GeV. The small sample of Λs from this experiment does not allow for such an analysis.

2.1.4. Prospectus: Particle Identification and Direct Image Digitization

The streamer chamber provides a measurement of the magnetic rigidity for all charged particles emitted from the interaction; in order to obtain their four-momenta, their charge and mass have to be known. There is a large variety of particles that can be produced in relativistic heavy ion interactions. For negative particles these are e^-, μ^-, π^-, K^-, and $\bar{p}$. For positive particles the possibilities are much greater: e^+, μ^+, π^+, K^+, p, d, t, ^{3}He, α, etc., up to the charge and mass of the beam or heavy target recoil products. Fortunately, there is a very large difference in their yields in different regions of phase space. The majority of all the charged particles are protons. At 2.1 GeV/nucleon up to 15% will be π^+ with a mean laboratory momentum of 350 MeV/c. Most of the negative tracks are π^-'s with a small contamination of e^- at low momenta. The large majority of nuclear fragments, d, t, ^{3}He, α, etc., have beam velocity and correspond to projectile spectator fragments. With this great variety of particles in the momentum range from 50 MeV/c up to 4 GeV/c per charge, there is a very large dynamic range over which one would like to do particle identification (PI).

As mentioned previously (section 1.2) the mechanism of streamer formation seriously compromises particle identification capability, as streamer density is not simply proportional to primary ionization. Nevertheless, it is clear that there is information on particle charge and mass reflected in the intrinsic track characteristics. An extreme illustration of this is shown in Figure 23 in which a 50 MeV/nucleon ^{40}Ar enters the chamber and fragments into a p and a Cl. The Cl ion loses enough energy in the target and trigger scintillators to come to rest in the chamber gas, showing a very distinctive Bragg peak.

The particle identification information is contained in the distribution of streamers per unit length, in track brightness, and for high energy heavy ions in the number of energetic δ rays per unit length. A sketch of streamer profiles for different particles is shown in Figure 24. There are several complications in trying to use these features for particle identification. One has to consider the dip angle of the track since in a photograph one sees only a projection. For bridging tracks, those with a very large dip angle, one completely loses the particle identification information, since a spark channel is produced. Furthermore, one must consider the characteristics of the film on which the event is recorded: a lower cutoff in intensity, a logarithmic response, and a limited dynamic range with "blooming" at regions of saturation. Also the track properties are very sensitive to the time delay between the particle's traversal and the firing of the chamber, as well as to variations in the applied high voltage pulse. Nevertheless a trained scanner can differentiate e^- and π^- with $p \leq 100$ MeV/c and π^+ and p up to 800 MeV/c using streamer density.

In the analysis of intermediate energy interactions of ^{12}C and ^{40}Ar at energies between 30 MeV/nucleon and 100 MeV/nucleon, K. Wolf and R. Wehman have been using the ALICE facility at Argonne National Laboratory to do a computer-assisted densitometric study of the tracks. Using the integrated intensity per unit length as a criterion for events like Figure 25, they are able to obtain a very clean separation of p, d, t, α as is shown in the histogram in Figure 26. It is not proportional to Z^2 but the peaks are well separated. Work is in progress to determine over what range of fragments and momenta particle identification can be achieved.

A different approach to streamer chamber event recording is being tested and evaluated. This entails using directly digitized pictures instead of 35 mm film. The recent advances in the charged coupled device (CCD) technology has produced arrays of light-sensitive pixels (16,000 or more per array) with very good linearity and dynamic range, which can easily be digitized at video rates. An RCA-SID 52501 array consisting of 525 x 320 elements, each 30 μm x 30 μm in size (Figure 27) was used to evaluate this technique. An example of a directly digitized event is given in Figure 28, which shows a picture of an event displayed on a TV monitor. The event was imaged with a 25 mm lens with the diaphragm stop at f-2.8. The camera was triggered simultaneously with the event, and the charge on each pixel, proportional to the incident light at that location, was digitized into an 8 bit word and stored in a 160 K memory. The power of this approach can best be appreciated in Figure 29, which shows the same event as a three dimensional surface with the height proportional to the detected light intensity. Besides having the event in a form suitable for computer analysis, one sees the large difference in brightness and width of the tracks, which is hoped will be usable in the particle identification. A cut along a row is shown in Figure 30, illustrating the different brightness of the tracks. The techniques of imaging and digitizing CCD arrays is well developed to make this approach promising. The largest obstacle is the handling of this large amount of information. In the example shown each picture requires 1680008 bit words. For three views of an event with the necessary spatial resolution easily a million words per event will have to be analyzed. Large memories and multiprocessors are at hand to tackle this huge information flow, but a dedicated system will need to be designed.

2.2. The Dubna SKM-200 2 m Streamer Chamber

The 2 m streamer chamber (SKM-200) has been operational at the Dubna Synchrophasotron since 1973. The main purpose of the experiments carried out with the use of the SKM-200 chamber was the investigation of nucleus-nucleus interactions at relativistic energies. The possibility of registering all charged secondaries in a 4π geometry and triggering the streamer chamber for rare events makes the setup (Figure 31) an extremely useful tool for quasi-exclusive experiments, performed with high intensity beams of relativistic nuclei.

The fiducial volume (about 200 x 100 x 60 cm^3) of the streamer chamber is divided into two gaps of 30 cm each by a transparent high voltage electrode. The drive unit of the chamber consists of a Marx generator and a pulse-shaping transmission line that provides a high voltage output pulse of an amplitude up to 700 kV with a variable time duration of 7-13 ns.

The streamer chamber is filled with pure neon gas at atmospheric pressure; tracks of a sufficient quality are also obtained with helium gas filling the chamber. In the latter case, an increase of the high voltage amplitude up to 560-600 kV and of duration up to 12 ns is required. This is to be compared with 500 kV and 10.5 ns, respectively, used with the neon gas.

The chamber is placed in a magnetic field of 0.8 T and is viewed by three cameras, which allow stereoscopic recording of the registered events.

The solid targets, made in the form of thin disks (typically 0.2-0.4 g/cm^2) are mounted inside the fiducial volume of the chamber at a distance of 70 cm from the entrance wall. The following targets (A_T) have been used in the SKM-200 experiments performed so far: ^{6}Li, ^{7}Li, C, Al, Si, Cu, Zr, and Pb. The neon gas filling the chamber also served as a target.

Other gaseous targets (at pressures up to 6 atm) placed in a cylindrical mylar container, were also successfully tested inside the fiducial volume.

The SKM-200 setup was exposed to beams of relativistic nuclei (A_P), namely ^{4}He, ^{12}C, ^{16}O, and ^{20}Ne, accelerated in the Dubna Synchrophasotron to 4.5 GeV/c momentum per incident nucleon.

Two types of triggering systems have been used so far in the experiments in which nucleus-nucleus (A_P-A_T) interactions have been studied.

1. A trigger for inelastic A_P-A_T collisions provided registration of inelastic events occurring in the streamer chamber (in a solid target or in the neon gas). The triggering system consisted of two sets of scintillator dE/dx counters: an upstream counter telescope, selecting incident nuclei of a given charge Z_P and a downstream veto-counter telescope, covering a small solid angle (3.5 msr) and selecting events without projectile charged fragments of the same charge Z_P. Thus, the chamber was triggered whenever a Z_P primary entered the chamber but did not leave it.
2. A trigger for central A_P - A_T collisions consisted of the upstream dE/dx counters [the same as in the case (1)] and downstream veto-counters registering the absence of

   either (i) charged relativistic fragments of the projectile nucleus within a narrow forward cone

   or (ii) in addition to (i), neutron spectators of the projectile nucleus within a narrow forward cone.

Thus the system selected events with no charged fragments [version (i)] or no charged <u>and</u> no neutral fragments [version (ii)] of the incident nuclei.

The cut-off angle for the registration of fragments was (35-52) mr in most experiments performed up to now.

Such a selection of central collisions provided reasonable statistics of relatively rare events (down to less than 1% of the total reaction cross section in the case of ^{12}C-^{12}C collisions) and, moreover, the absence of projectile fragments seems to be a much more justifiable signature of central events than, for example, high multiplicity selection.

The pictures (Figure 32) obtained from the SKM-200 were scanned, and charged secondary tracks were measured with the use of semiautomatic measuring devices. The geometrical reconstruction of the measured data and analysis yielded momenta (p) and emission angles (θ) of the charged secondaries. A rough estimate of the ionization was also available from the visual inspection of the tracks. Typical values of the measurement errors for relativistic secondaries are $\Delta p/p \leqslant 2\%$-4%, depending on the momentum and the track length.

The technical data concerning the Dubna streamer chamber and first results of testing its operation were presented at the Frascati Conference in 1973 (Va 73).

The experiments that have been carried out with the SKM-200 chamber concerned mainly the three following lines of investigation of nucleus-nucleus interactions at 4.5 GeV/c momentum per incident nucleon.

A) Determination of the total cross sections for all inelastic interactions (He-A_T, C-A_T) and of the cross sections for various channels of ^{4}He fragmentation. Table V illustrates the possibility of separation of various fragmentation channels and consequently selection of nucleus-nucleus collisions with different values of impact parameter. Peripheral events are operationally defined as fragmentation in which at least two nucleons of the projectile have been observed. Central events correspond to interactions in which no charged fragments of the projectile have been observed.

B) The analysis of various characteristics of secondary π^- mesons, e.g., multiplicities (n), transverse momenta (p_T) and rapidities (y), and of their A_T dependence for central and peripheral $^4He-A_T$ collisions. Some of these results are shown in Figure 33, while a more detailed presentation and discussion of the results can be found in reference (Ak 80).

C) The analysis of the π^- multiplicity distributions in central collisions and comparison with those observed in p-p and A_p-A_T inelastic collisions. An illustration of these results is presented in Figure 34, where the dispersion of the multiplicity distribution is plotted against the average value of the π^- multiplicity (Ak 80).

3. STREAMER CHAMBERS FOR INTERMEDIATE ENERGY HEAVY IONS

3.1. The 88" Cyclotron Hybrid Streamer Chamber

The past five years have marked a period of active study of the continuum spectra of light and heavy particles emitted in the collision of heavy ions. Investigations of the energy dependence of isotopic yields, angular distributions, and energy spectra of complex ejectiles were vigorously pursued at several cyclotron laboratories capable of accelerating nuclei in the range of 10-20 MeV/nucleon, notably Berkeley, Texas A & M, Oak Ridge, and Maryland in the United States, and Groningen, Jülich, and Berlin in Europe. In parallel with this effort were the first experiments performed at the Bevalac and later at the CERN proton synchrotron extending the useful range of these machines downward in energy to the region of 100 MeV/nucleon. These two benchmark energies roughly encompass a number of characteristic energies or velocities of possible relevance to the nature of the nucleus-nucleus interaction: the speed of sound in nuclear matter, the Fermi energy, the pion production threshold, and the energy where projectile and target disengage in momentum space and thus where effects of Pauli exclusion should diminish in importance.

Although to date there is yet to be developed a consistent picture of what the existing data imply, it was evident rather early that reactions at 20 MeV/nucleon bore more than superficial resemblance to peripheral interactions at relativistic energies and were very likely characterized by multiparticle final states. Without prejudice to the discussion of the roles of "fast" and "slow" processes governing nucleon and complex particle emission, it is probable that the reaction mechanism at these energies is complicated. The frequently contrary indications that single particle inclusive and even coincidence measurements gave only served to underscore the need for the development of 4π detection capability.

This project began as a pilot study of the feasibility of such a visual technique for cyclotron work in 1977. An inspection of a sample of ^{16}O interactions in emulsion between 20 and 50 MeV/nucleon revealed a rich topology at these energies but also demonstrated the unsuitability of emulsions for any large program, for two principal reasons. The first difficulty is the precipitous decrease in residual range that heavy ions undergo in passing through emulsion below 100 MeV/nucleon. For ^{16}O at 100, 60, 30, and 20 MeV/nucleon, the ranges are 0.78, 0.32, 0.09, and 0.05 cm. Thus, the thickness of emulsion that defines even a gross selection of energy, for example, between 20 and 30 MeV/nucleon, represents only a miniscule fraction of a mean free path for an interaction of any kind, and it is easily estimated that the number of incident ions necessary to achieve a statistically meaningful body of data is excessive. Second, the total ionization and resulting track damage is too great below 100 MeV/nucleon, and element discrimination is considered unreliable even with range information. It would be unfair not to mention, however, that early survey experiments, albeit with poor statistics, were carried out at the Berkeley HILAC almost 20 years ago with emulsion detectors (Pf 63).

A prototype streamer chamber was designed and fabricated for use in tests with β^- particles and beam-gas interactions. This single gap chamber is shown in Figure 35; axial entry and exit ports of thin mylar permitted a scintillator-phototube detector to trigger on β^-, and an additional forward angle port allowed selection of elastic scattering and fragmentation events in tests with 140 MeV α particles. On completion of these tests in 1978, a more versatile chamber was designed specifically for heavy ion studies at the 88" cyclotron.

3.1.1. Physical Description

The present chamber is a single gap design of active volume $(17.1 \times 11.3 \times 5.1 \text{ cm}^3)$. Lucite construction and standard O-ring seals allow the sytem to be operated between 0 and 1 atmosphere pressure. The top electrode is electro-formed nickel mesh of 97% optical transmissivity; both the anode and cathode are isolated from the gas by lucite to prevent the formation of a spark channel. Thin (0.0025 cm) mylar windows occupy nearly the full area of the chamber's four sides as is seen in Figure 36, in order that trigger detectors may be positioned at any angle. More recently, the lateral right window has been replaced with a lucite plate and target ladder, and solid-state telescopes have been used as trigger devices exclusively, outside of the downstream window. A plan view of the experimental arrangement for these latter experiments is shown in Figure 37(a).

The chamber lies horizontally on the lower pole tip of the JUPITER C-magnet, the gap of which has been widened to 17.8 cm. The maximum field after modification is 1.1 T. A view of the chamber parallel to the E and B field is provided by two diagonal mirrors, as is evident in Figure 37(b). Upstream of the chamber a sliding seal radial offset and bellows connection has been installed to accommodate the passage of the beam, which is normally steered several centimeters to beam right to compensate for the beam trajectory within the magnet. The last section of beam line is lucite as conductors are forbidden within the proximity of the chamber, and the beam must traverse an air gap of 5 cm before entering the chamber. Downstream of the chamber, the beam is counted in a standard scintillator-phototube detector.

The pulsed high voltage is provided by a three stage Marx generator (Figure 38) insulated with pressurized dry air. All three stages have triggered spark gaps. The instrinsically good rise time of the high voltage pulse (≃12 ns) is matched on the falling edge by pulse shaping with a pressurized coaxial spark gap immediately before the chamber, and the waveform is monitored at this point with a calibrated high voltage probe.

The Flight Research camera outfitted with a 90 mm macro lens accommodates 500' rolls of 35 mm film (KO 2498,ASA 300), and the 4000 frames per roll are spray developed. The target cave must be totally darkened and the experimental area completely shrouded as there is no shutter for the camera and thus the film must remain exposed on the platens before each event. A perspective view of the configuration is shown in Figure 39 with shroud and camera magnetic shielding removed. This configuration is relevant for the initial beam-gas studies; in the present hybrid configuration the lateral scintillators (c) and (j) would be absent, and the target ladder, digital display, and telescope housing would be visible.

3.1.2. Operation

The first application of the chamber was a survey of interactions of heavy ions with a gas target, to gain experience with the operating characteristics of the chamber, and to examine particular predictions concerning the multiplicity of low-energy heavy fragment recoils to wide angles. Events induced by 26 MeV/nucleon ^{7}Li and ^{16}O and 35 MeV/nucleon ^{12}C with neon comprised the approximately 10% valid beam-gas events in 50,000 photographs. Figure 40 shows an interaction of ^{12}C + Ne of multiplicity nine; note the total charge of the projectile-target system is only 16. Single and coincident threshold scintillator detectors were used for the event trigger. However, even with the largest solid angles realizable, the variability of the vertex position along the beam path introduced significant trigger biases into the data. The operation with gas targets has been summarized in previous reports (Va 79b, Va 80) and will not be dealt with in greater extent here.

The chamber is found to work satisfactorily with standard mixtures of neon-helium (90%-10%). No special precautions are needed in terms of gas purity and its performance is uncritical over a range of gas pressures. Even without the admixture of electronegative poisoning, the memory time of the gas is sufficiently short to allow beam fluences of 5×10^4 s^{-1}. It is conjectured that the chamber may already be partially poisoned by the outgassing of the chamber construction because of its large surface-to-volume ratio.

The stability of the pulsed high voltage waveform was sufficiently good to require only periodic monitoring. The reproducibility of the pulse can be judged from Figure 41, which is a record of approximately 250 consecutive firings of the Marx generator. Normally, the peak field is 10-12 kV/cm, with a basewidth of 40 ns; under these conditions the streamers are observed to grow in length to a major fraction of the chamber gap. Properly speaking, the chamber should be termed a "track projection chamber" rather than a streamer chamber, as the streamers then do not inherently contain depth information. (This does not imply that such chambers cannot provide three-dimensional track reconstruction, as the dip angle can be inferred from track endpoint information on the chamber walls.)

The high voltage system is susceptible to sporadic failures, namely, misfiring and spontaneous firing. Normally, this is remedied with adjustment of the insulating gas pressure and input voltage; nevertheless, it is occasionally necessary to clean the spark gaps and replace component parts of the Marx generator.

3.1.3. Triggering

Clearly, the capability of a visual detector where the tracks themselves offer only limited information concerning the particle species can be greatly enhanced in a hybrid configuration where the identity of at least one of the particles can be determined. For the remainder of this section, this mode of operation and the first experiment performed with this system are described.

At present, the chamber has a downstream array of silicon ΔE-E telescopes, the thicknesses of the front and back detectors being optimized for the detection of beam velocity fragments ranging from lithium to oxygen. Timing and linear signals are derived in the usual way with conventional preamplifiers and electronics. To date, two options have been exercised for correlating the visual and electronic data.

In the first [Figure 42(a)], the two linear signals are given directly to an on-line particle identifier circuit and its output routed to an array of single channel analyzers in parallel, each defining a window in amplitude corresponding to a particular isotope or element. The outputs of all single channel analyzers are then fanned into an encoder that produces a digital display image on the photographic frame directly along with the event. Thus, the particle identification is incorporated immediately on the film plane, at the expense of loss of energy information from the telescope.

In the second scheme [Figure 42(b)], the linear signals are given to an analog-to-digital converter and recorded in event mode by computer. The correlation between each picture and the corresponding event on tape is preserved by an event number, which accompanies the event to computer and which simultaneously indexes the photographic frame. In either case, a fast timing signal initiates the high voltage pulse.

Although the performance of solid state detectors is unaffected by the strong magnetic field, it is impossible to shield them adequately from a large noise pickup from the streamer chamber because of the pulsed high voltage. However, the linear signals from the event are presented to the electronics after one transit time from target cave to control room, τ, whereas the noise pulse arrives at 3τ, and thus the problem is easily overcome with a moderately short shaping time (0.4 μs) and appropriate linear gate. Figure 43 summarizes the timing sequence of a single event. Once a valid coincidence is registered and event cycle initiated, a veto of approximately 750 ms is applied to block new signals appearing to the electronics until the camera has advanced the film to the next frame.

3.1.4. Physics: Transition from Transfer to Fragmentation Processes

The first experiments with the hybrid chamber were directed towards the determination of associated charged particle multiplicities. In addition to the simplicity of analysis, which then required only scanning rather than track measurement, the small linear dimensions of the chamber relative to typical radii of curvatures and noticeable track distortions caused by electrostatic effects precluded rigidity information from being extracted. Nevertheless, no other technique yet exists for multiplicity measurements in this energy regime.

One of the features first reported concerning the reactions of ^{16}O with various targets at 20 MeV/nucleon was that the longitudinal momentum spectra of complex fragments emitted in these collisions were in approximate agreement with measurements two orders of magnitude higher in energy (Ge 77, Gr 75). Subsequent experiments on this system and others at several intermediate energies qualitatively upheld this observation and pointed to the conclusion that a transition from low energy to high energy behavior, at least in phenomenology, may not be at all gradual but rather may occur at a reasonably well-defined threshold dependent on the system. A word of caution is due, for the state of agreement among various singles experiments is not entirely satisfactory, and reliable systematics for a broad range of projectile-target combinations are yet wanting.

Peripheral interactions at low energies (excluding elastic and inelastic scattering) have been successfully understood in terms of transfer reactions leading to two-body final states, using the term in its broadest sense encompassing single nucleon transfer and multistep multinucleon transfer processes. At relativistic energies, it is generally accepted that projectile fragmentation, characterized by a prompt breakup of the projectile in the proximity of the target and leading to at least a three-body final state, dominates the total reaction cross section. McVoy and Nemes, therefore, attempted to understand the rapid broadening of the longitudinal momentum spectra at bombarding energies in the vicinity of 20 MeV/nucleon in a direct reaction framework with a local momentum plane wave Born approximation calculation where both extremes could be treated on an equal footing (Mc 80). They found that for projectile fragmentation the momentum spectra are governed by the matrix elements

$$T^{PF}(\underset{\sim}{k}'_N) = \phi_{xN}(\underset{\sim}{k}_N - \underset{\sim}{k}'_N) \quad , \qquad (8)$$

where ϕ_{xN} is the momentum wave function of the fragment in the projectile, $\underset{\sim}{k}_N$ is the momentum of the fragment before removal from the projectile, and $\underset{\sim}{k}_N$ is the fragment momentum in the continuum. Their results then directly reduce to the projectile fragmentation calculations of Goldhaber in a Fermi gas model (Go 74).

The matrix element for transfer, on the other hand, is additionally constrained in momentum by the condition that the nucleons removed from the projectile are localized at the target in a quasibound state,

$$T^{Tr}(\underset{\sim}{k}'_N) = \phi_{xN}(\underset{\sim}{k}_N - \underset{\sim}{k}'_N)\phi_{xT}(\underset{\sim}{k}_o - \underset{\sim}{k}'_N) \quad . \tag{9}$$

The second term in the product is the momentum wave function of the removed nucleons in the target final state, and k_0 is the projectile momentum. It is responsible for additionally narrowing the momentum spectra at lower energies and does <u>not</u> appear in the matrix element for inclusive projectile fragmentation, due to the integration over momentum of all final states of the unobserved part of the projectile. What is most appealing about the calculation is that the transition from transfer to fragmentation arises in a natural way. Specifically, this transition occurs when the potential responsible for binding the removed nucleons to the target, $V_{xT}(\underset{\sim}{k}_x)$, loses its minimum because of the increasing centrifugal contribution as a function of bombarding energy. For the production of ^{15}N, the model gives fair quantitative agreement both for the energy where the transfer (^{16}O, ^{15}N) disappears in favor of the fragmentation $^{16}O \rightarrow {}^{15}N + p$ and their spectral widths, though it does less well in the case of ^{12}C.

A generalization of the concept of critical angular momentum has been proposed by Siwek-Wilczyńska for final states populated in cluster-transfer reactions (Si 79) and a semiclassical prescription has been derived for the maximum angular momentum l_{crit} that can be transferred in a peripheral collision as a function of target mass, transferred mass, and bombarding energy (Wi 73). For the case of ^{16}O + CsI at an energy of 16.5

MeV/nucleon, the predicted l_{crit} are displayed in Figure 44, along with the optimum angular momenta for transfer l_{opt}, of Brink (Br 72) based on wave mechanical matching considerations. The two calculations address the probability of transfer from two independent physical conditions. The former depends on the details of the nuclear, Coulomb, and centrifugal potentials and the latter essentially on kinematics. One may hypothesize, then, that a reaction leading to a particular final mass will occur by transfer if $l_{opt} < l_{crit}$ and by fragmentation if $l_{opt} > l_{crit}$.

These expectations have been examined for the system ^{16}O + CsI in the streamer chamber, with a target of 50 mg/cm^2 and an energy range in the target of 17.8-14.9 MeV/nucleon. A total of 16,000 pictures were taken at three trigger detector angles with the CsI target and mylar ($C_{10}H_8O_4$) and, of the 7000 pictures taken with CsI, approximately 55% represent valid events. The analog particle identification [scheme of Figure 42(a)] is seen in Figure 45, along with the gating definition for this experiment.

Two typical events with the mylar target are shown in Figure 46; the arrows indicate the trigger particle and identity in each case. The data were scanned for total multiplicity, the number of tracks within 45° of the beam in projected angle, and the number of tracks emitted in the backward direction. Although such a heavy target should overwhelmingly deexcite by neutron emission, occasional events were observed with tracks in the backward hemisphere, and these were assumed to be statistically evaporated charged particles. Although they represented a very small fraction of the total events, a correction was applied to the multiplicity distributions, assuming that such particles were isotropically evaporated and would be mistaken for projectile associated fragments a certain fraction of the time. The multiplicities so corrected are shown in Figure 47. The mean multiplicities as a function of fragment mass (Figure 48) show a pronounced dependence on scattering angle, perhaps not surprisingly as the selected trigger positions comfortably bracket the grazing angle for this energy.

Using the capability of the streamer chamber as an ideal 4π veto detector, the fraction of transfer events to total events is derived, assuming all single track events (M = 1) represent complete transfer of the projectile remnant to the target. The measured transfer probability is displayed in Figure 49, along with the calculation described above. The sharp cutoff that would normally result at the divergence of the optimum and critical angular momenta has been smoothed by introducing a Gaussian distribution in l around the Brink predictions to match the data best. The trend is qualitatively reproduced, although there is an excess of transfer events especially for the lighter ejectiles. To some degree the discrepancy should be due to events in which a fast neutron is emitted (and to which the experiment is not sensitive) resulting in a reduction of the transferred angular momentum. However, recent experiments on a similar system indicated that the preequilibrium neutrons are few in comparison with those evaporated from the target or projectile (Ga 80). A more important question to address is how a description so nearly devoid of physical input, especially in nuclear excitation degrees of freedom, has had such substantial success in reproducing the energy dependence of the incomplete fusion process (Si 79).

3.1.5. Prospectus: Investigation of Streamer Formation with Other Gases

Within the next few years, several major facilities will actively pursue programs of investigation between 20 and 100 MeV/nucleon, and undoubtedly among these interests will be very subthreshold (and thus very collective) pion production and searches for hydrodynamical effects in collisions of massive nuclei. There is hardly a need to comment that this trend puts an increasing premium on a versatile and reliable 4π detector of wide dynamic range in energy and sensitive to both light and heavy fragments. The hybrid streamer chamber would seem a viable candidate, though significant development work needs still to be done.

What has been clearly established so far is that the technique is feasible for energies as low as 10 MeV/nucleon and perhaps less. With care in design, such chambers could be constructed and operated with considerably less energy loss in the gas and chamber windows and with a concomitant improvement in the target-to-gas event ratio. Of greater consequence is the surprising ease with which conventional solid state detectors and electronics have worked along with this detector and to augment the advantages of both.

Chambers designed specifically for this energy range ideally would be a factor of four to five larger in linear dimensions than the present design, as it is essential to be able to extract accurate magnetic rigidity for all secondaries. To facilitate track reconstruction and streamline data analysis vastly, film as an intermediary should be eliminated as soon as possible in favor of charge coupled devices.

Equally important will be the development of particle identification capability intrinsic to track parameters alone. This calls for a major effort in the study of chamber response to a variety of charged particles and energies in the avalanche regime, streamer formation being completely ruled out if one seeks charge and mass information for high Z. Successful operation of optical avalanche chambers will require much greater concern for gas purity, reproducibility of the electric field profile, and implementation of image intensifiers.

There are circumstances under which the energy loss of secondary fragments in the target is simply unacceptable and a gas target is desired. Nature has favorably provided us with neon as a gas that works uncritically in streamer chambers. Are there others?

Hydrogen and helium have been made to perform passably but at much higher electric field strengths. A survey of the heavier noble gases argon and xenon has been carried out as a function of E and p with the chamber for both minimum ionizing β^- and heavy ions.

In tests with β^-, streamer formation is observed to occur for both Ar and Xe but at significantly higher values of E/p than necessary for Ne-He mixtures. Tracks with pure Ar were diffuse and ill-defined [Figure 50(b)] and disappeared rapidly with increasing pressure. Small admixtures of methane above the 0.1% level, however, radically changed the performance of the chamber. Tracks were now defined by bright, narrow and well-localized streamers, having a density of $\approx 1.5\ \mathrm{cm}^{-1}$ [Figure 50(c), 7% methane], about a factor of two less than that observed in Ne-He. Figures 50(d) and 50(e) (3.5% and 1.75% methane) show streamers simultaneously photographed parallel and perpendicular to the electric field; the filamentary appearance of the streamers viewed from the side is qualitatively similar to that with neon. The regularity of the streamer spacing and pronounced spreading of the discharge transverse to the particle trajectory (and hence to the direction of neighboring streamers) suggest a space charge effect. The onset of streamers in pure xenon occurs at still higher values of E and lower p and with a correspondingly lower linear density. Perpendicular to the applied field [Figure 50(f)], streamers in pure xenon are defined by bright spherical discharges with filaments emanating from it in both directions along the field.

In-beam studies with argon-methane mixtures at various fields and pressures yielded pictures of relatively poor quality. The two-body fragmentation of ^{12}C at 420 MeV shown in Figure 51 is representative of the behavior with heavy ions, whereas more lightly ionizing secondaries were frequently difficult to recognize because of the scarcity of streamers along the tracks. Similar tests with pure xenon at such low fields were negative.

We would like to acknowledge Dr. S.Y. Fung of the University of California, Riverside, for his assistance and material concerning the two-pion correlation experiment at the Bevalac streamer chamber. We also would like to acknowledge Dr. Ewa Skrzypczak of the Institute of Experimental Physics, Warsaw University, and Dr. Jerzy Bartke of the High Energy Laboratory, JINR Dubna, for their contribution of results from the SKM-200 Collaboration (Alma-Ata, Dubna, Bucuresti, Moscow, Tbilisi, Warsaw) carried out at the Dubna 2 m streamer chamber. We further acknowledge the members of the GSI-LBL-ANL-UNAM Streamer Chamber Collaboration, as well as the Harvey-Hendrie group at the 88" cyclotron in providing recent results for this report.

This work was supported by the Director, Office of Energy Research, Division of Nuclear Physics of the Office of High Energy and Nuclear Physics of the U.S. Department of Energy under Contract W-7405-ENG-48, and the Bundesministerium für Forschung und Technologie, West Germany.

LIST OF FIGURES

Figure 1. Schematic representation of a track in a streamer chamber, (a) viewed normal to the E field; (b) viewed parallel to the E field.

Figure 2. The streamer chamber as seen from one of the camera ports. The coils producing the magnetic field frame the chamber, which is seen through the transparent mylar window. The beam enters from the left and interacts on the target placed 30 cm downstream from the entrance window.

Figure 3. View of the 12 stage Marx generator. Across each capacitor bank 60 kV are applied charging the capacitors banks in parallel. When the chamber is triggered, the capacitors are discharged in series through the spark gaps, their voltages adding to a maximum of 720 kV.

Figure 4. Profile of the high voltage pulse applied to the chamber, with a width of 13 ns. The peak voltage is maintained constant to 2% to minimize fluctuations in brightness from one event to the next.

Figure 5. System used in the minimum bias and central trigger mode runs on the streamer chamber with relativistic heavy ions. The beam is prepared by the coincidence of three counters S1-S3 vetoed by a plastic scintillator collimator C, with a 1.2 cm diameter hole $B = S1 \cdot S2 \cdot S3 \cdot \overline{C}$. The counters S1 and S2 are 150 μm silicon surface barrier detectors, S3 is a thin plastic scintillator with a long light pipe to allow the phototube to be outside of the magnetic field of the chamber. A trigger scintillator T is placed downstream of the target, which intercepts the projectile fragments that did not suffer a collision. The trigger is

defined as the beam in anticoincidence with the trigger scintillator signal above a certain threshold ($B \cdot \overline{T}$).

Figure 6. Three typical events of ^{40}Ca + Ca at 2.1 GeV/nucleon, corresponding to different pulse heights (P) in the trigger scintillator relative to that of the beam (p_B): a) $p = p_B$, noninteracting beam; b) $p = 0.8\ p_B$, peripheral interaction in which the beam fragments with little momentum transfer to the target; c) $p = 0.1\ p_B$, central collision in which projectile and target completely fragment into nucleons and pions. Two kinds of tracks are clearly seen, the long thin ones in which individual streamers are observed, and the short ones of large diameter that, due to their large dip angle, connect the central electrode and the front electrode in such a way that the streamers fuse into each other and form a spark. The bright patches on the right side of the picture are flares.

Figure 7. Photograph of a flare with no magnetic field.

Figure 8. Table used for scanning the film. The three views of an event can be projected on the table with magnifications of x14 and x49. The scanner defines the event topology and counts and classifies the different types of tracks.

Figure 9. The trajectory of a charged particle in a homogeneous magnetic field is a helix with the pitch angle λ equal to the angle between the tangent to the trajectory and the plane normal to the magnetic field. When viewed with different cameras, the track gives different projections on a reference plane defined by fiducial marks of known coordinates, which are flashed simultaneously with the event.

Figure 10. Image plane digitizer used to measure the tracks to be reconstructed. The operator measures the fiducial marks first to obtain an absolute reference frame and then measures between seven and twenty points along the track in each view. The digitizer can be positioned to 1 μm on the 35 mm film.

Figure 11. Computer reconstruction of the measured trajectories in one view for a central interaction of ^{40}Ar + KCl at 1.8 GeV/nucleon. The beam enters from the left, and the position of the vertex is reconstructed from the intersection of all the tracks.

Figure 12. Laboratory momenta of the charged particles produced in the interaction of ^{40}Ar + KCl at 1.8 GeV/nucleon corresponding to Figure 11.

Figure 13. The same event as in Figure 12 transformed to the center of mass rapidity (x axis), transverse momentum (y,z) space.

Figure 14. Total charged particle (n_{tot}) and negative pion (n_{π^-}) multiplicity distributions for the interaction of Ar + KCl at 1.8 GeV/nucleon for the inelastic (●) and central (□) trigger modes. For the inelastic trigger, representative error bars are shown and the curve is drawn to guide the eye. At this energy the total cross section for π^- production is σ_T = 4.4 b.

Figure 15. Topology of reaction products for Ar + KCl in the inelastic trigger mode at 1.8 GeV/nucleon, drawn as contours of constant cross section (mb) in the n_{π^-} vs n_{tot} multiplicity plane. The dash-dot curve corresponds to n_{π^-} as a function of the total multiplicity. The straight lines correspond to the total disintegration limit.

Figure 16. a) Contour plot of the correlation between the π^- multiplicity (n_π-) and the number of participant protons (Q) from the interaction of 1.8 Gev/nucleon ^{40}Ar + KCl. The dots correspond to the mean π^- multiplicity as function of Q.
b) For a fixed number of participant protons, the π^- multiplicity distribution is essentially Poisson as is evident here by the mean and dispersion of each distribution as a function of Q.

Figure 17. Mean π- multiplicity as function of the number of participants (Q) for bombarding energies between 1 and 1.8 GeV/nucleon. A linear dependence is observed in all the cases.

Figure 18. Center of mass energy dependence of the mean negative pion multiplicity n_π- for central collisions of ^{40}Ar + KCl corresponding to a constant σ_c = 180 mb.

Figure 19. Kopylov ratio R^{S--}_{D--} versus relative pion momentum q. Beam of 1.8 GeV/nucleon ^{40}Ar incident on (a) BaI_2 and (b) Pb_3O_4 in an "inelastic" triggering mode and on (c) Pb_3O_4 triggering on the most central collisions. The curves are fit by Eq. (7) (Fu 78).

Figure 20. ^{40}Ar + KCl interaction with strange particle production at 1.8 GeV/nucleon. In the upper right quarter one sees the typical Vee-shaped decay of a Λ into a proton and a π^-. The proton is the stiffer track curving towards the right. Due to conservation of strangeness, the Λ is produced along with a kaon, either a K^+ or a K°, which is not identified. In this case, the Λ has a momentum of 3.45 GeV/c in the laboratory and decays 59.7 cm from the production vertex.

Figure 21. The observed Vees that are not gamma conversions into e^+e^- are shown here in a scatter plot of the pair's invariant mass under the assumptions they are a $p\pi^-$ or a $\pi^+\pi^-$ pair. One sees clearly two bands corresponding to a Λ ($M_{p\pi^-} = 1.15$ GeV) and a K° ($M_{\pi^+\pi^-} = 0.493$ GeV).

Figure 22. The Vees that satisfied the Λ decay kinematics are shown here in the center of mass on a scatter plot of parallel momentum vs transverse momentum. The shaded region corresponds roughly to the cutoff introduced by accepting only Λ's that decay further than 10 cm from the target. The circle around the $p_{||} = 0$ corresponds to the maximum kinematically allowed Λ momentum in the reaction $NN \rightarrow \Lambda NK$ at 1.8 GeV. Most of the Λ's have much larger c.m. momenta, partly due to the Fermi motion in the nuclei and in part to some collective effect.

Figure 23. Fragmentation of a 50 MeV/nucleon ^{40}Ar into p + Cl with the Cl ion stopping in the chamber gas. The magnetic field, normal to the photograph, is in this case 0.3 T.

Figure 24. Sketch of the streamer formations along the track for different particles. a) A 600 MeV/c π , minimum ionizing, has well-separated streamers and low overall brightness. b) A low energy proton, p = 600 MeV/c, shows streamers that begin to fuse with each other and a much higher brightness than a π of the same momentum. c) A relativistic heavy ion shows a very large ionization forming a bright, thick luminous tube, which, when viewed from the side, shows energetic δ rays escaping the streamer core and spiraling along the magnetic field.

Figure 25. Interaction of a 30 MeV/nucleon ^{40}Ar with BaI_2 producing a 14 charged particle final state. Three of the fragments stop in the downstream targets and trigger scintillator. Another particle stops in the gas producing a Bragg peak. A large variation in track width is seen. In this experiment the streamer chamber magnetic field was reduced to 0.3 T and image intensifiers were used to increase the dynamic range for particle identification.

Figure 26. Particle identification spectrum for the reaction products of ^{12}C induced reactions at 150 MeV/nucleon. The average peak streamer density is obtained by digitizing across the track with a 1 μm raster. Good separation of p, d, t, α is observed.

Figure 27. Imaging charged coupled device array (RCA-SID 52501) consisting of 525 x 320 sensitive squares 30 μm on a side. The incident light produces photoelectrons, which are collected in potential wells that can be shifted row by row and read out at 7 MHz. This signal can be digitized after amplification and stored in a computer memory creating a digitized image.

Figure 28. A directly digitized CCD frame of a 2.1 GeV/nucleon ^{40}Ca interaction on Pb is shown here converted back to a video signal and shown on a TV monitor. The tracks are deformed due to the different scales for the horizontal and vertical axis. One sees both minimum ionizing particles (spiraling track at the left side of the picture) and bridging tracks (short bright tracks near the vertex), which span a dynamic range of ∿1000 in light output. The bridging tracks and the flare at the top right are saturated, and one sees the "blooming" effect of the CCD at the flare.

Figure 29. The same event as Figure 28 shown as a three dimensional surface with the height proportional to the streamer brightness.

Figure 30. Streamer brightness profile across a row as seen by the CCD camera, showing the different track widths and brightnesses encountered.

Figure 31. The SKM-200 streamer chamber

Figure 32. Central collision of ^{16}O + Pb at an incident momentum of 4.5 GeV/c/nucleon.

Figure 33. The dependence of the average transverse momentum on the target mass number, A_T, for inelastic events and for subsamples of events characterized by different intervals of a) impact parameter, b) π^- multiplicity, c) π^- rapidity.

Figure 34. The dispersion, D_-, of the multiplicity distribution versus the average value of the multiplicity, $<n_->$ for negative π_o^-.

+	^{12}C - A	inelastic interactions
o	^{12}C - A	central interactions (with no charge fragments registered in a forward cone with a half angle θ_{ch} = 2°)
●	^{12}C - A	central interactions, θ_{ch} = 4°
■	^{16}O - A	central interactions, θ_{ch} = 2°
□	^{16}O - A	central interactions, θ_{ch} = 4°

Figure 35. Prototype streamer chamber used in early tests with β^- and beam-gas interactions with α particles.

Figure 36. The 88" cyclotron streamer chamber.

Figure 37. (a) Top view of the hybrid streamer chamber. (b) Upstream view; pulse shaping spark gap and high voltage probe not shown.

Figure 38. (a) Three-stage Marx generator. (b) Pulse shaping spark gap. The low inductance resistor dissipates the energy and prevents it from reflecting into the Marx generator.

Figure 39. Perspective view of the streamer chamber for initial beam-gas studies. (a) Streamer chamber and diagonal mirror. (b) JUPITER C-magnet. (c) scintillator-phototube trigger detector. (d) beam pipe. (e) pulse shaping coaxial spark gap. (f) Marx generator. (g) high voltage probe. (h) camera. (i) diagonal mirror. (j) scintillator-phototube trigger detector. In the present hybrid configuration, scintillators (c) and (j) would be absent; target ladder, digital display, and telescope housing would be visible.

Figure 40. Interaction of ^{12}C + Ne at 35 MeV/nucleon. Beam enters from the left.

Figure 41. High voltage pulse profile monitored at the chamber. Record consists of approximately 250 consecutive Marx firings.

Figure 42. Schematic of triggering schemes for hybrid operation. (a) Particle identification directly incorporated onto the film plane. (b) Event mode recording of telescope data along with event number. Fast and slow electronics denoted by "F" and "S", respectively.

Figure 43. Timing sequence for a single event cycle.

Figure 44. Calculated optimum (l_{opt}) and critical (l_{crit}) angular momenta as a function of ejectile mass for the system ^{16}O + CsI.

Figure 45. Particle identification spectrum and gating definition for ^{16}O + mylar experiment.

Figure 46. Typical events for ^{16}O induced reactions with mylar. Beam enters from the right; mid-target energy is approximately 16.5 MeV/nucleon. Arrow to the left of each photograph indicates the trigger particle and its identity according to the gate number.

Figure 47. Associated multiplicity distributions as a function of ejectile and angle for ^{16}O + CsI at 16.5 MeV/nucleon. Preliminary data.

Figure 48. Mean multiplicities as a function of ejectile and angle for ^{16}O + CsI at 16.5 MeV/nucleon. Preliminary data.

Figure 49. Transfer probability (fraction of M = 1 events to total events) as a function of ejectile and angle. Preliminary data. Also shown is the calculated transfer probability described in the text.

Figure 50. Tracks of ^{90}Sr β^- in the 88" cyclotron streamer chamber with various gases. (a) Ne-He, 700 torr, E = 11.2 kV/cm. (b) Ar, 310 torr, E = 13.4 kV/cm. (c) Ar + methane (7%), 310 torr, E = 13.4 kV/cm. (d) Ar + methane (3.5%), 310 torr, E = 11.4 kV/cm, parallel (top) and perpendicular (bottom) to E. (e) same as (d) except 1.75% methane. (f) Xe, 210 torr, E = 11.4 kV/cm, parallel (top) and perpendicular (bottom) to E. Length of the photographic image is 15 cm.

Figure 51. The fragmentation of ^{12}C at 420 MeV into two heavy ions, with Ar-methane volume gas.

List of Tables:

TABLE I

Magnet

Configuration	M5 picture frame, both poles removed
Dimensions	166 cm inner coil diameter, 69.3 cm coil gap
Field	1.32 T, 9% maximum variations within chamber
Power	2.6 megawatts

Chamber

Sensitive volumen	120 cm long x 60 cm high x (2 x 20 cm) deep
Center electrode Front electrode	Stainless steel 0.22 mm wire mesh 76% light transmission
Gas	90% Ne, 10% He, $\sim$30 ppm SF_6

Photography

Cameras	Flight Research
Modification	loop generators, cycled vacuum platens
Rewind Cycle	50-300 msec
Lenses	40 mm Leitz Sumicron
Demagnification	49x at center of the chamber
Stereo	3 views, 15° stereo angle
Film	Kodak SO-143

Marx Generator

Configuration	12 stages
Capacity	9 nf per stage
Supply Voltage	30 kV regulated
Output	720 kV
Charging Time	250 msec
Premarx	2 stages
Trigger amplifier	8 kV hydrogen thyratron

Blumlein Transmission Line

Configuration	oil insulated with trombone
Pulse Length	adjustable 7 to 15 ns
Spark Gap	distance adjustable 18-27 mm in SF_6 atmosphere 25-32 psi

TABLE II

Momentum resolution

P	$<\Delta p/p>$
$p < 20$ MeV/c	0.8%
200 MeV/c $< p <$ 100 MeV/c	1.5%
100 MeV/c $< p$	5%

Angle resolution	$\Delta\theta$
Dip angle λ	0.8°
Aximuth X	0.9°

Position Resolution in the Vertex Reconstruction

In the electrode plane	2.8 mm
In depth	6.4 mm

TABLE III

E_{lab}[GeV/n]	$<Q>$	D_Q	$<n_{\pi^-}>$	D_{π^-}
0.360	23.16 ± 0.12	4.17 ± 0.07	0.20 ± 0.01	0.42 ± 0.09
0.556	25.97 ± 0.19	3.8 ± 0.12	0.79 ± 0.03	0.87 ± 0.09
0.772	26.94 ± 0.20	4.2 ± 0.10	1.58 ± 0.05	1.28 ± 0.07
0.977	29.30 ± 0.23	3.3 ± 0.10	2.35 ± 0.07	1.43 ± 0.06
1.180	29.13 ± 0.22	3.4 ± 0.14	3.34 ± 0/08	1.81 ± 0.06
1.385	28.2 ± 0.23	3.9 ± 0.13	4.10 ± 0.09	1.85 ± 0.05
1.609	28.2 ± 0.20	3.4 ± 0.08	5.09 ± 0.08	2.17 ± 0.05
1.808	28.0 ± 0.10	4.4 ± 0.05	5.79 ± 0.04	2.45 ± 0.03

TABLE IV

N per Event	r_o(fm) Expt.	χ^2/DF	r_o(fm) TFM theory $\rho_c = \frac{1}{3}\rho_o$	r_o(fm) TFM theory $\rho_c = \rho_o$
2-4	3.12±1.10	8.56/7	5.65	4.21
5-8	4.00±0.72	15.15/7	7.72	5.36
9-12	4.82±0.65	7.23/7	8.36	5.81
13-15	5.57±1.17	3.59/7	8.42	5.85

TABLE V

Fragmentation process		Targets				
		σ				α
		Li	C	Al	Cu	($\sigma \sim A_T^{\alpha}$)
Inclusive emission of the projectile fragments	^1H	166±13	227±34	319±34	417±45	0.40 ± 0.05
	^2H	84±15	91±27	113±38	159±45	0.27 ± 0.14
	^3H	47±5	58±9	73±20	95±14	0.30 ± 0.08
	^3He	48±5	49±8	70±15	95±20	0.30 ± 0.10
peripheral		208±20	244±26	313±48	412±70	0.29 ± 0.08
central		51±5	106±10	248±28	525±50	1.01 ± 0.06

(Ak 80) V.D. Aksinenko, M.Kh. Anikina, V.S. Buttsev, L.V. Chkaidze, N.S. Glagoleva, A.I. Golokhvastov, A.G. Grachov, K.K. Gudima, E.A. Dementjev, S.V. Kadikova, N.I. Kaminski, S.A. Khorozov, E.S. Kuznetsova, J. Lukstins, A.T. Matyushin, V.T. Matyushin, M.G. Mescherjakov, Zh.Zh. Musulmanbekov, N.N. Nurgozhin, E.O. Okonov, T.G. Ostanevich, A. Peisert, E. Skrzypczak, R. Szwed, E.A. Shevchenko, S.S. Sidorin, E.K. Khusainov, V.D. Toneev, G.L. Vardenga, V.D. Volodin, J.A. Zakrzewski, and M.S. Zuravleva, Nucl. Phys. A348:518 (1980)

(Ba 67) R.K. Bardin, P.J. Gollon, J.D. Ullman, C.S. Wu, Phys. Lett. 26B:112 (1967)

(Ba 79) J. Bartke, Proc. of the 8th Int. Conf. on High Energy Physics and Nucl. Structure, Vancouver, August (1979), D.F. Meadsy and A.W. Thomas (eds.), North Holland

(Bj 69) J.D. Bjorken and E.A. Paschos, Phys. Rev. 185:1975 (1969)

(Br 72) D.M. Brink, Phys. Lett. 40B:37 (1972)

(Br 78) C. Bricman, C. Dionisi, R.J. Hemingway, M. Mazzucato, L. Montanet, N. Barash-Schmidt, R.C. Crawford, M. Roos, A. Barbaro-Galtieri, C.P. Horne, R.L. Kelly, M.J. Losty, A. Rittenberg, T.G. Trippe, G.P. Yost, B. Armstrong, Phys. Lett. 75B:1 (1978)

(Ch 63) G.E. Chikovani, V.N. Roinishvili, V.A. Mikhailov, Phys. Lett. 6:254 (1963)

(Ch 64) G.E. Chikovani, V.N. Roinishvili, V.A. Mikhailov, Nucl. Inst. and Meth. 29:261 (1964)

(Cu 73) E. Cummins, Weak Interactions (McGraw-Hill, New York, 1973)

(Cu 80) J. Cugnon, T. Mizutani, and J. Vandermeulen, CALTECH report MAP-10 (1980)(unpublished).

(Da 68) O.I. Dahl, T.B. Day, F.T. Solmitz and N.L. Gould, "SQUAW" Group A Programming Note No. P-127, Lawrence Berkeley Laboratory, unpublished

(Da 69) V.A. Davidenko, B.A. Dolgoshein, V.K. Semenov, S.V. Somov, Nucl. Inst. and Meth. 67:325 (1969)

(Do 64) B.A. Dolgoschein, B.U. Rodionov, B.I. Luchkov, Nucl. Inst. and Meth. 29:270 (1964)

(Eg 75) K. Eggert, W. Thome, B. Betev, G. Bohm, P. Darriulat, P. Dittman, E. Gygi, M. Holder, K.T. McDonald, H.G. Pugh, F. Schneider, H. Albrecht, T. Modis, K. Tittle, I. Derado, V. Eckardt, H.J. Gebauer, R. Meinke, O.R. Sander, P. Seyboth, Nucl. Inst. and Meth. 126:477 (1975)

(Fa 79) M.L. Faccini-Turluer, R. Barloutaud, C. Cochet, A. Givernaud, L. Mosca, J. Saudraix, P. Sixel, L. Becker, U. Gensch, E. de Wolf, F.A. Triantis, R. Windmolders, H. Blumenfeld, Yu.I. Arestov, P.V. Chliapnikov, A.A. Minaenko, A.M. Rybin, V.A. Urarov, J. MacNaughton, Zeit. Phys. C1:19 (1979)

(Fr 80) E.M. Friedlander, R.W. Gimpel, H.H. Heckman, Y.J. Karant, B. Judek, E. Ganssauge, Phys. Rev. Lett. 45:1084 (1980)

(Fr 82) E.M. Friedlander and H.H. Heckman, in Heavy Ion Science, Volume II (D.A. Bromley, ed.), Plenum Press, New York (1982)

(Fu 78) S.Y. Fung, W. Gorn, G.P. Kiernan. F.F. Liu, J.J. Lu, Y.T. Oh, J. Ozawa, R.T. Poe, L. Schroeder, and H. Steiner, Phys. Rev. Lett. 40:292 (1978)

(Fu 78a) S.Y. Fung, W. Gorn, G.P. Kiernan, J.J. Lu, Y.T. Oh, R.T. Poe, Phys. Rev. Lett. 41:1592 (1978).

(Ga 80) A. Gavron, R.L. Ferguson, Felix E. Obenshain, F. Plasil, G.R. Young, G.A. Petitt, K. Geoffroy Young, D.G. Sarantites, C.F. Maguire, Phys. Rev. Lett. 46:8 (1980)

(Ge 77) C.K. Gelbke, D.K. Scott, M. Bini, D.L. Hendrie, J.L. Laville, J. Mahoney, M.C. Mermaz, C. Olmer, *Phys. Lett.* 70B:415 (1977)

(Go 74) A.S. Goldhaber, *Phys. Lett.* 53B:306 (1974)

(Go 78) J. Gosset, J.I. Kapusta and G.D. Westfall, *Phys. Rev.* C18:844 (1978)

(Gr 72) A. Grigarian, A. Ladage, D.J. Mellema, F.D. Rudnick, D.H. Stork, H.K. Ticho, G.J. Eckman, D.B. Hunt, R. Peters, in Proceedings of the First International Conference on Streamer Chamber Technology, September 14-15, 1972, ANL-8055 (Instruments), J.M. Watson, ed.

(Gr 75) D.E. Greiner, P.J. Lindstrom, H.H. Heckman, B. Cork, F.S. Bieser, *Phys. Rev. Lett.* 35:152 (1975)

(Gr 79) J.G.H. de Groot, J. Engels, *Zeit. Phys.* *C*1:51 (1979)

(Gy 78) M. Gyulassy and K. Kauffmann,. *Phys. Rev. Lett.* 40:298 (1978)

(He 75) Clemens A. Heusch, Barry Lieberman, Abraham Seiden, *Nucl. Inst. and Meth.* 124:165 (1975)

(He 78) K. Heller, P.T. Cox, J. Dworkin, O.E. Overseth, P. Skubic, L. Schachinger, T. Devlin, B. Edelman, R.T. Edwards, G. Bunce, R. Handler, R. March, P. Martin, L. Pondrom, M. Sheaff, *Phys. Rev. Lett.* 41:607 (1978)

(Ho 77) M. Holder, J. Knobloch, J. May, H.P. Paar, P. Palazzi, D. Schlatter, J. Steinberger, H. Suter, H. Wahl, E.G.H. Williams, F. Eisele, C. Geweniger, K. Kleinknecht, G. Spahn, H.-J. Willutzki, W. Dorth, F. Dydak, V. Hepp, K. Tittle, J. Wotschack, P. Bloch, B. Deraux, M. Grimm, J. Maillard, B. Reyaud, J. Rander, A. Savoy-Navarro, R. Turlay, F.L. Navarria, *Phys. Lett.* 69B:377 (1977)

(Hü 77) J. Hüfner and J. Knoll, *Nucl. Phys.* A290:460 (1977)

(Ko 73) G.I. Kopylov, M.J. Podgoretsky, *Yad. Fiz.* 18:656 (1973); [*Sov. J. Nucl. Phys.* 18:336 (1974)].

(Ko 74) G.I. Kopylov, Phys. Lett. 50B:472 (1974).

(Lu 81) J.J. Lu, D. Beavis, S.Y. Fung, W. Gorn, A. Huie, G.P. Kiernan, R.T. Poe, G. VanDalen, Phys. Rev. Lett. 46:898 (1981).

(Mc 80) K.W. McVoy, M.C. Nemes, Z. Physik A295:177 (1980)

(Mo 79) I. Montvay and J. Zimanyi, Nucl. Phys. A316:490 (1979)

(Pf 63) E. Pfohl, Ch. Winter-Gegauff, J.P. Lonchamp, Proceedings of the Third Conference on Reactions Between Complex Nuclei, Asilomar, ed. A. Ghiorso, R.M. Diamond, H.E. Conzett, University of California Press (1963)

(Ri 74) Peter Rice-Evans, Spark, Streamer, Proportional and Drift Chambers, Richelieu Press, Ltd., London (1974)

(Sa 78) Jack Sandweiss, Physics Today 31:40 (1978)

(Sa 80) A. Sandoval, R. Stock, H.E. Stelzer, R.E. Renfordt, J.W. Harris, J.P. Brannigan, J.V. Geaga, L.J. Rosenberg, L.S. Schroder and K.L. Wolf, Phys. Rev. Lett. 45:874 (1980)

(Sa 80a) A. Sandoval, H.H. Gutbrod, W.G. Meyer, R. Stock, Ch. Lukner, A.M. Poskanzer, J. Gosset, J.-C. Jourdain, C.H. King, G. King, Nguyen Van Sen, G.D. Westfall, K.L. Wolf, Phys. Rev. C21:1321 (1980) and references therein

(Sc 79) L.S. Schroeder, Nucl. Inst. and Meth. 162:395 (1979)

(Si 79) K. Siwek-Wilczyńska, E.H. du Marchie van Voorthuysen, J. van Popta, R.H. Siemssen, J. Wilczyński, Phys. Rev. Lett. 42:1599 (1979)

(So 65) F.T. Solmitz, A.D. Johnson and T.B. Day, "Three View Geometry Program," Alvarez Group Programming Note-P-117, Lawrence Berkeley Laboratory, unpublished

(St 69) A.W. Stetz, V. Perez-Mendez, Nucl. Instr. and Meth. 73:34 (1969)

(St 79) H. Stöcker, J. Maruhn, and W. Greiner, Z. Physik A286:121 (1978) and Phys. Lett. 81B:303 (1979)

(Ul 68) J.D. Ullman, R.K. Bardin, P.J. Gollon, C.S. Wu, Nucl. Inst. and Meth. 66:1 (1968)

(Va 73) G.A. Vardenga, V.D. Volodin, N.S. Glagoleva, Yu.A. Karzhavin, P.S. Kuznetsov, Yu. Lukstinjsh, A.T. Matyushin, V.T. Matyushin, M.G. Mescheryakov, E.O. Okonov, S.N. Khorozov, in Proceedings of the 1973 International Confernce on Instrumentation for High Energy Physics, Frascati, 1973 (ed. S. Stipeich) 157 (1973)

(Va 78) J.P. Vary, Phys. Rev. Lett. 40:295 (1978)

(Va 79a) Ch. de la Vaissiere, H. Muirhead, S.N. Ganguli, Ph. Gavillet, M. Mazzucato, C. Dionisi, R. Blokzijl, J.C. Kluyver, G.F. Wolters, E.W. Kittel, M. Zralek, B. Foster, P. Grossman, Zeit. Phys. C1:3 (1979)

(Va 79b) K. Van Bibber, W. Pang, M. Avery, Proceedings of the Symposium on Heavy Ion Physics from 10 to 200 MeV/amu, Vol. 1, p. 365, Brookhaven National laboratory, July 16-20, 1979, J. Barrette, P.D. Bond, ed. (BNL-51115)

(Va 80) K. Van Bibber, W. Pang, M. Avery, E. Bloemhof, IEEE Transactions on Nuclear Science, Vol. NS-27, No. 1, 86 (1980)

(Wa 72) J.M. Watson, ed., Proceedings of the First International Conference on Streamer Chamber Technology, September 14-15, 1972, ANL-8055 (Instruments)

(Wi 73) J. Wilczyński, Nucl. Phys. A216:386 (1973)

(Ya 78) F.B. Yano, S.E. Koonin, Phys. Lett. 78B:556 (1978).

(Ya 79) Y. Yariv and Z. Frankel, Phys. Rev. C20:2227 (1979)

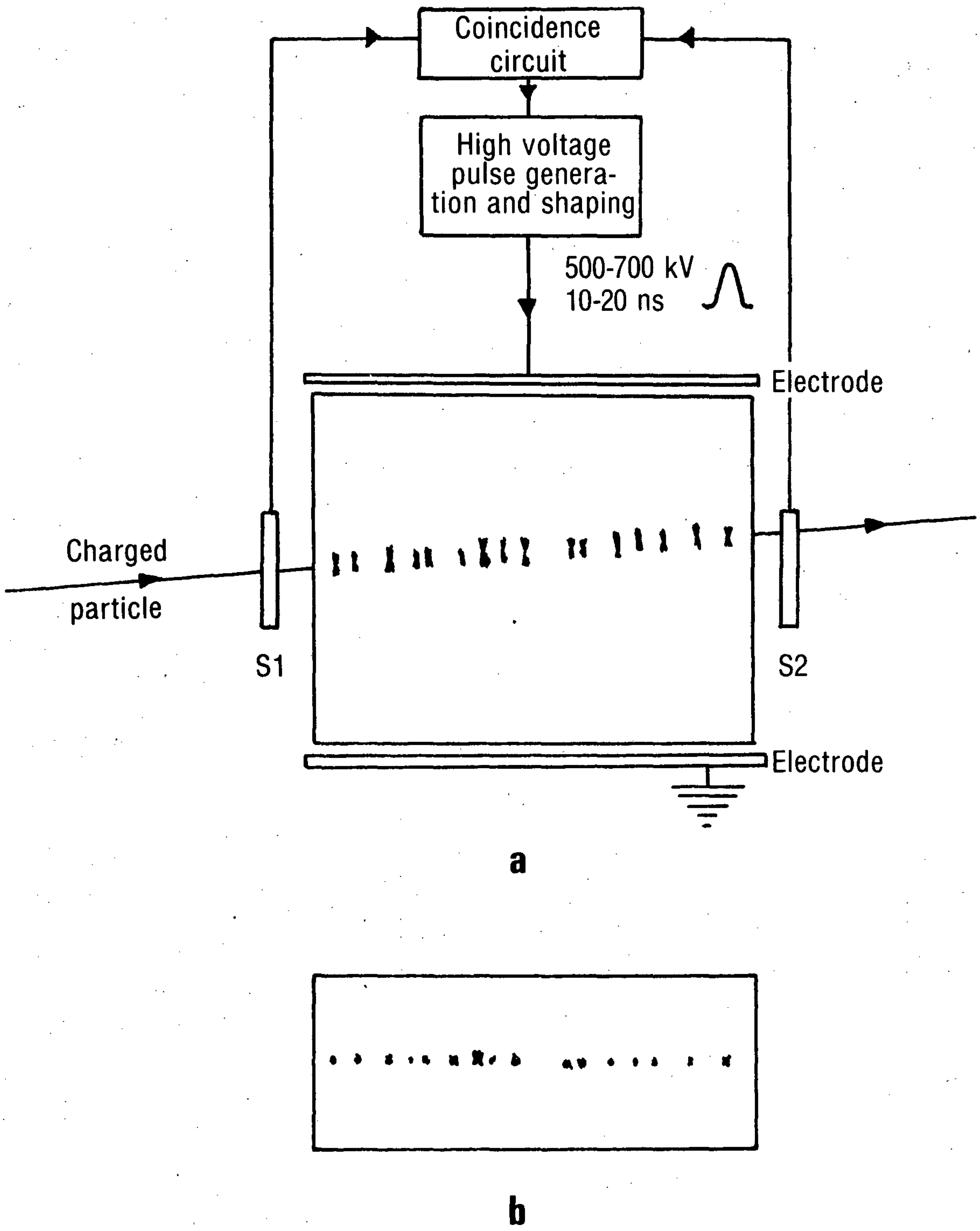

Fig. 1

XBL 783-7506 A

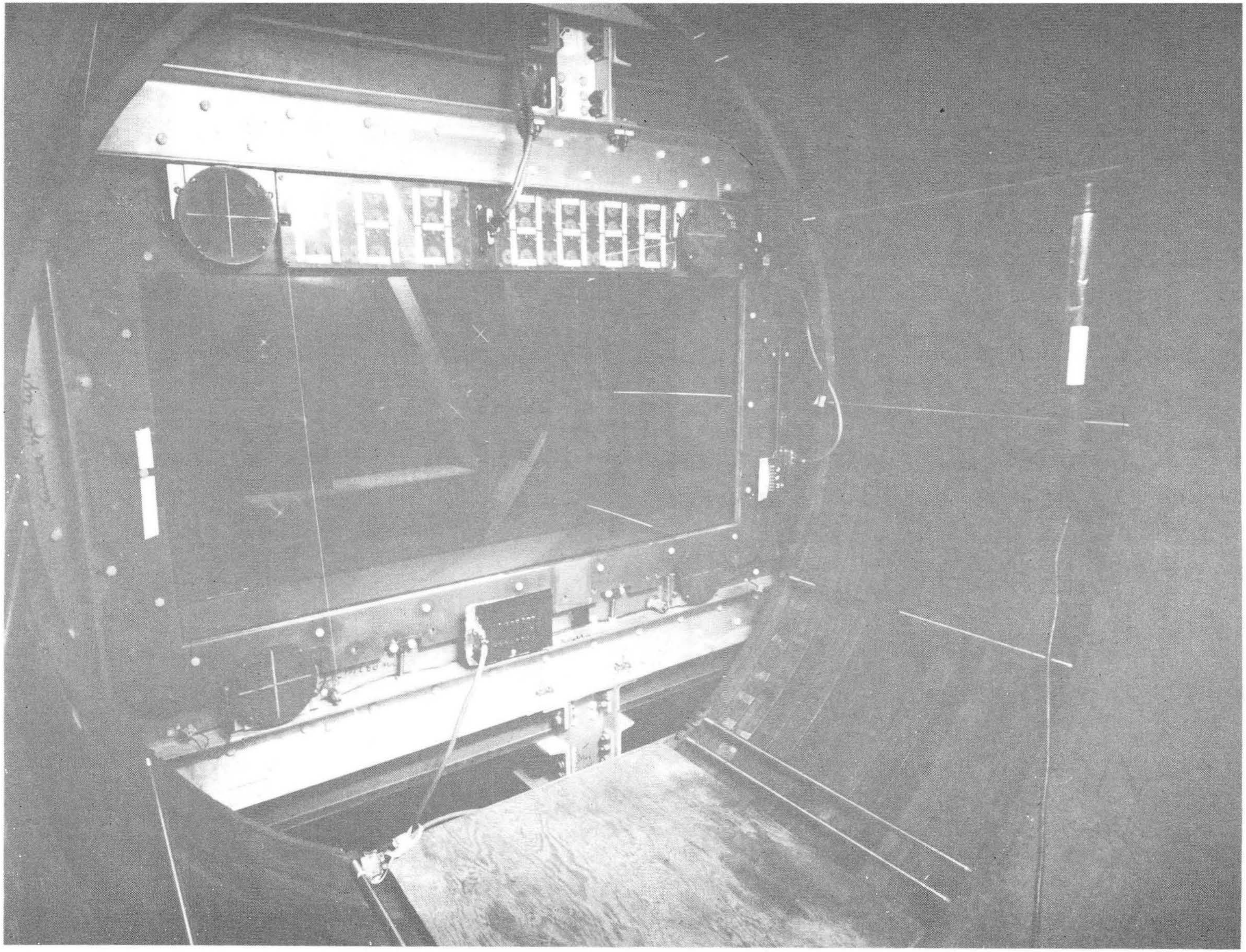

Fig. 2

CBB796-7630

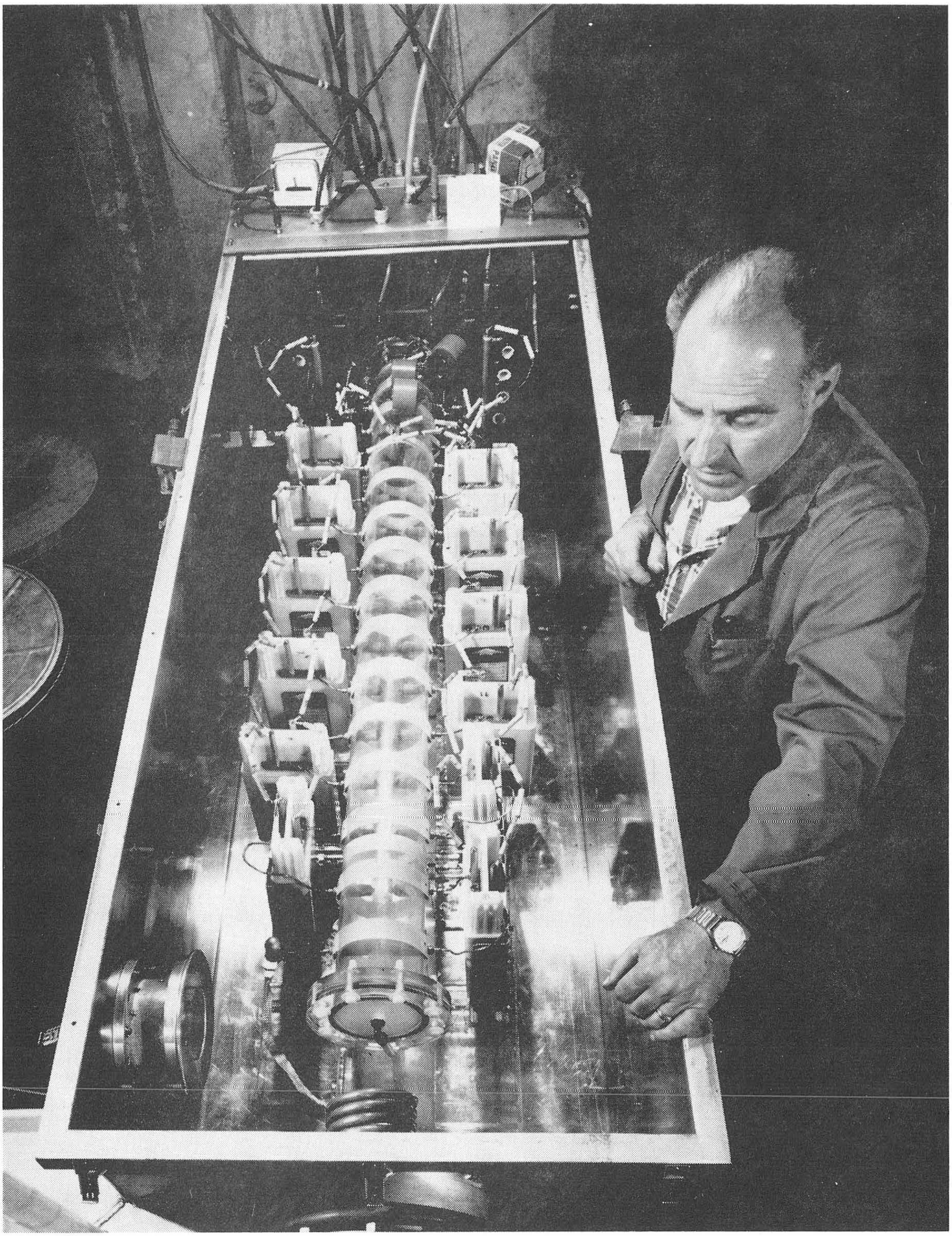

Fig. 3

CBB817-6558

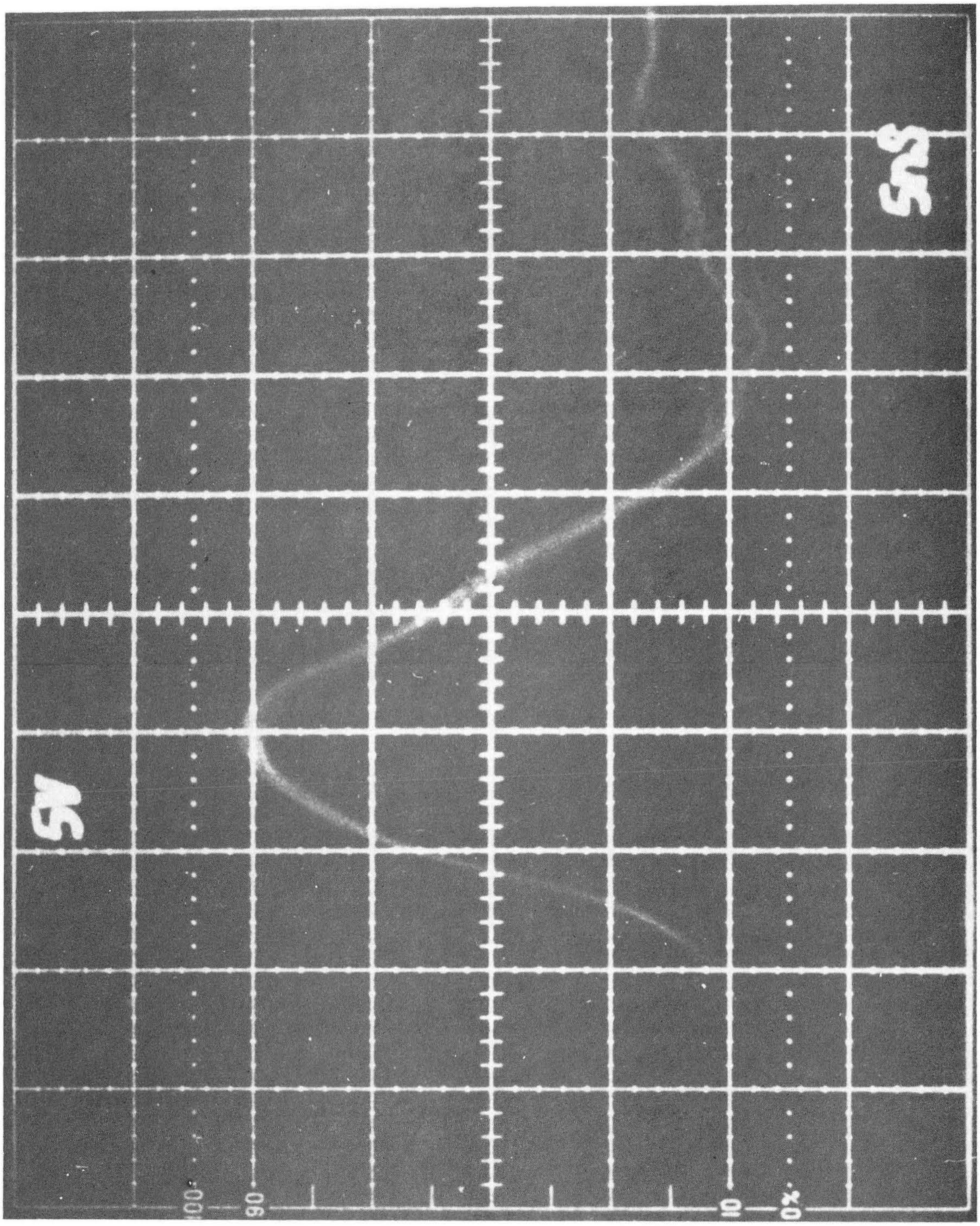

Fig. 4

XBB 816-5362

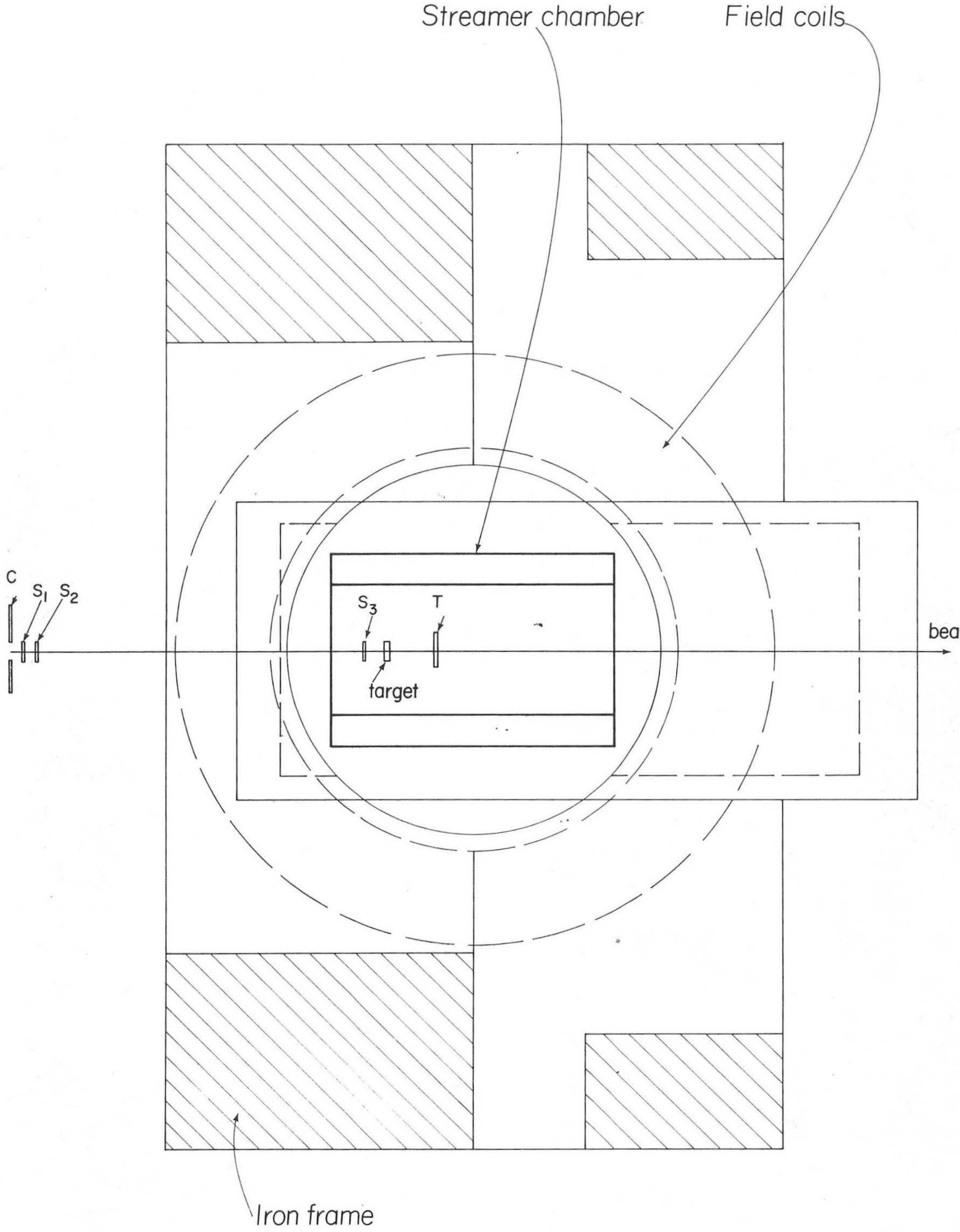

XBL 817-1054

Fig. 5

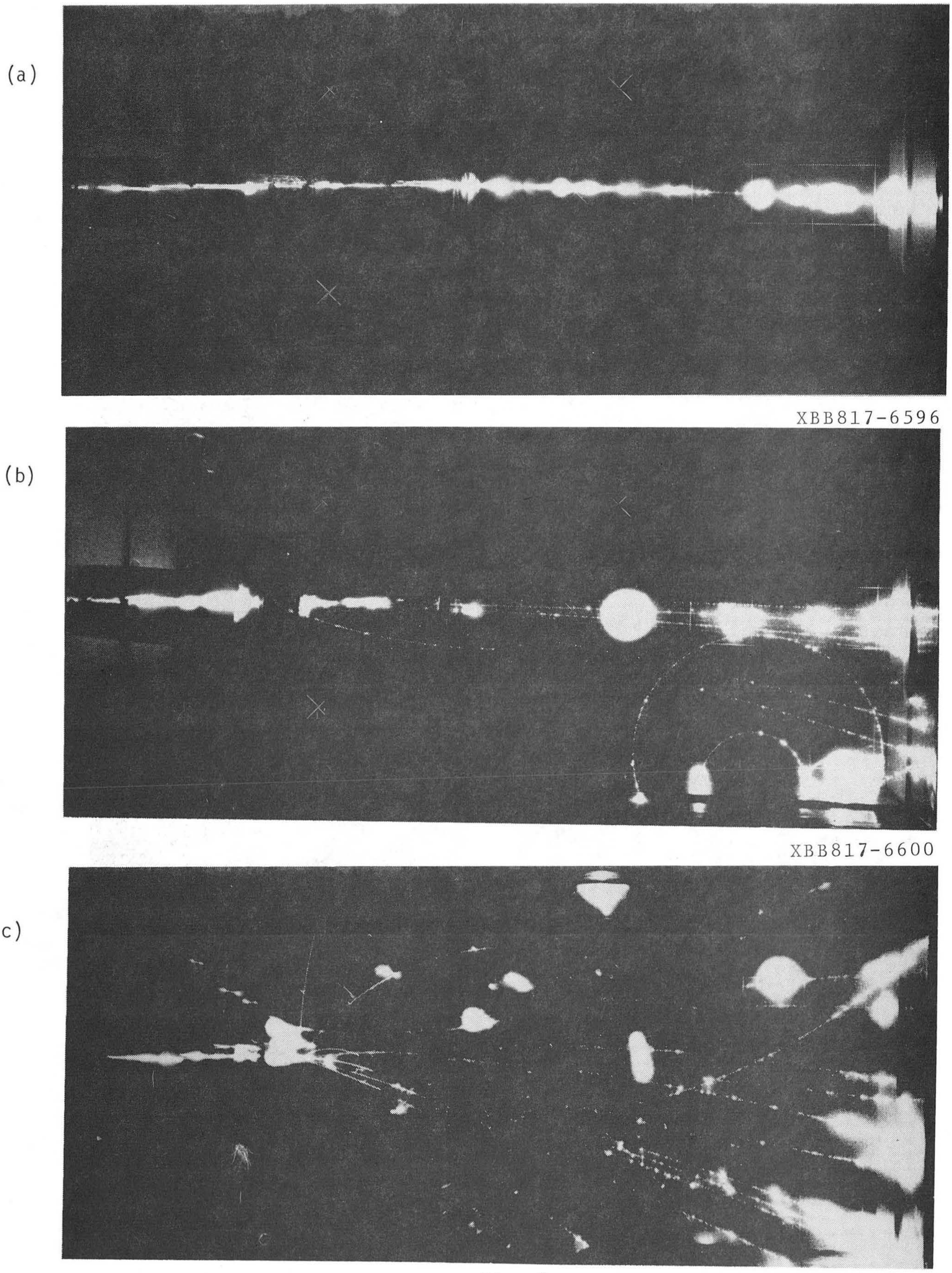

Fig. 6

XBB817-6593

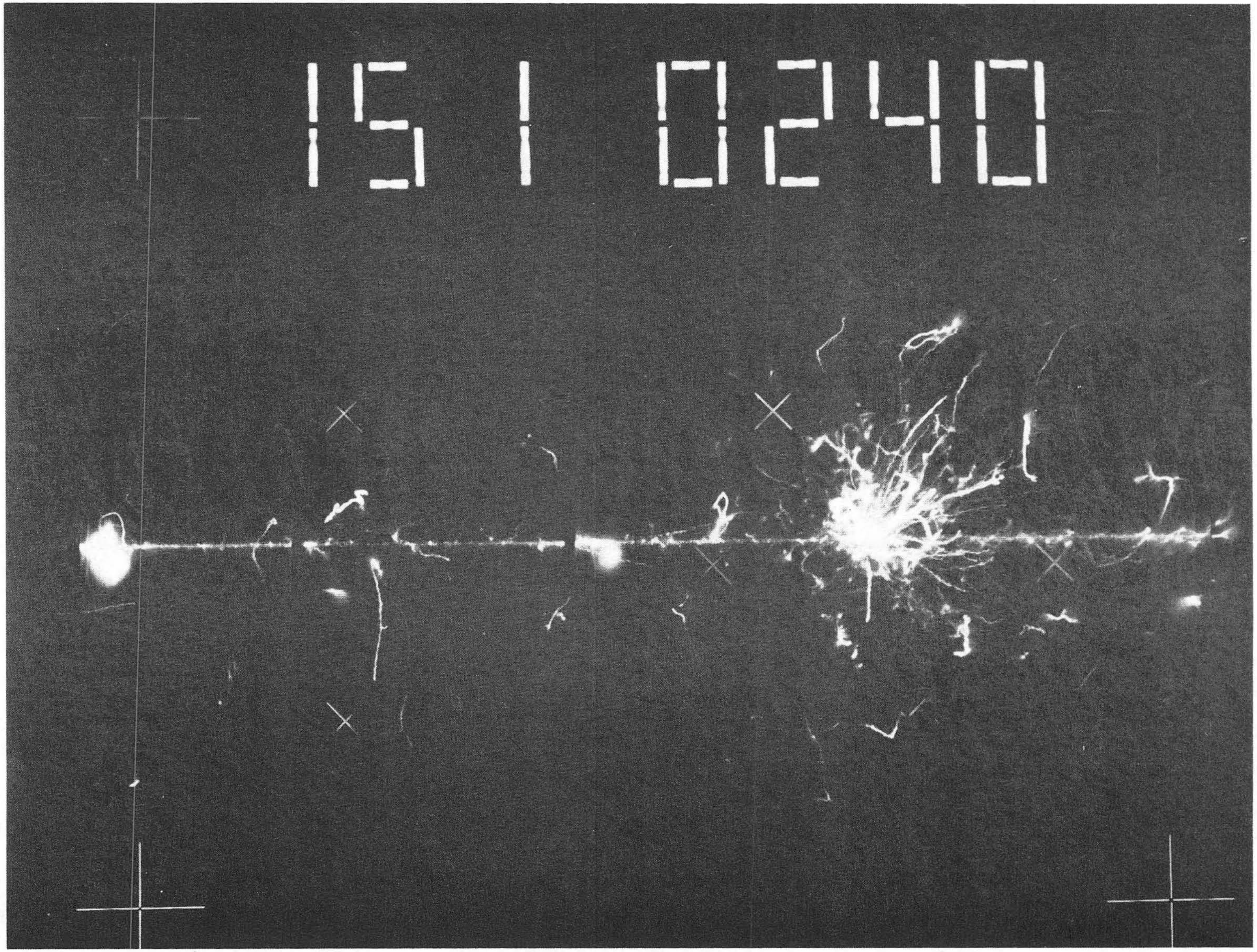

Fig. 7

XBB817-6602

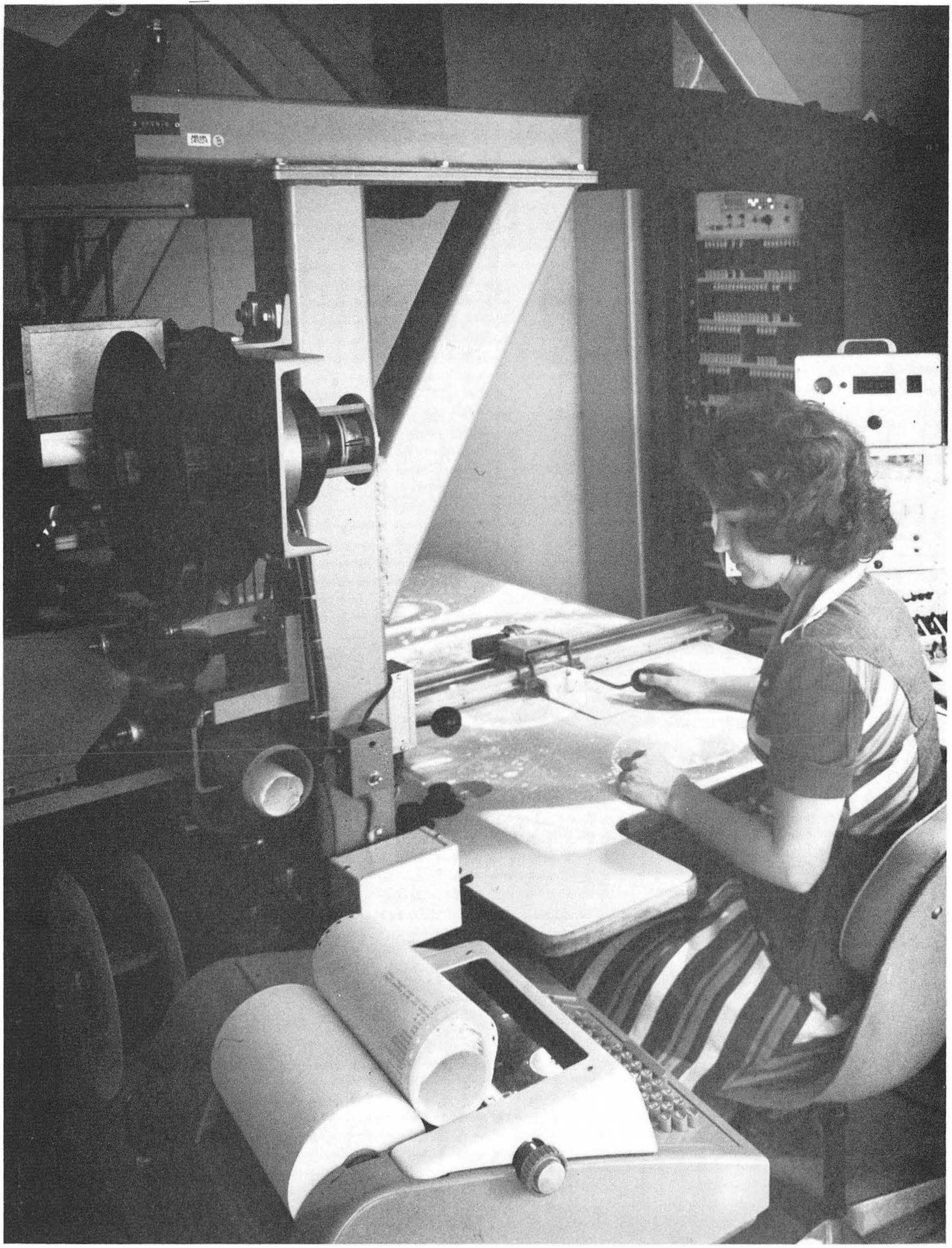

Fig. 8 CBB769-8903

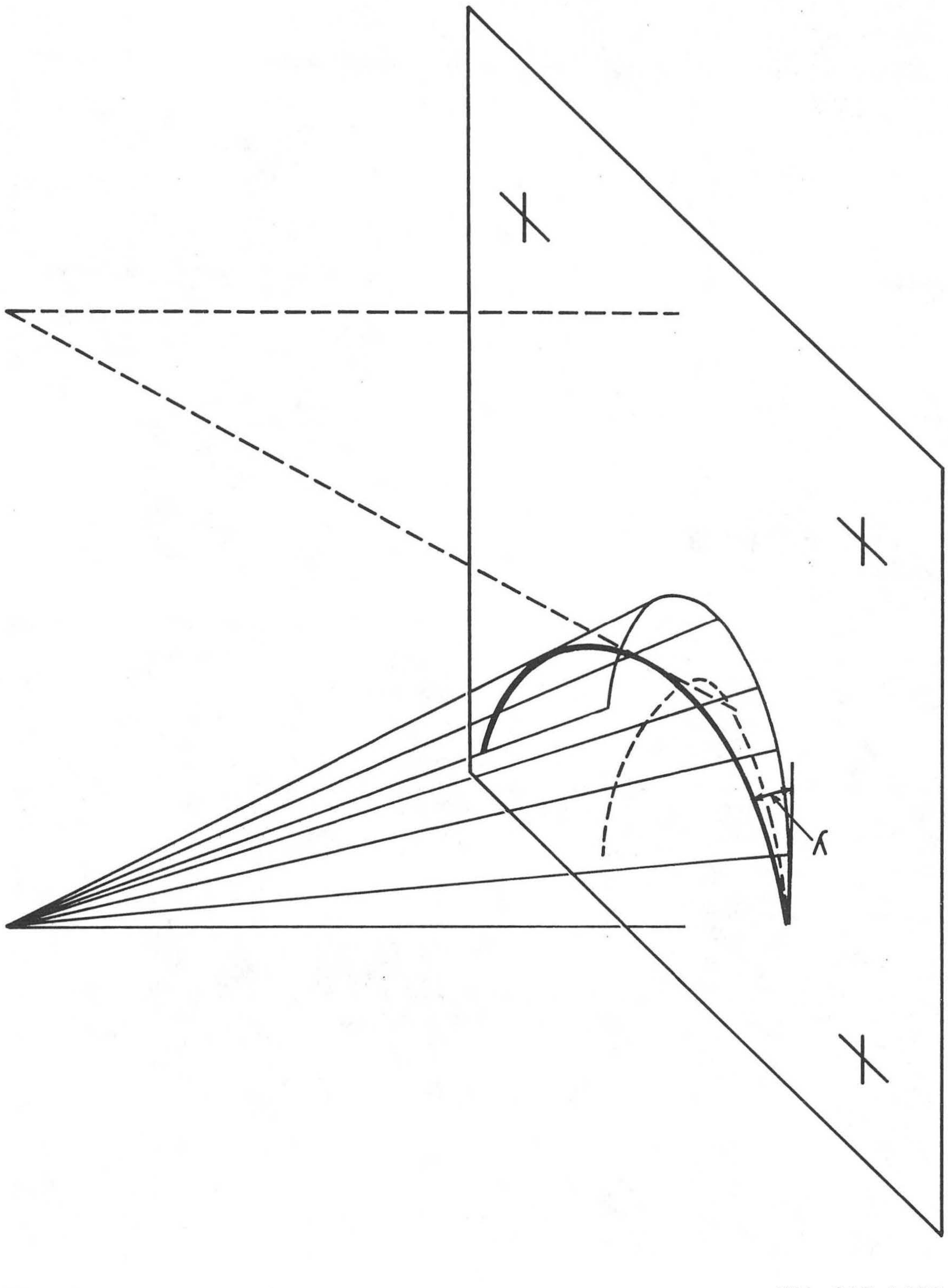

Fig. 9

XBL 817-1056

Fig. 10

CBB769-8901

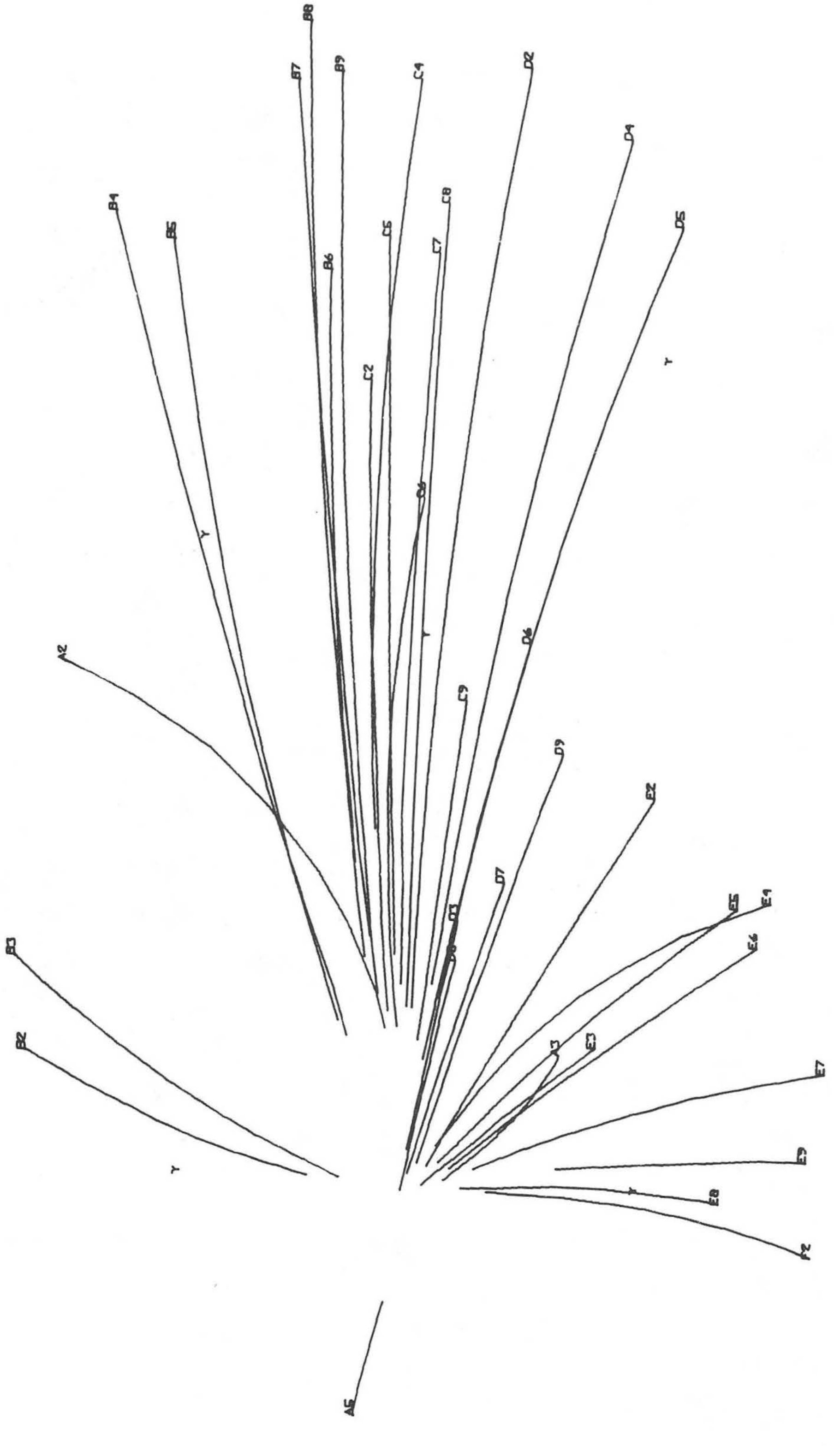

6052702.

Fig. 11

XBL 816-10164

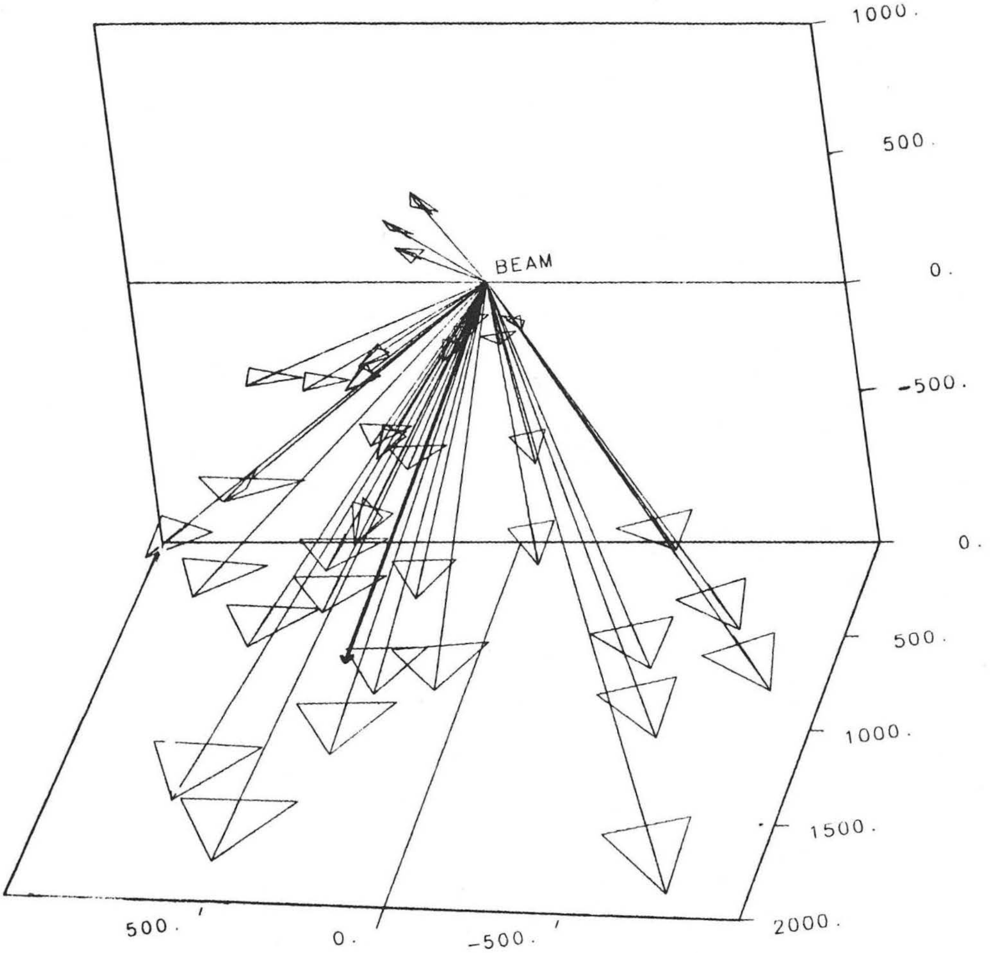

Fig. 12

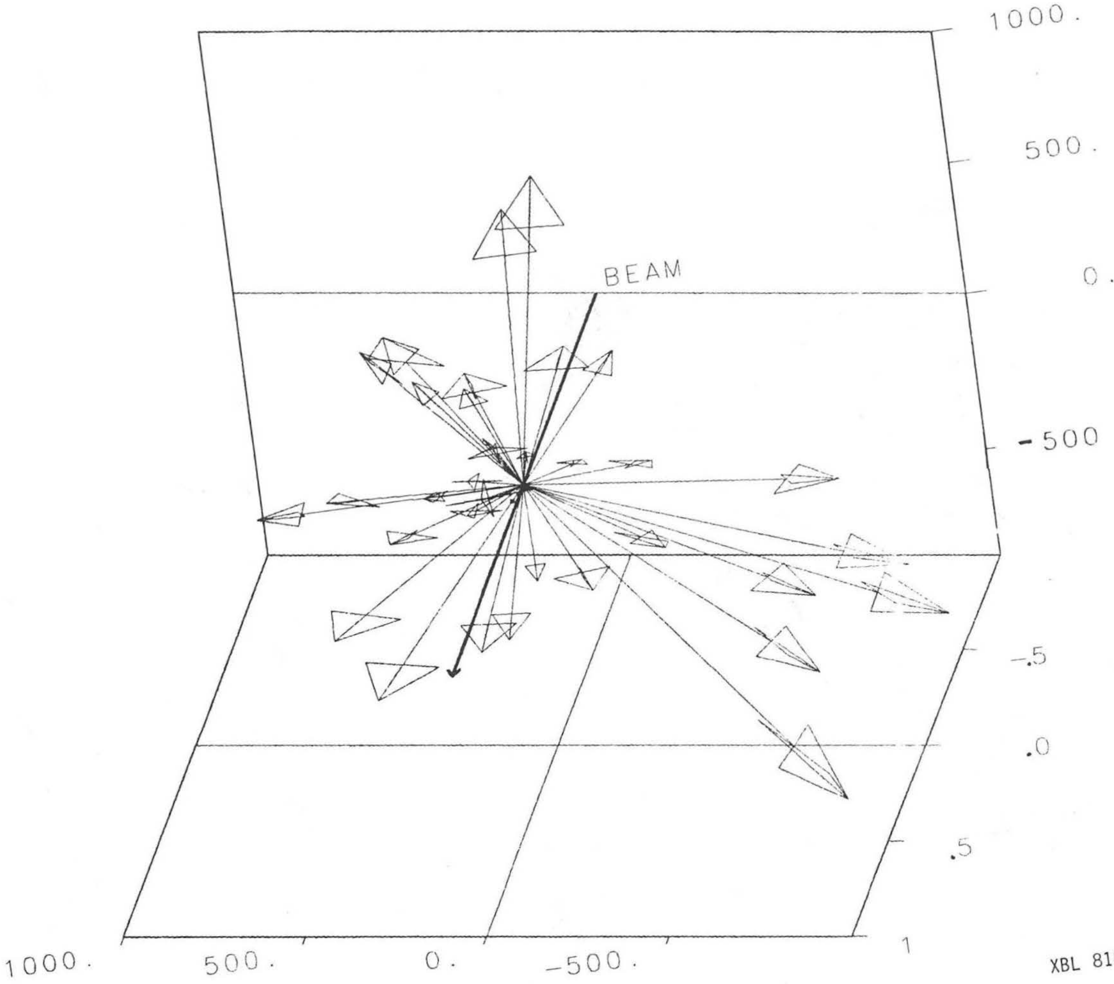

XBL 818-11281

Fig. 13

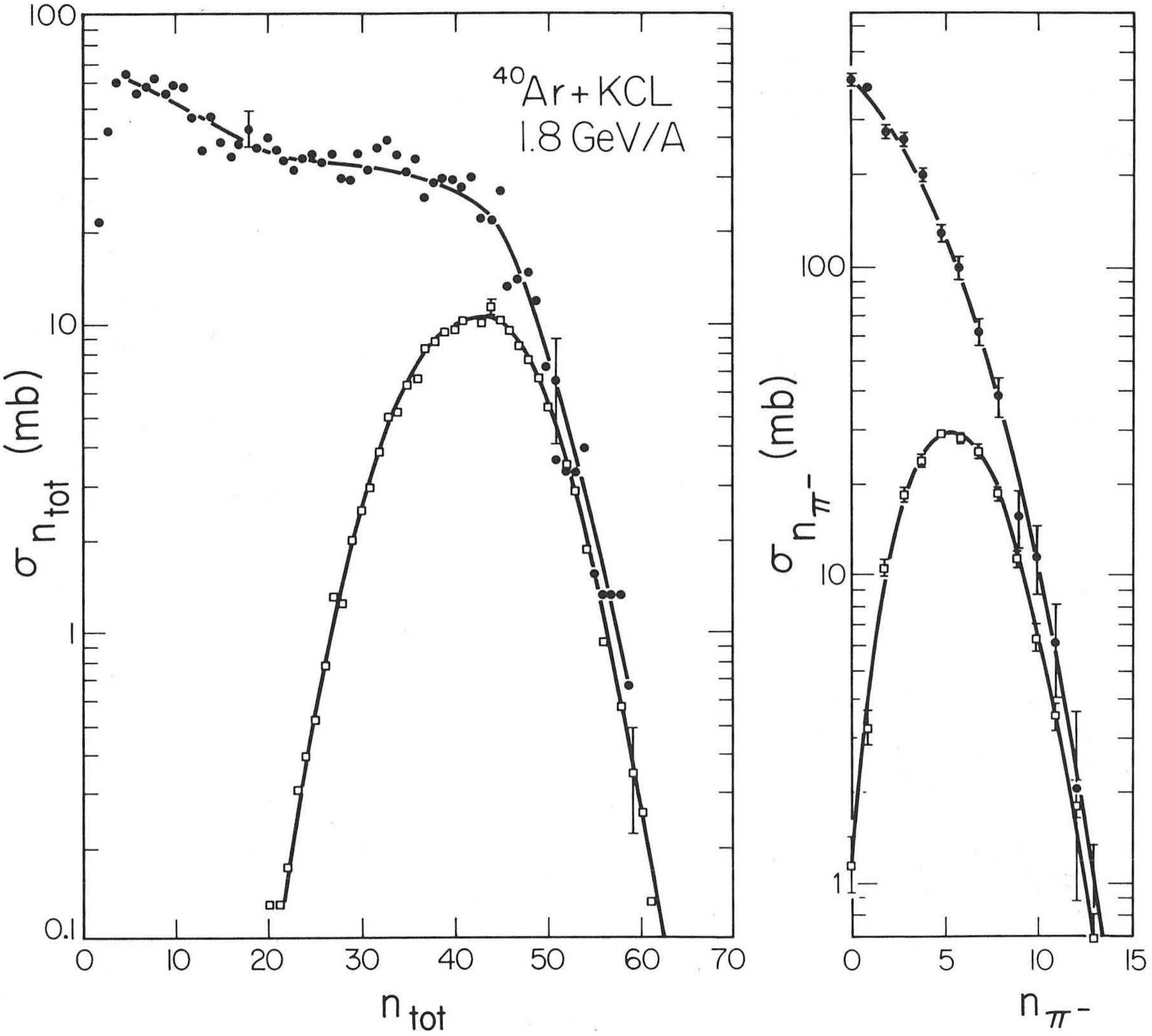

XBL 804-704

Fig. 14

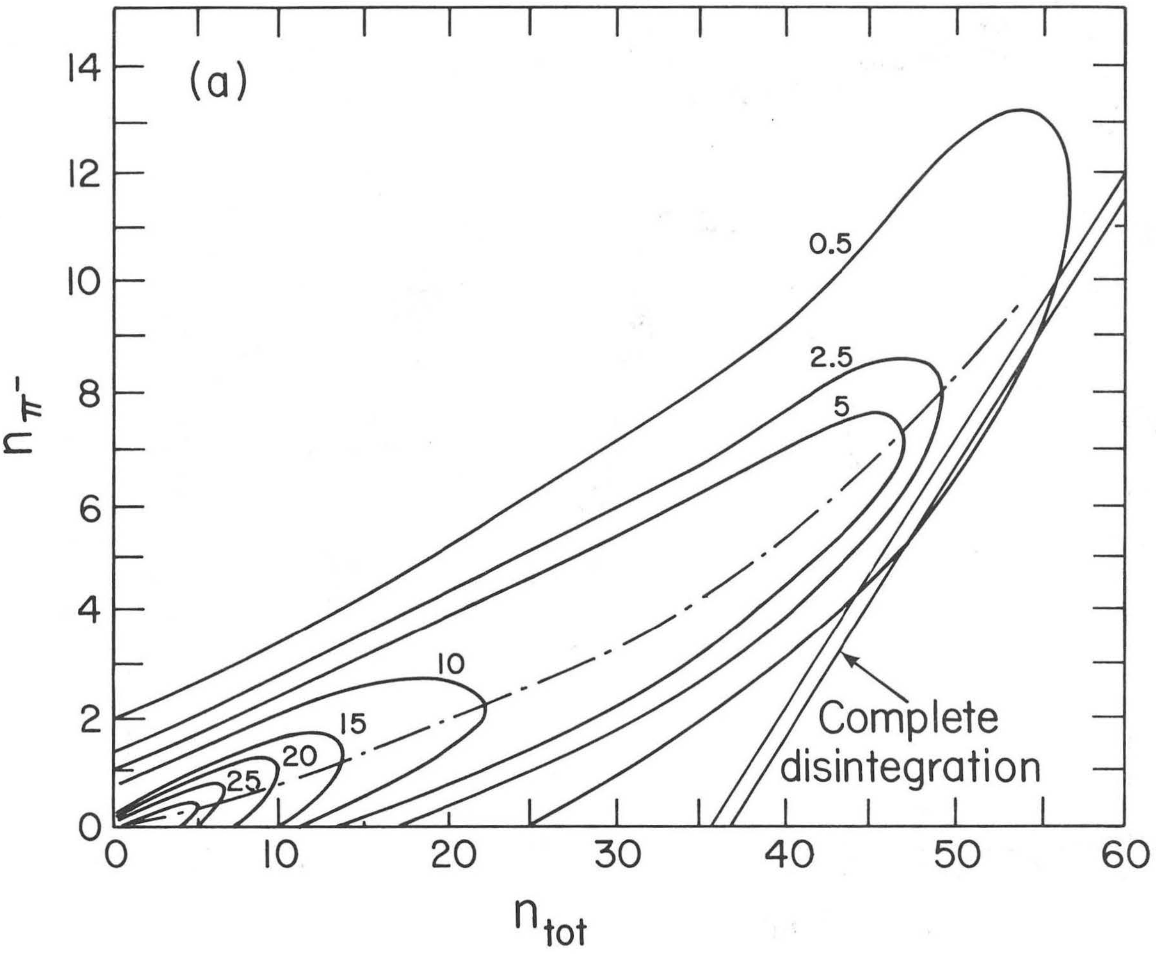

XBL 804-702

Fig. 15

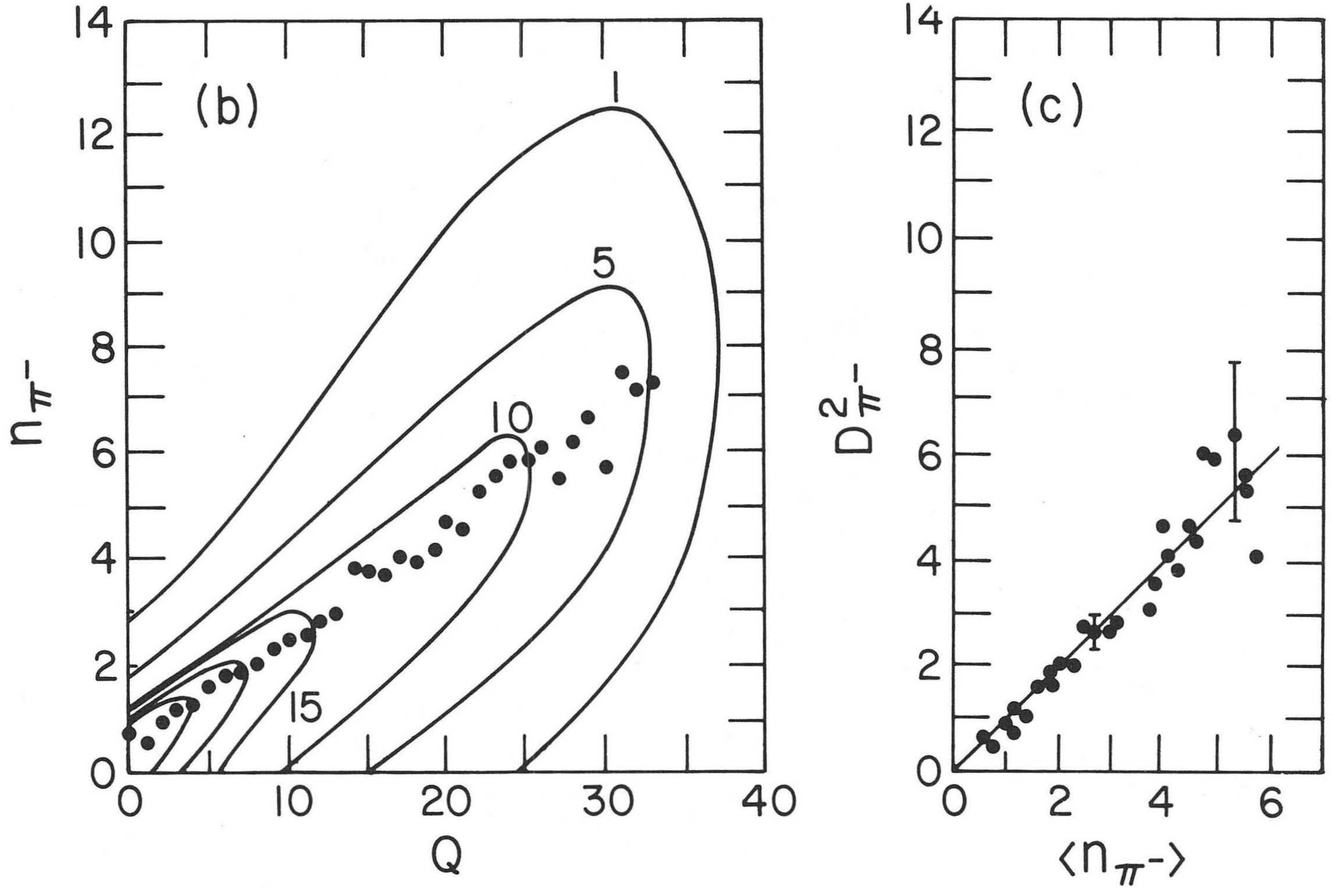

XBL 804-703

Fig. 16

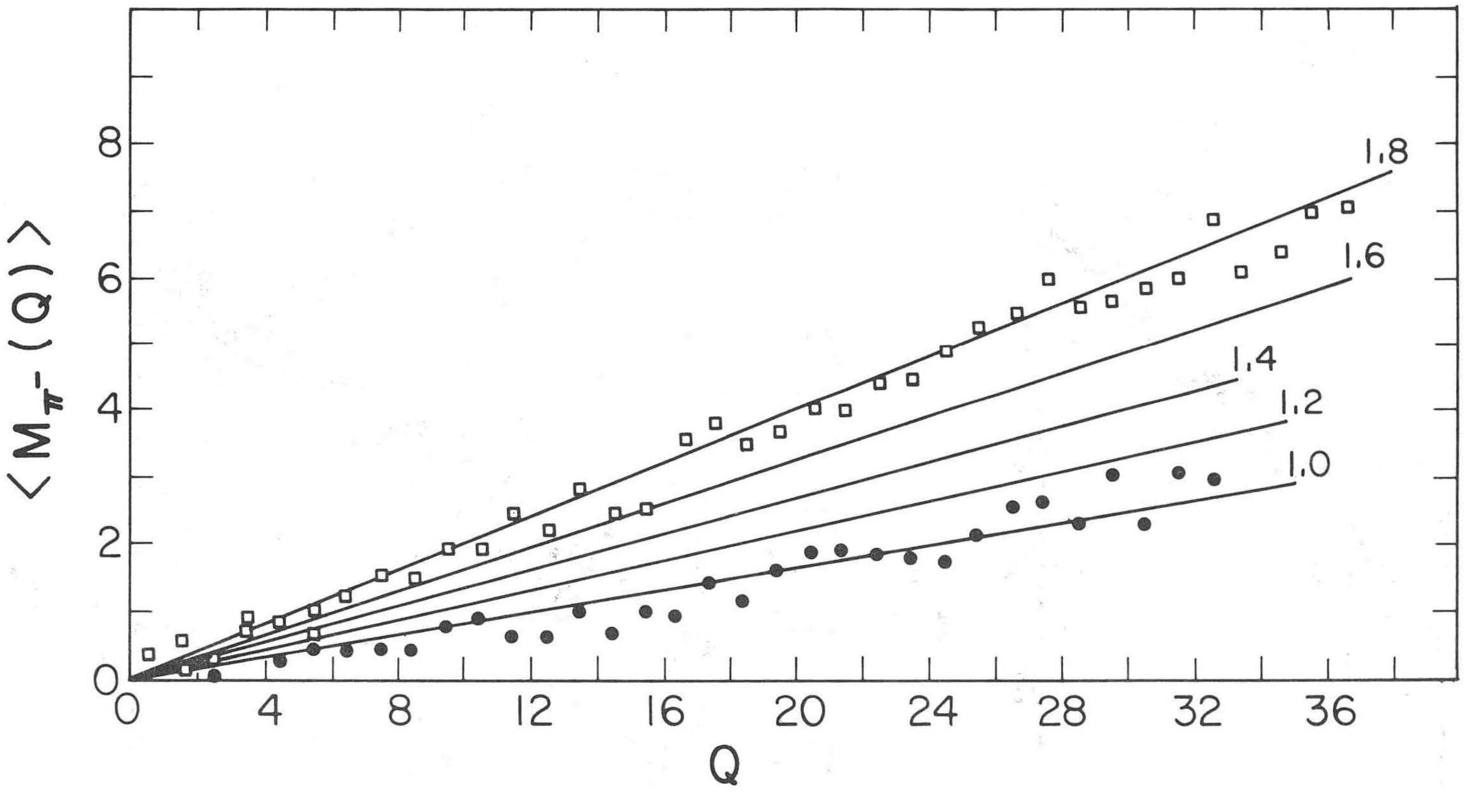

XBL804-747

Fig. 17

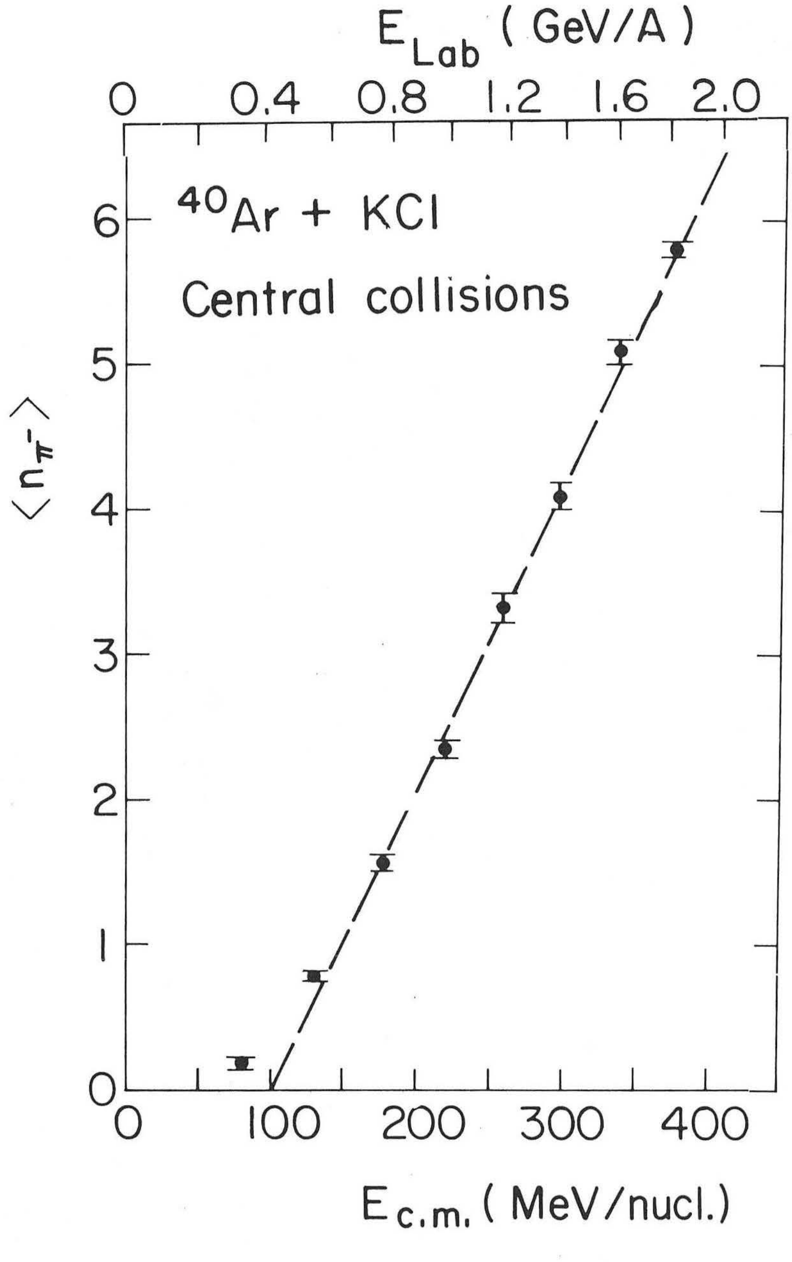
E_{Lab} (GeV/A)
0
0.4
0.8
1.2
1.6
2.0
^{40}Ar + KCl
Central collisions
$\langle n_{\pi^-} \rangle$
0
1
2
3
4
5
6
0
100
200
300
400
$E_{c.m.}$ (MeV/nucl.)
XBL 804-701

Fig. 18

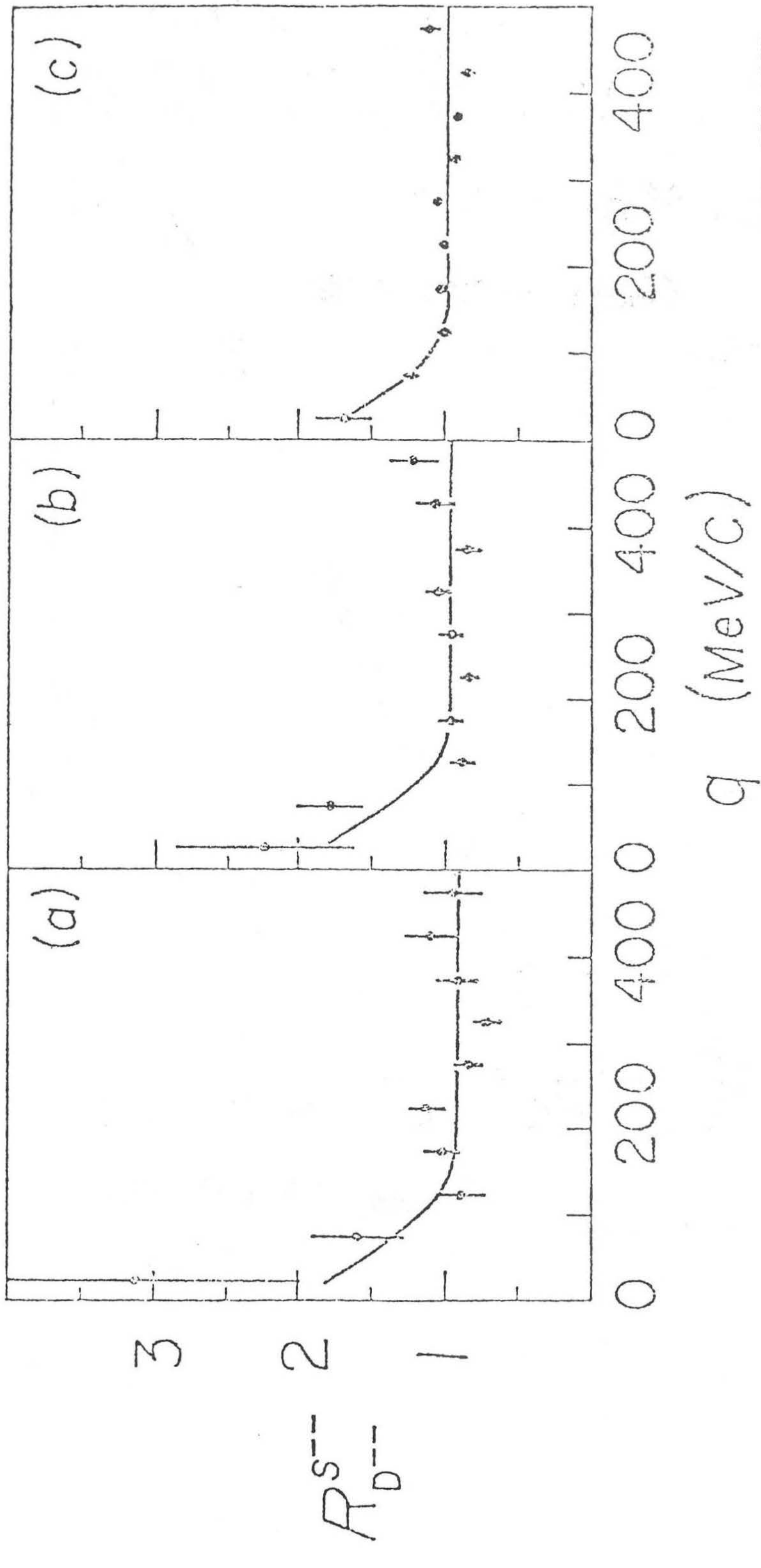

XBL 814-9335

Fig. 19

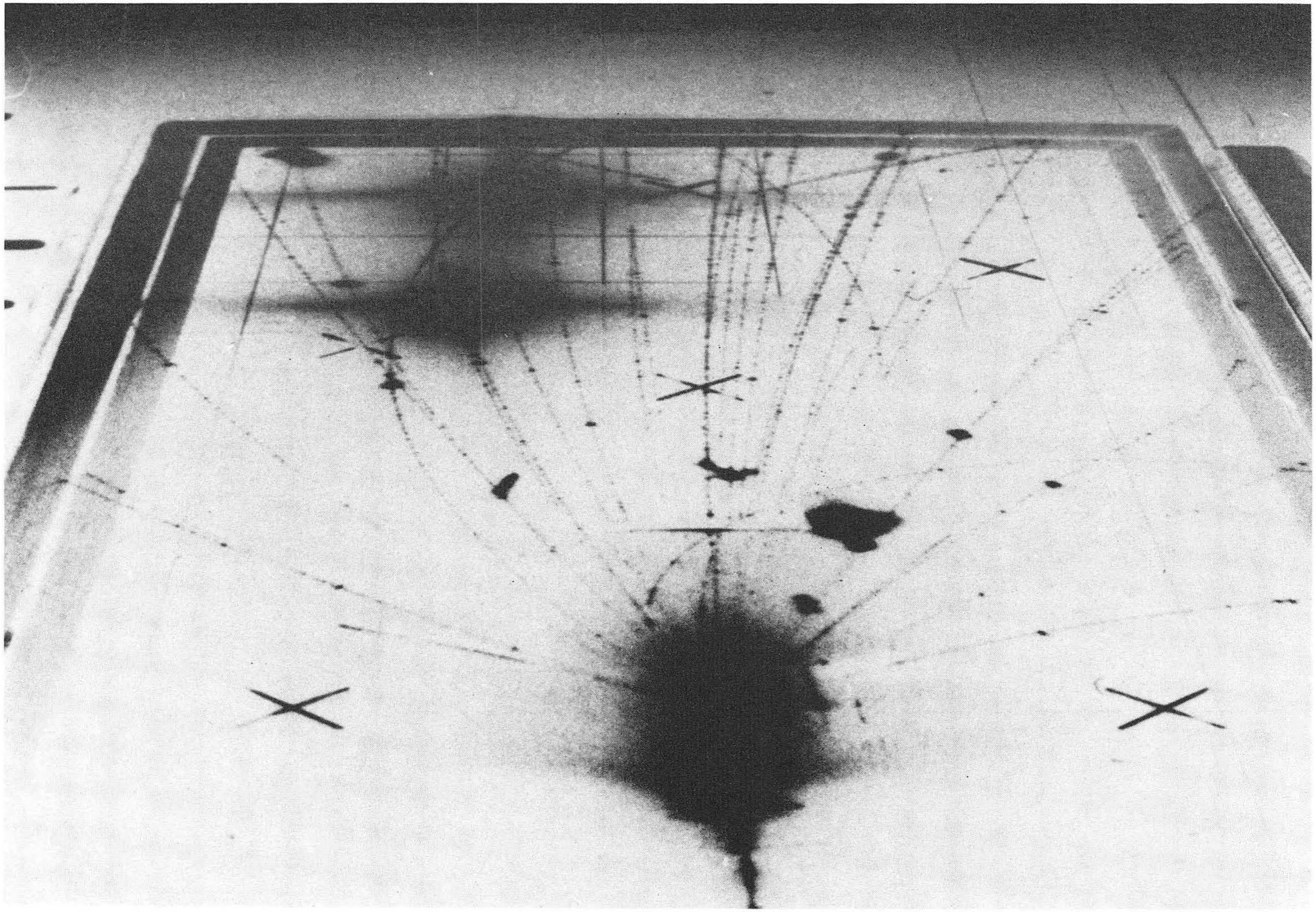

Fig. 20

XBB814-3519

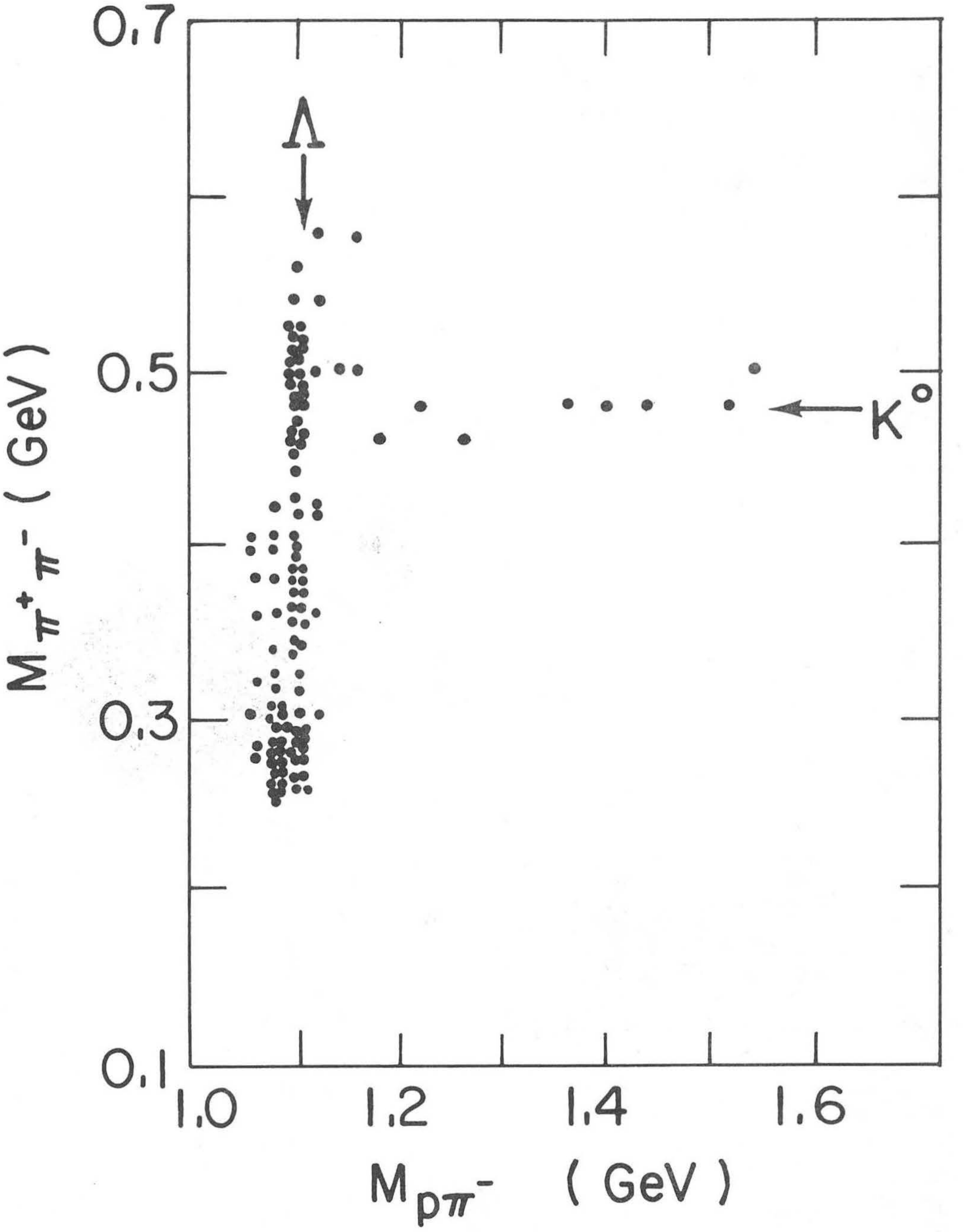

Fig. 21

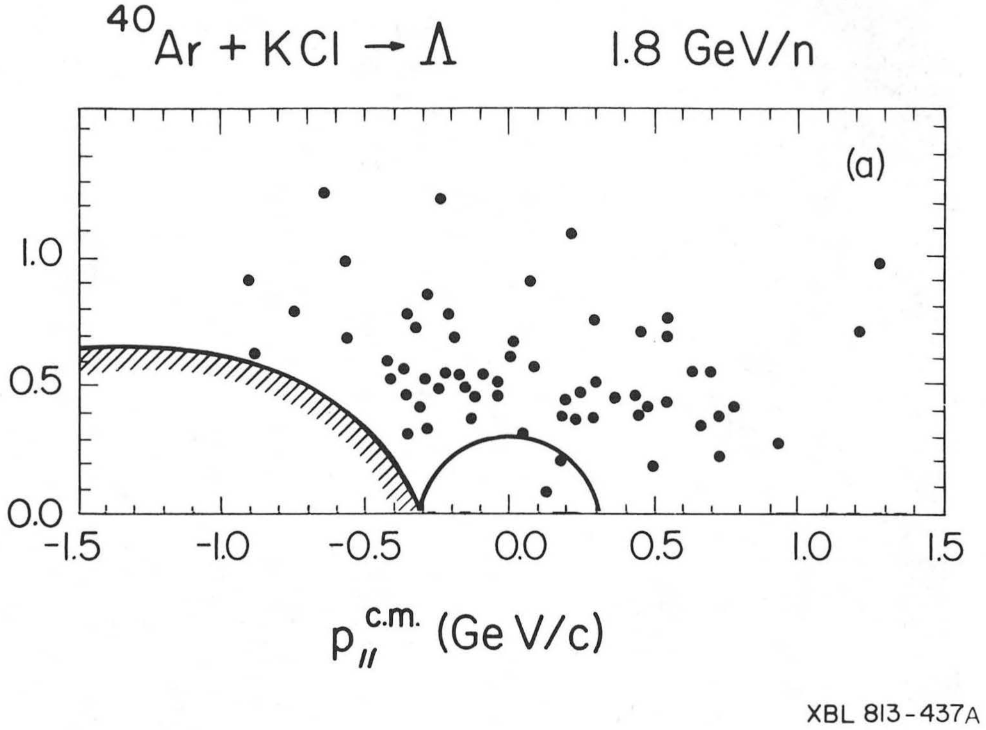
^{40}Ar + KCl → Λ
1.8 GeV/n
(a)
1.0
0.5
0.0
-1.5
-1.0
-0.5
0.0
0.5
1.0
1.5
$p_{\parallel}^{c.m.}$ (GeV/c)
XBL 813-437A

Fig. 22

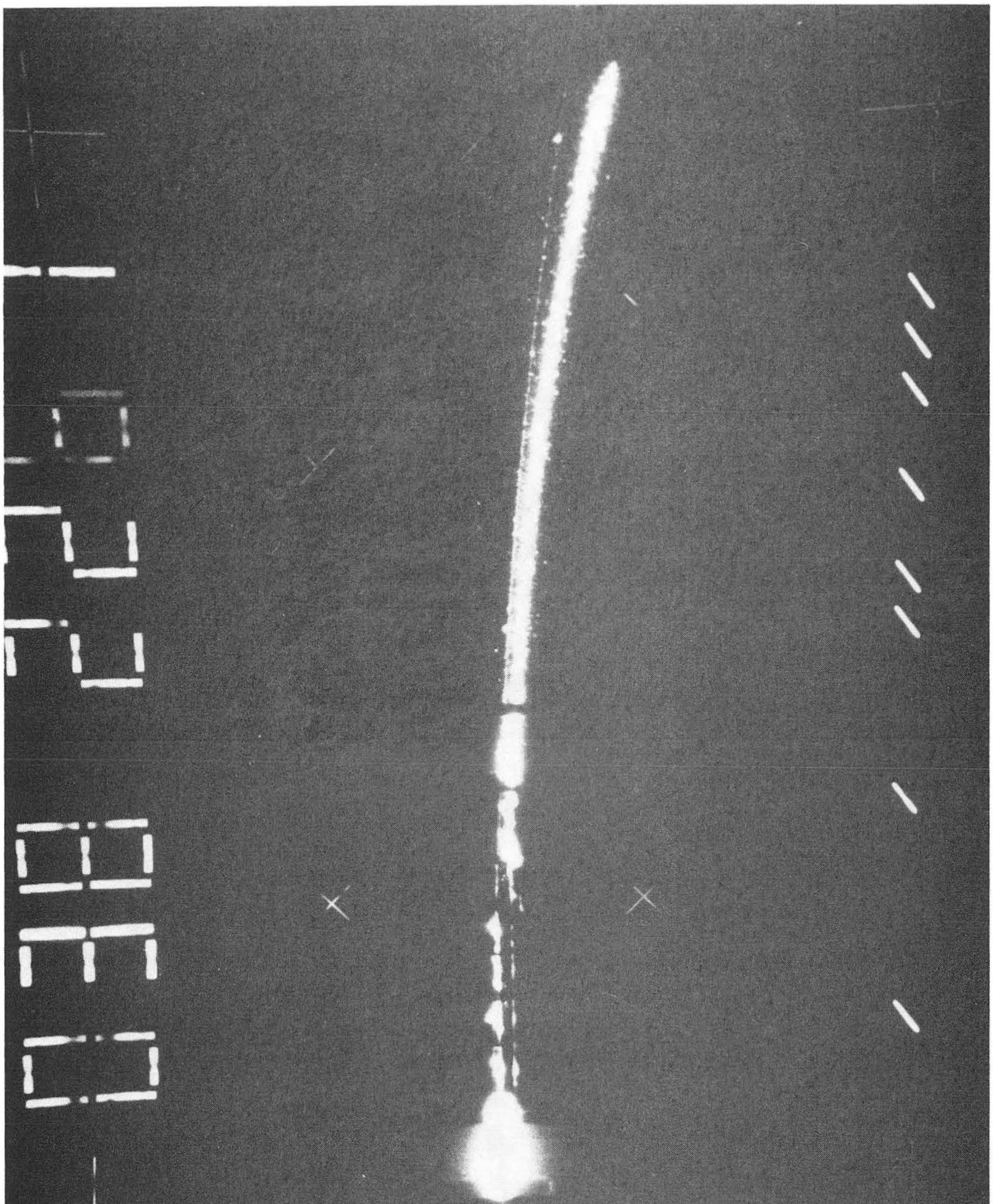

Fig. 23

XBB814-3522

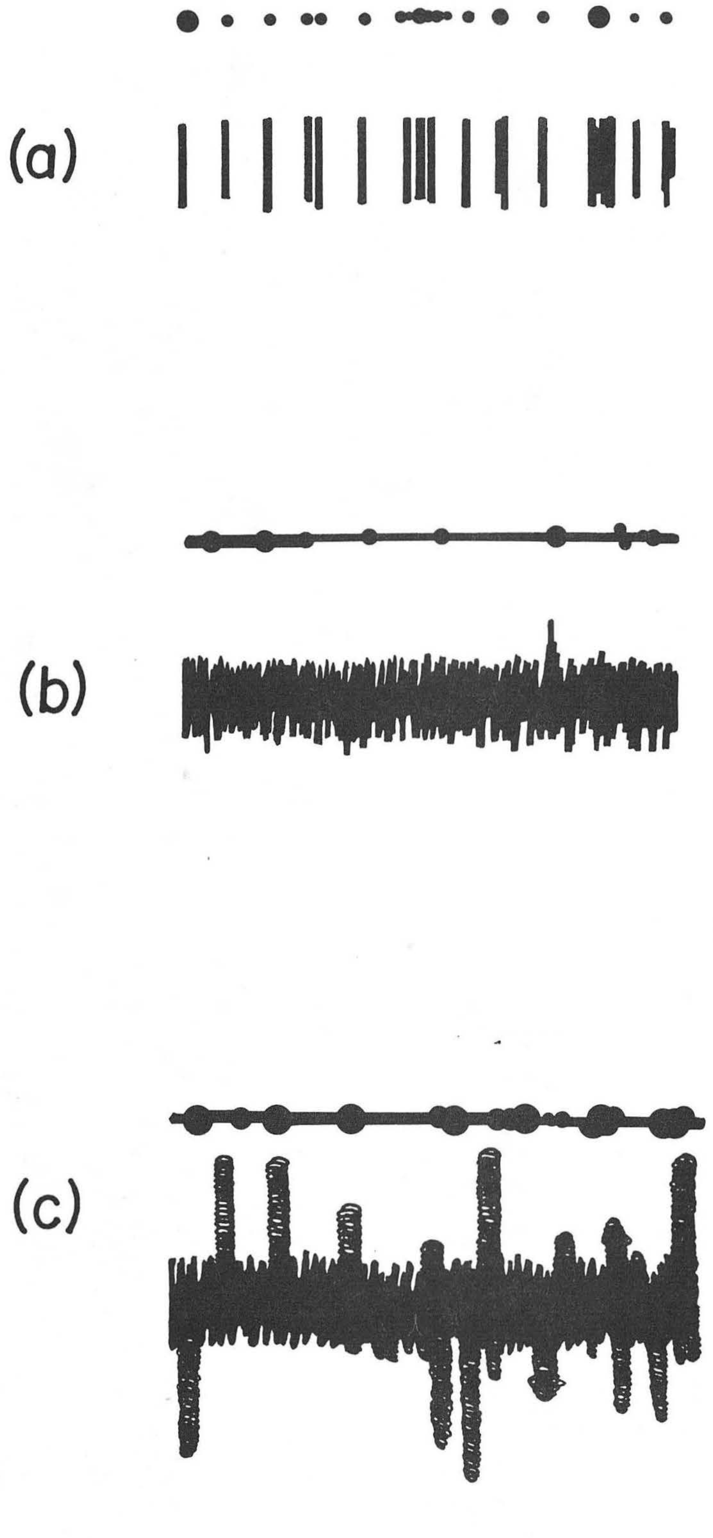

XBL 817-1057

Fig. 24

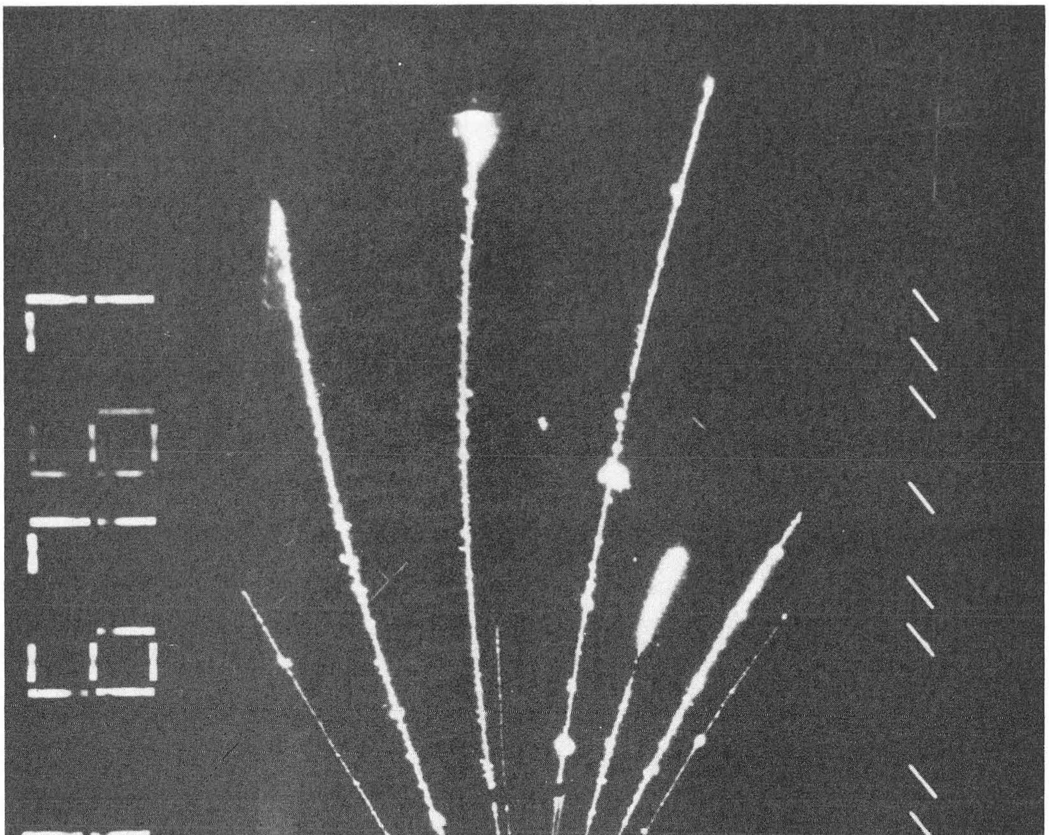

XBB814-3521

Fig. 25

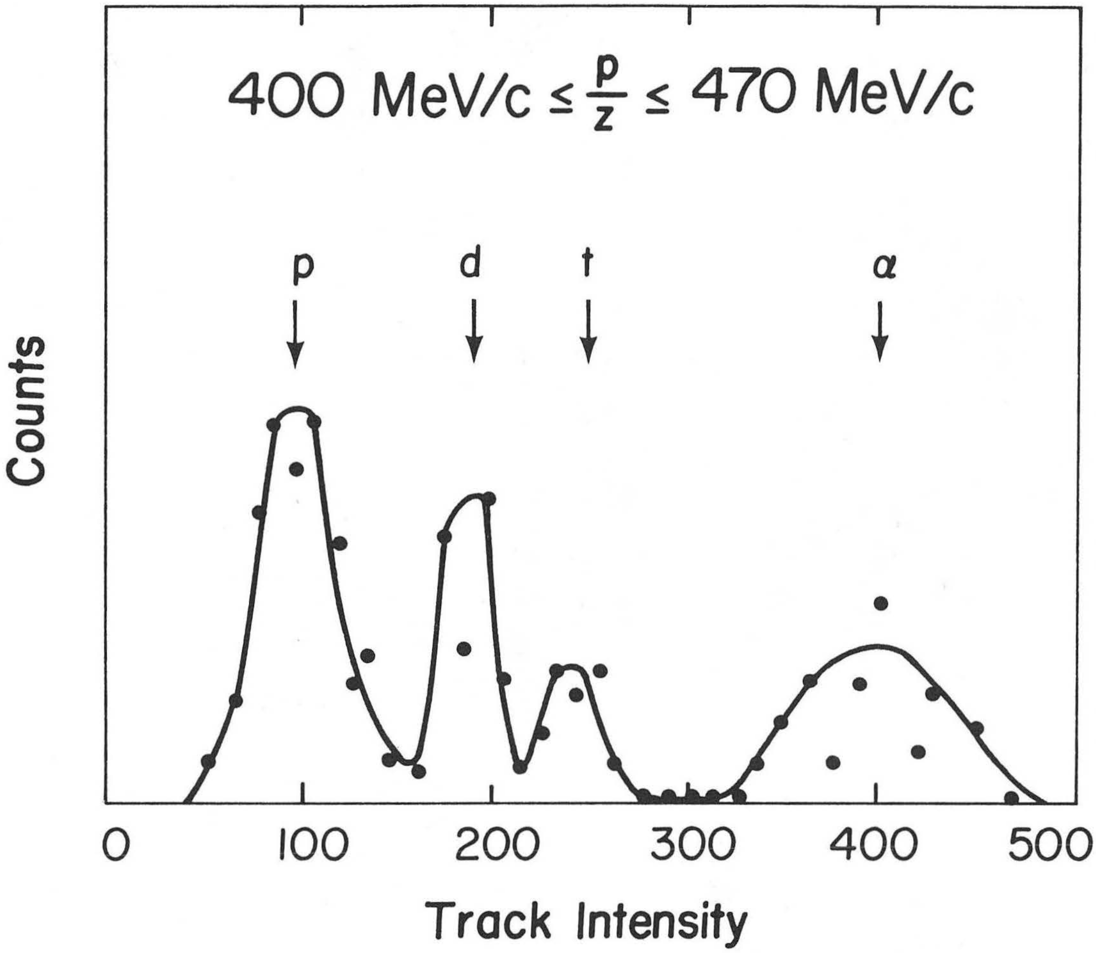

XBL817-1055

Fig. 26

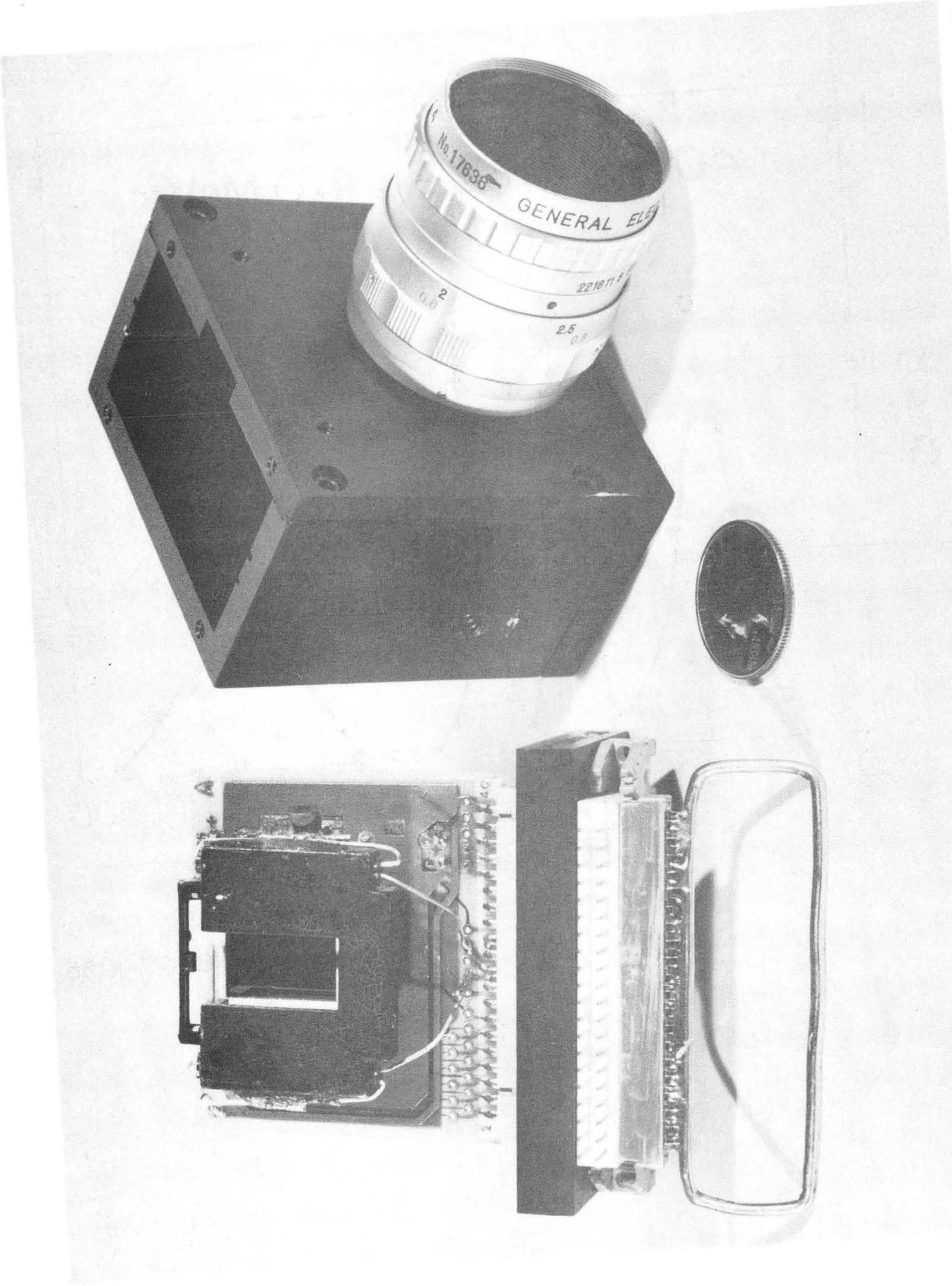

CBB817-6556

Fig. 27

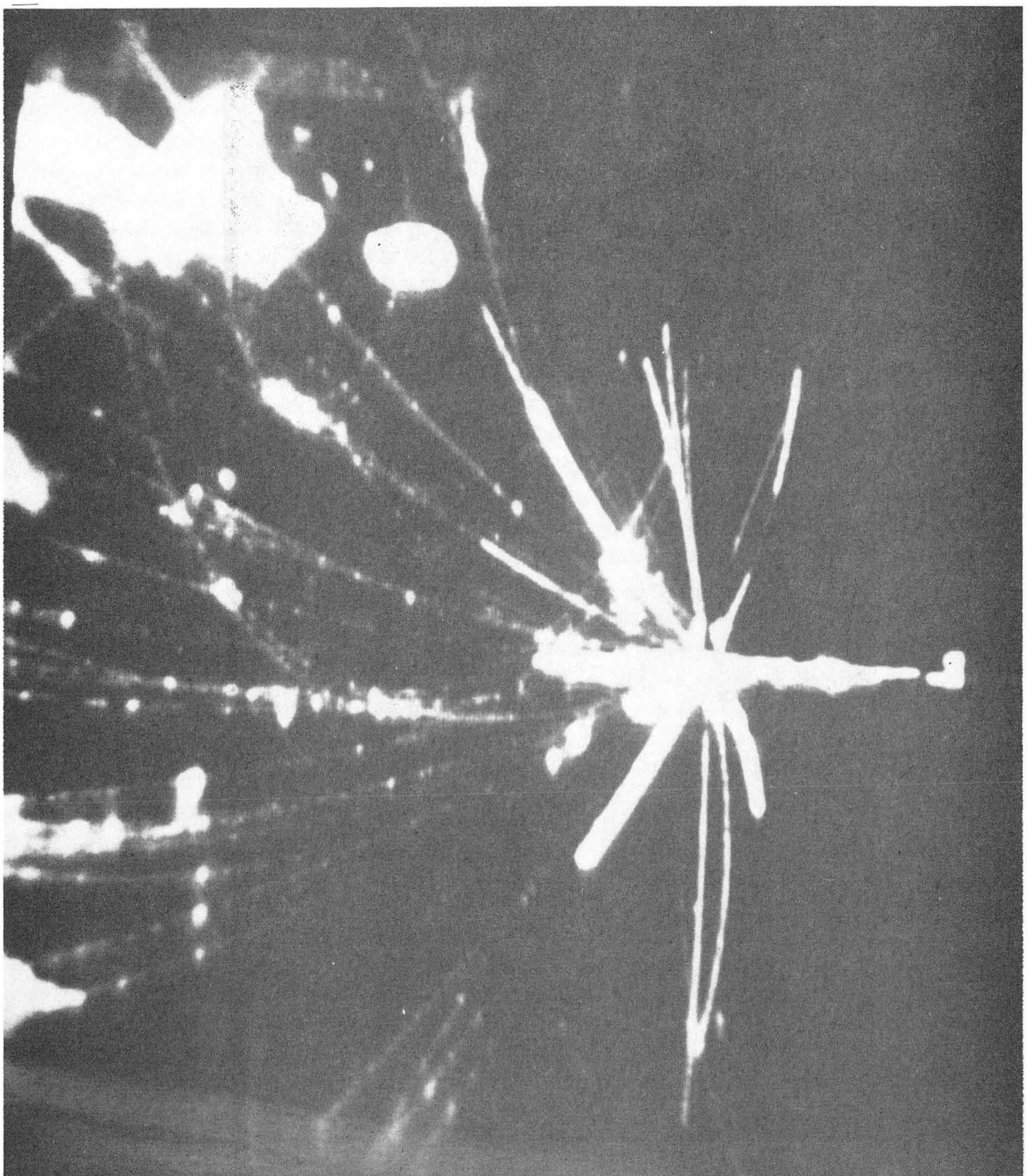

XBB816-5360

Fig. 28

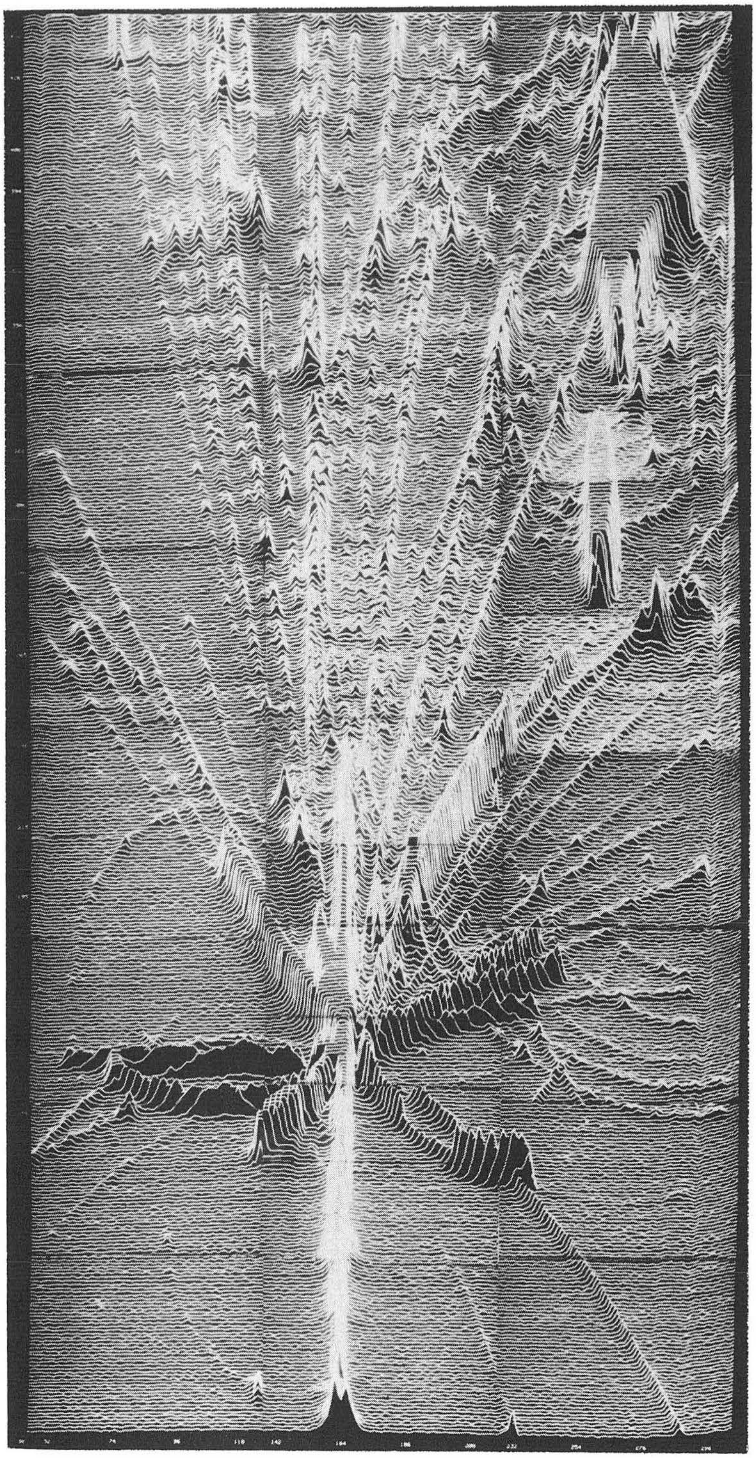

Fig. 29

XBB817-6698

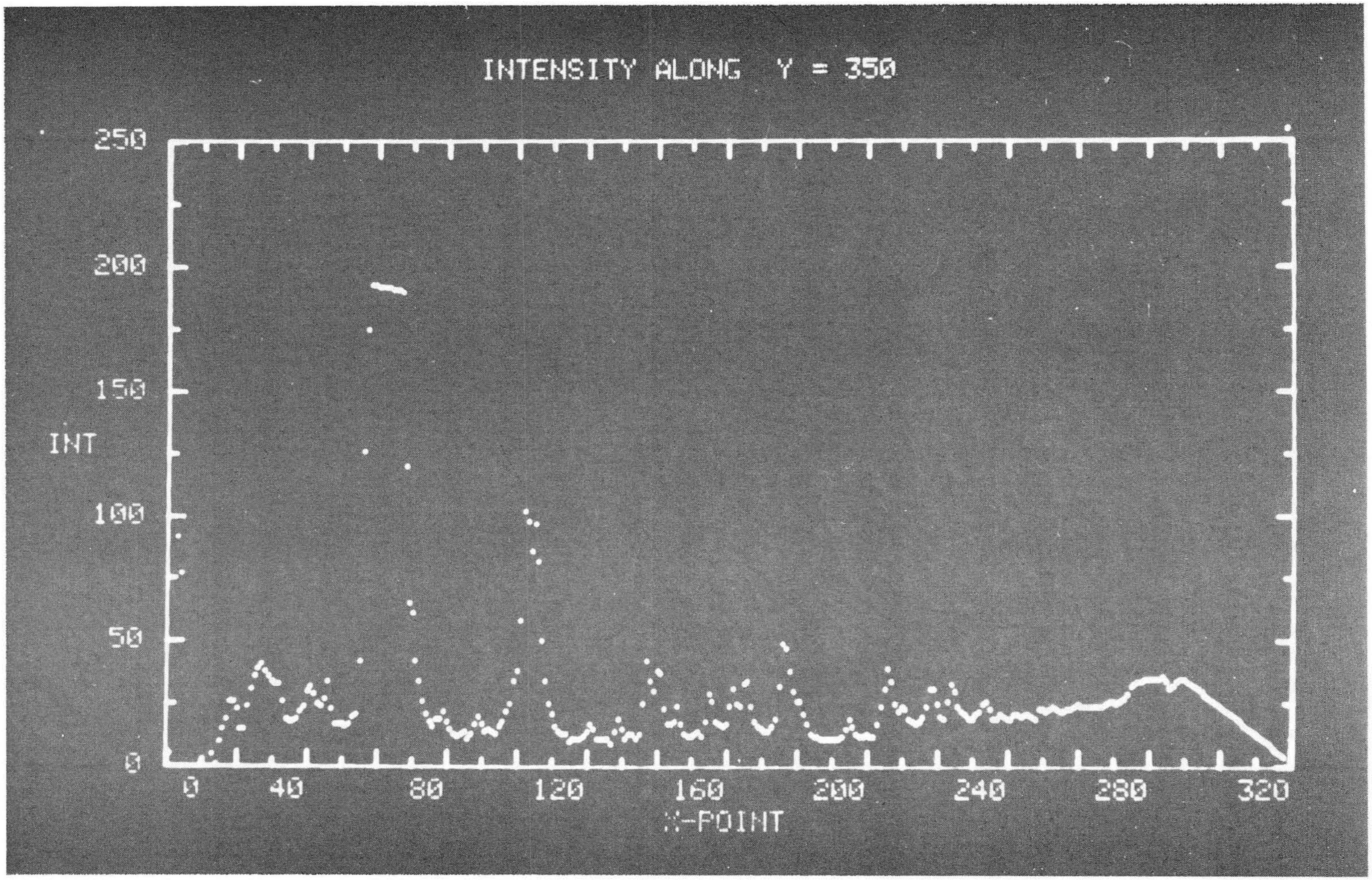

Fig. 30

XBB816-5361

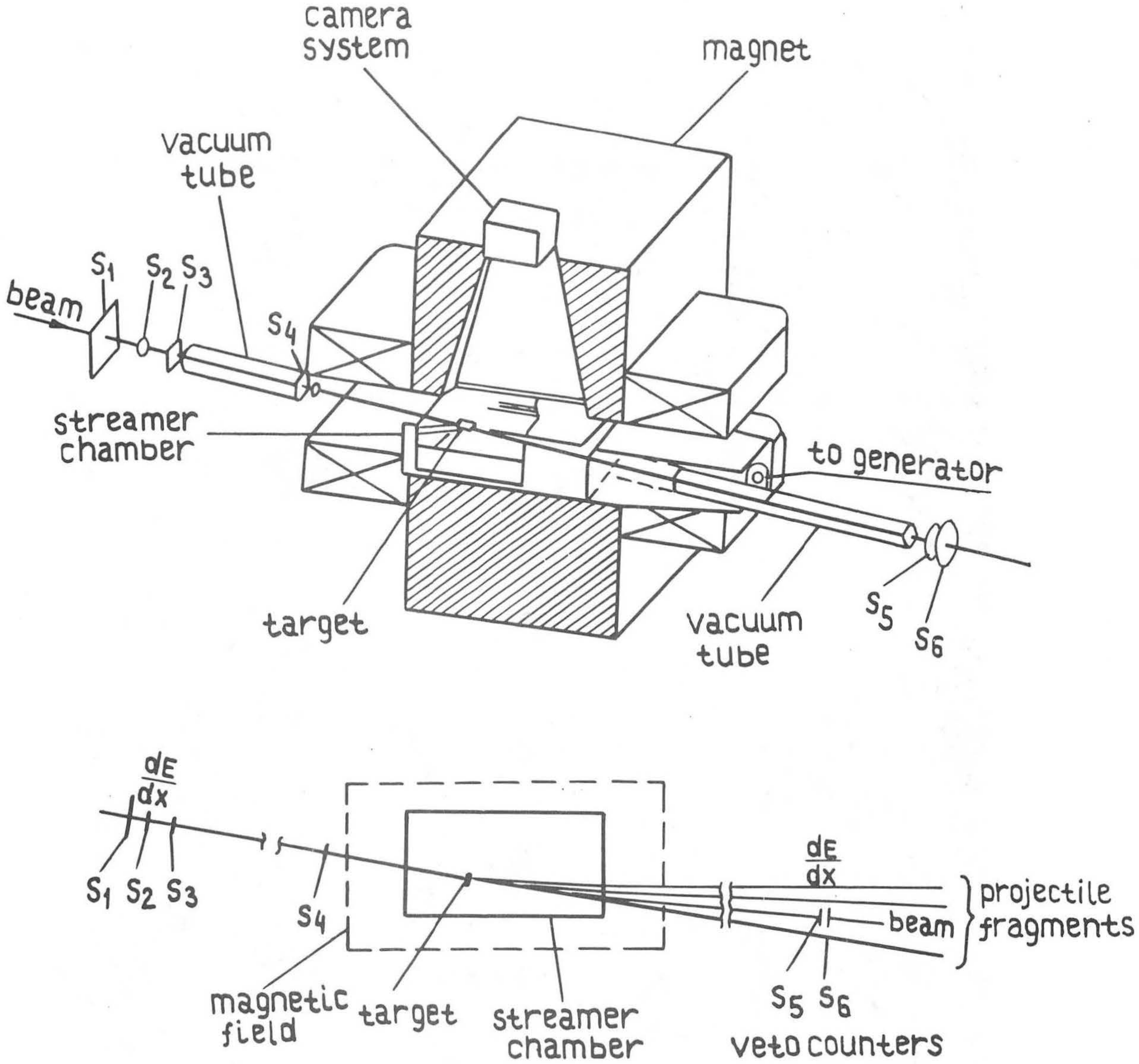

TRIGGER = $S_1 \times S_2 \times S_3 \times S_4 \times \bar{S}_5 \times \bar{S}_6$

XBL 813-8640

Fig. 31

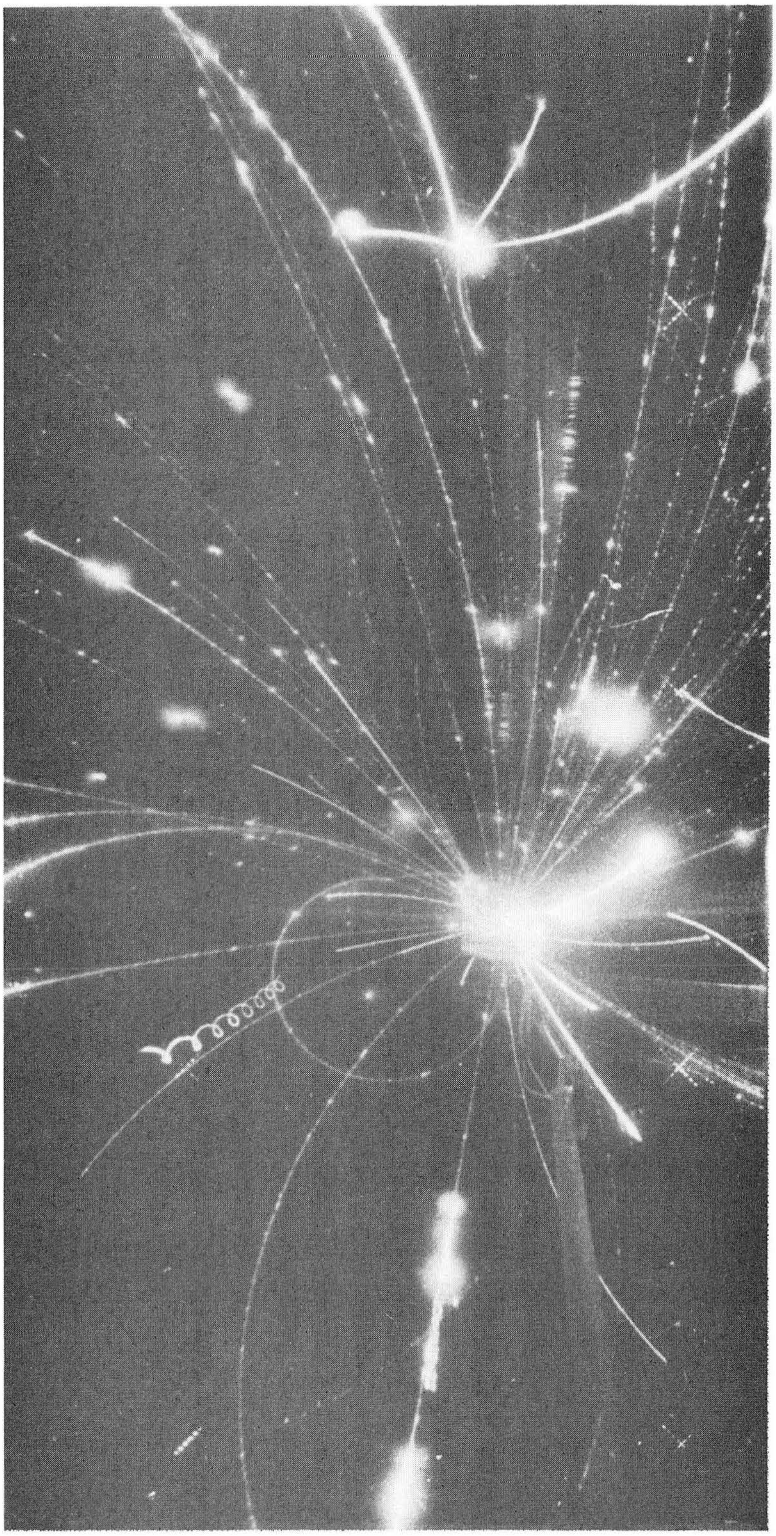

Fig. 32

XBB813-2375

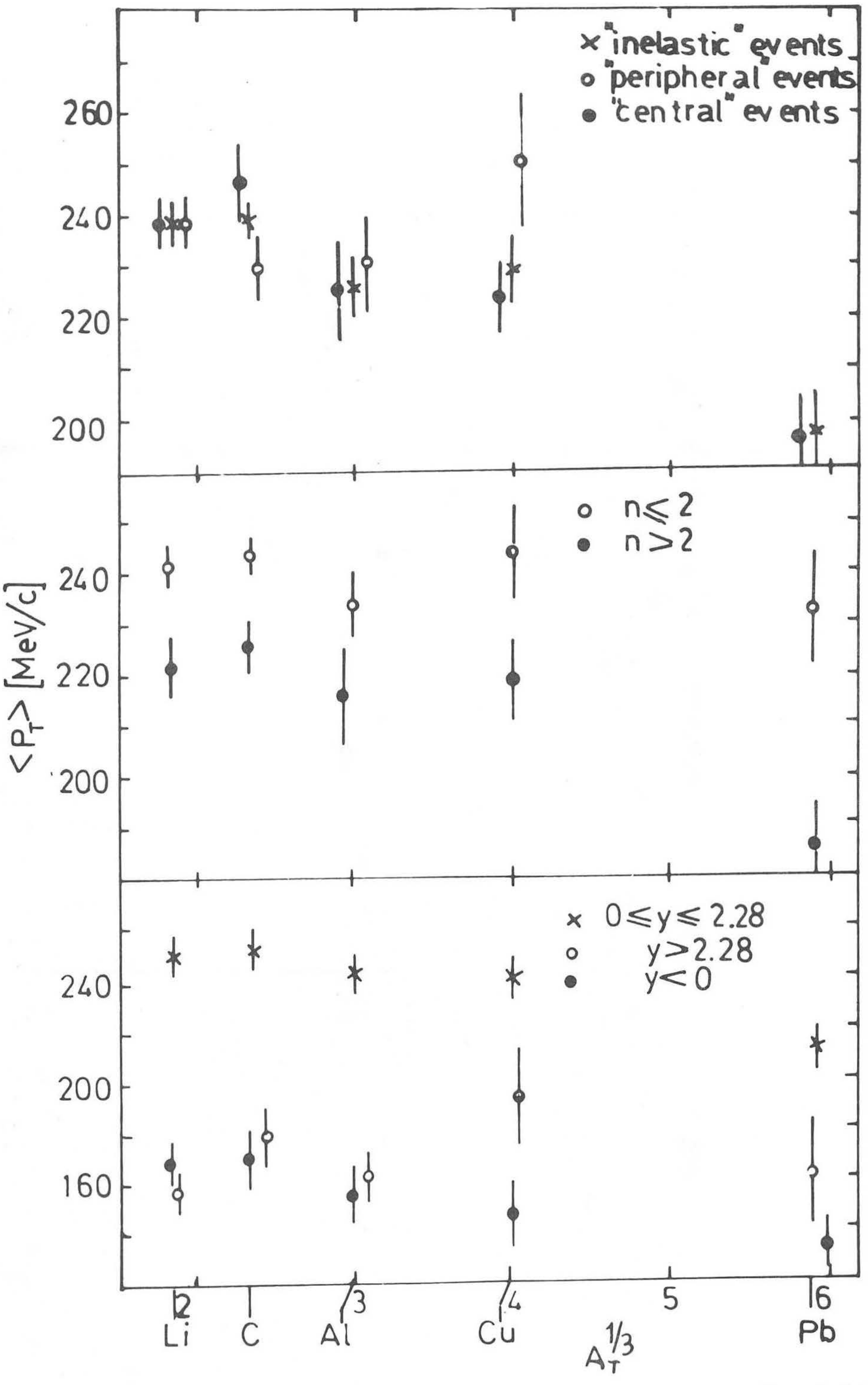

XBL 813-8641

Fig. 33

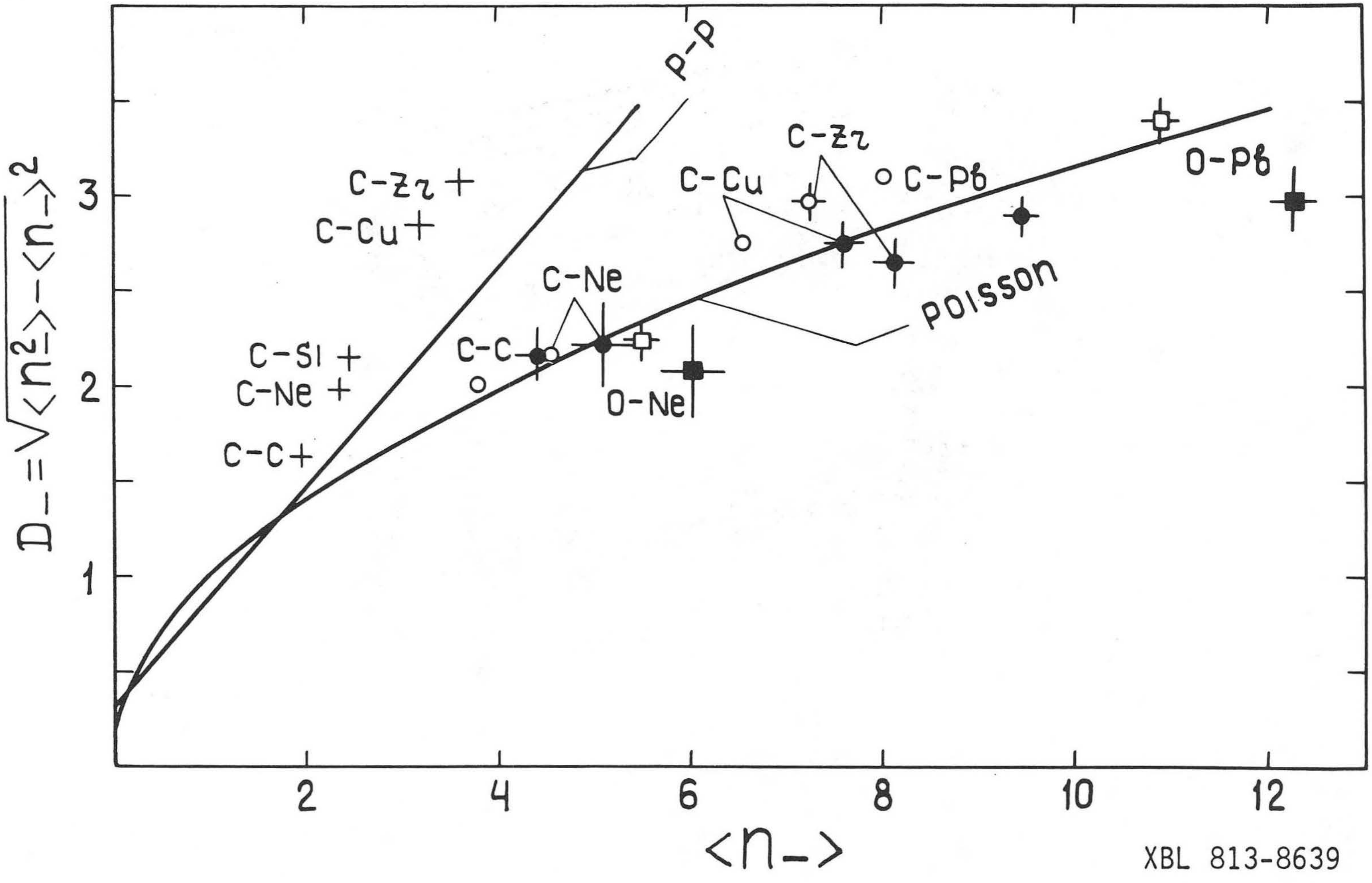
$D_- = \sqrt{\langle n_-^2 \rangle - \langle n_- \rangle^2}$
1
2
3
2
4
6
8
10
12
$\langle n_- \rangle$
p-p
C-Zr +
C-Cu +
C-Si +
C-Ne +
C-C +
C-C
C-Ne
O-Ne
C-Cu
C-Zr
C-Pb
O-Pb
POISSON
XBL 813-8639

Fig. 34

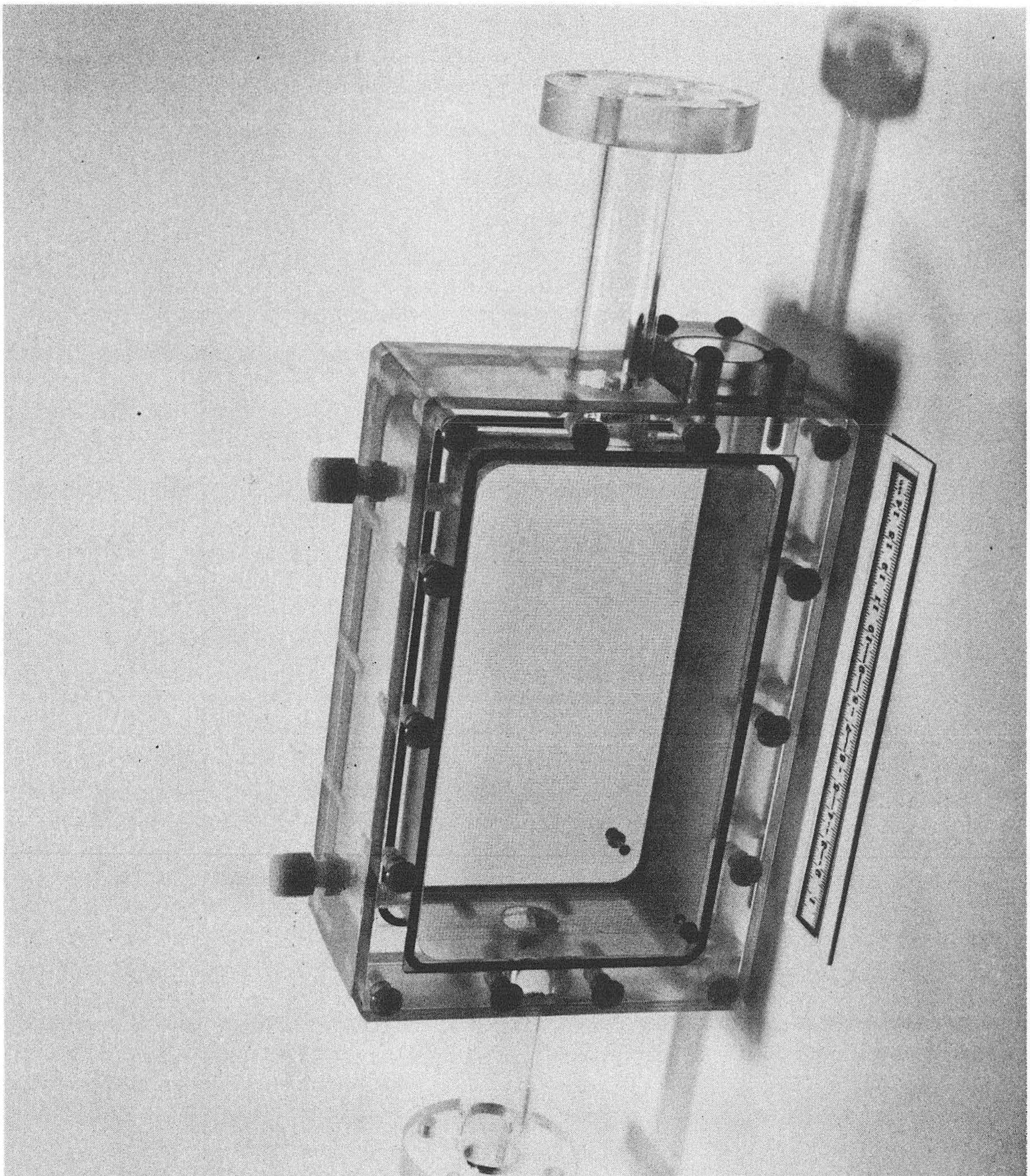

XBB782-1905

Fig. 35

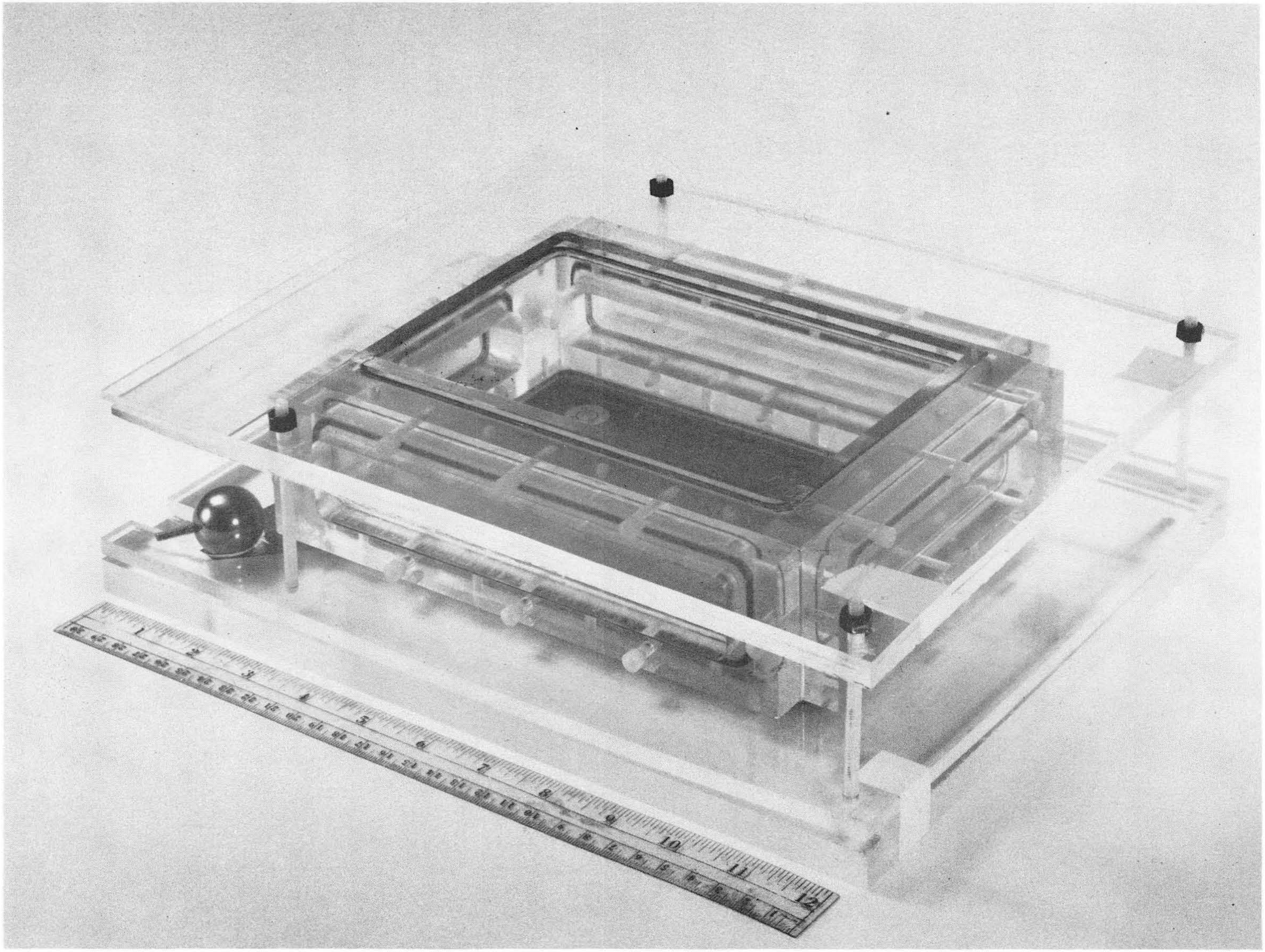

Fig. 36

XBB795-7440

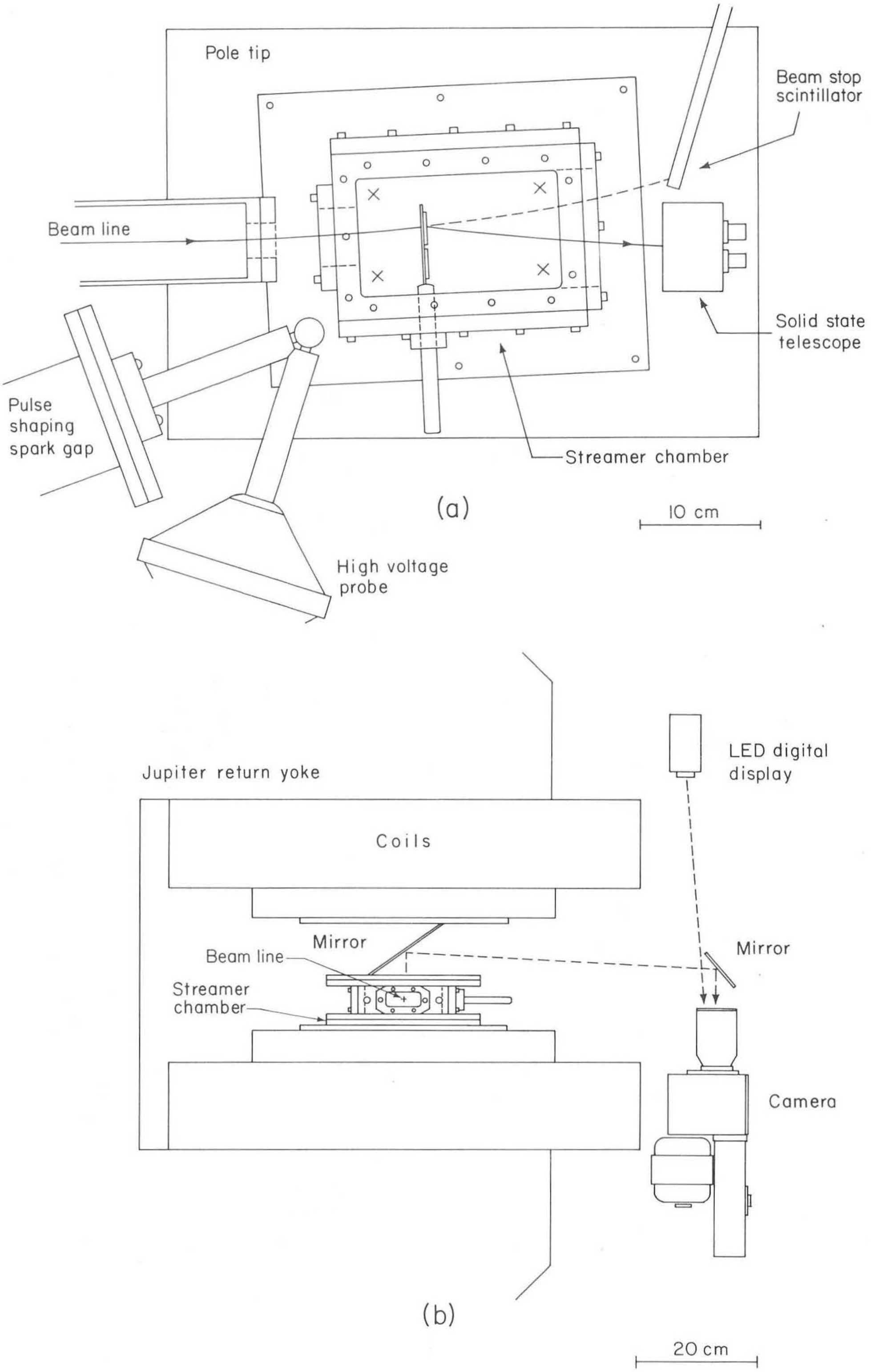

XBL 812-274

Fig. 37

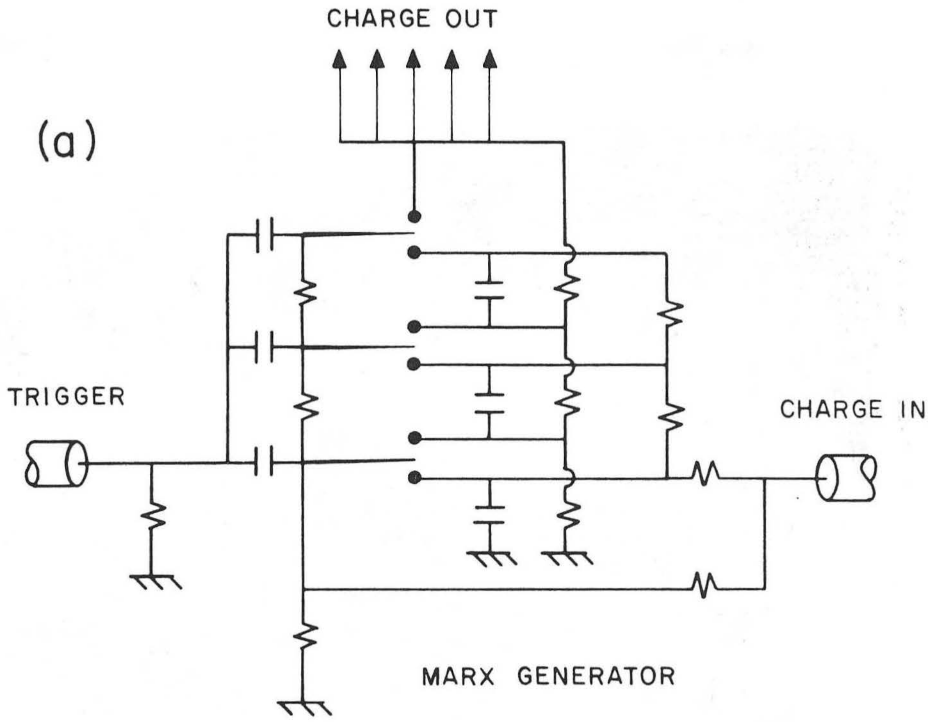

MARX GENERATOR

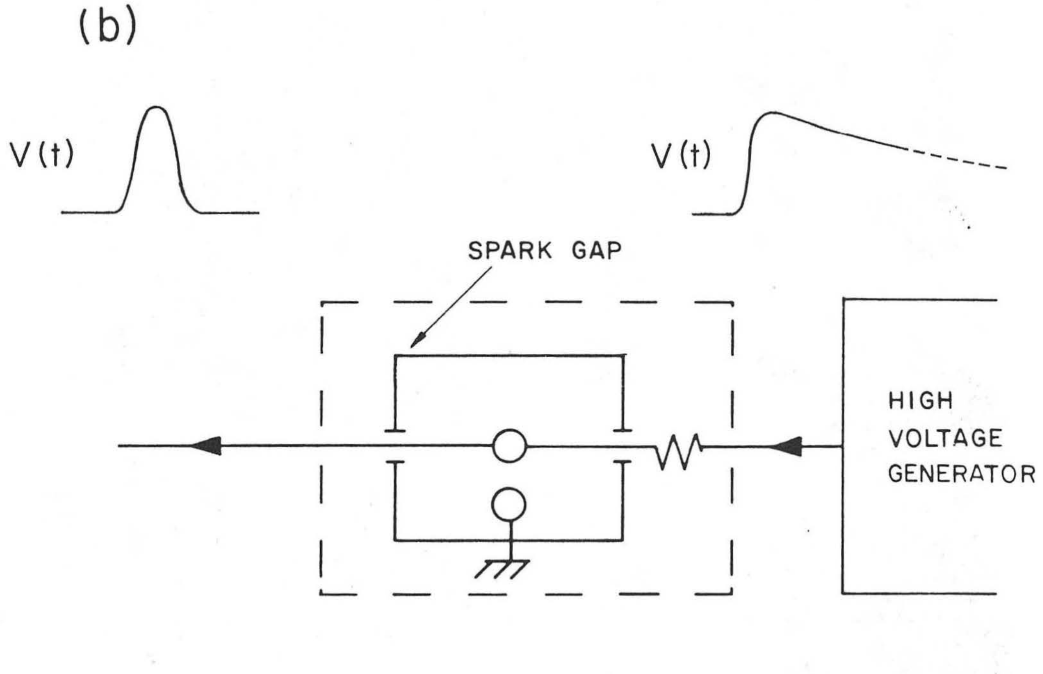

PULSE-SHAPING NETWORK

XBL 812-272

Fig. 38

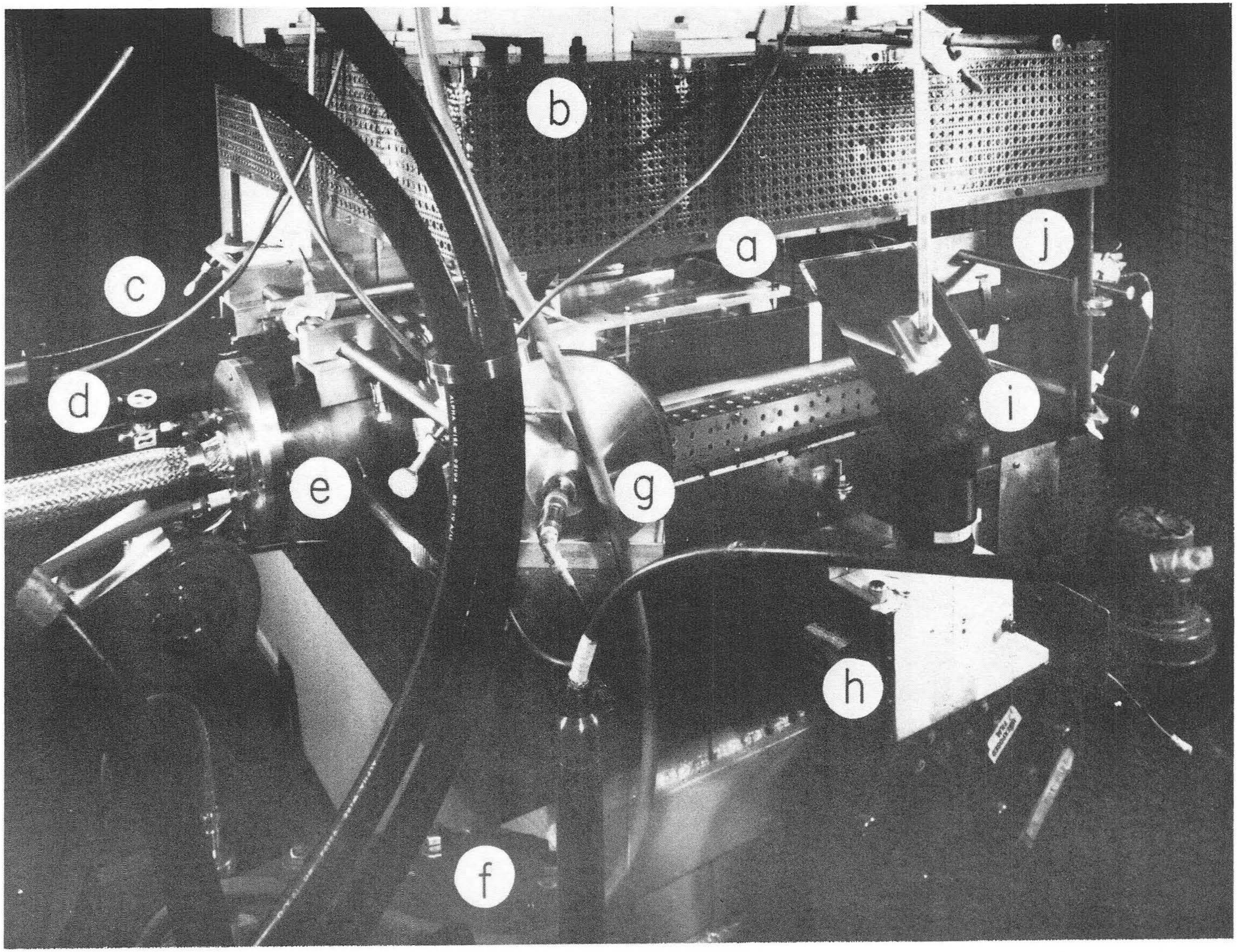

Fig. 39

XBB794-4911A

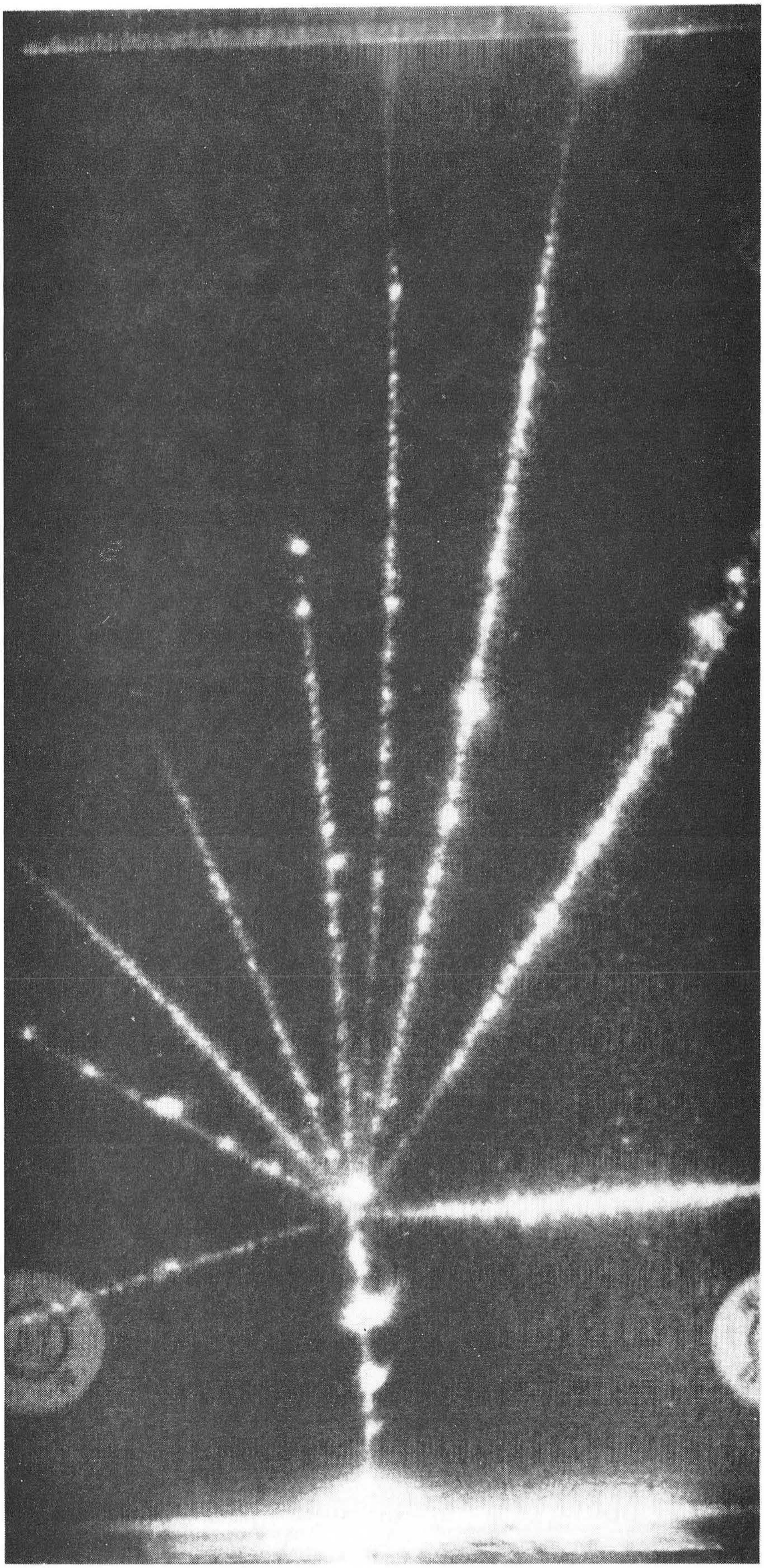

XBB798-11198

Fig. 40

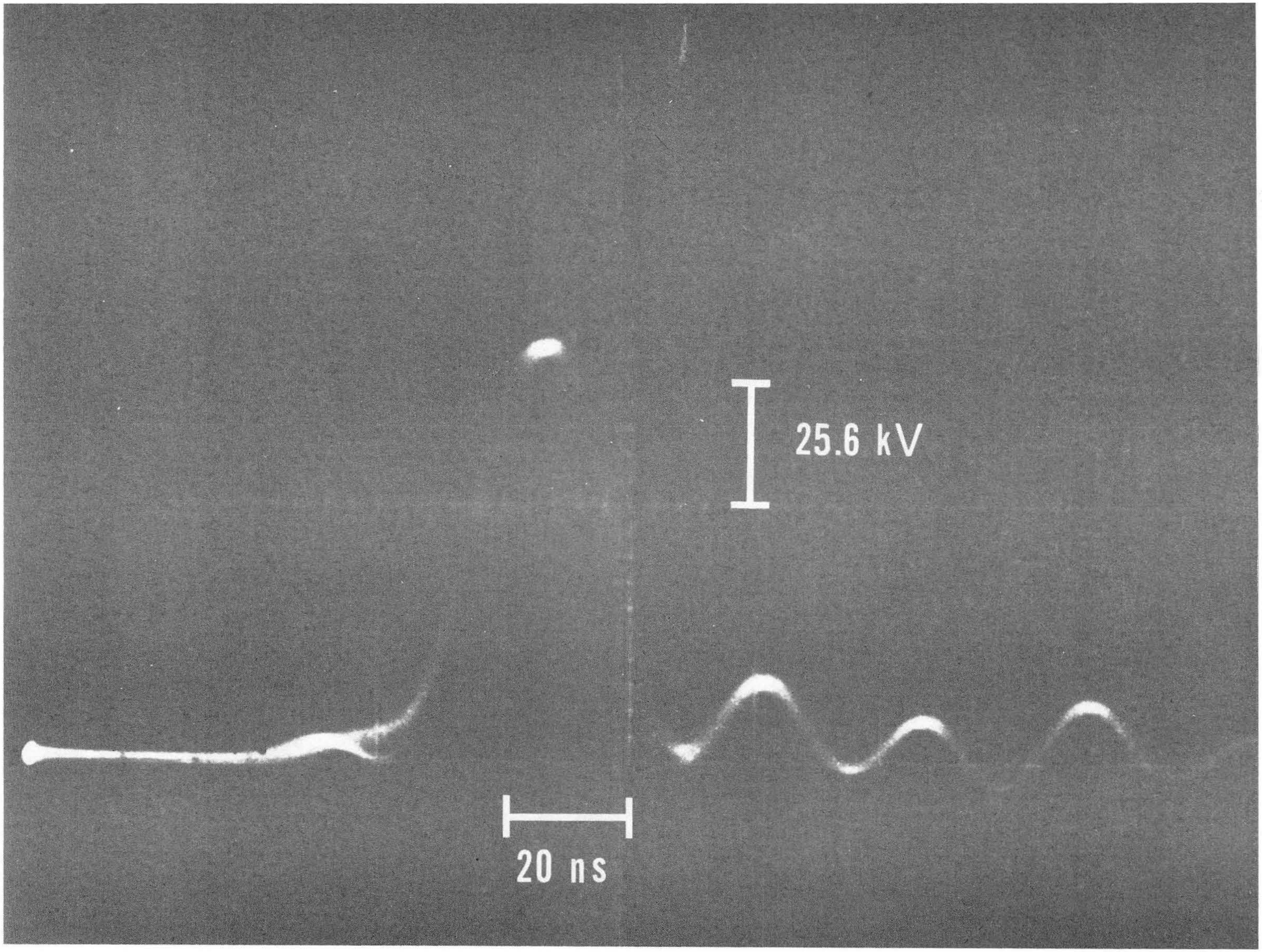

Fig. 41

XBB812-2022

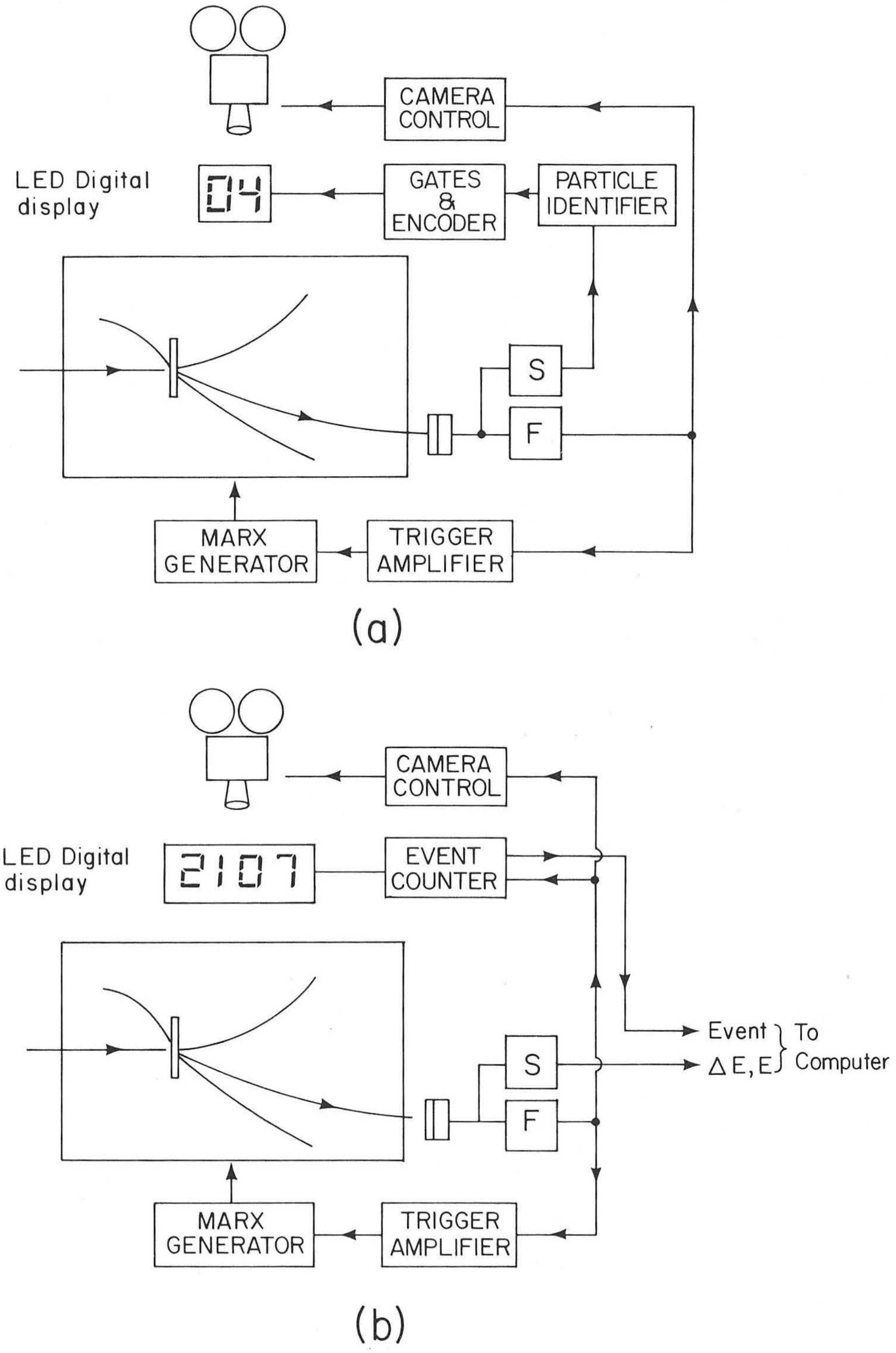

XBL 812-282

Fig. 42

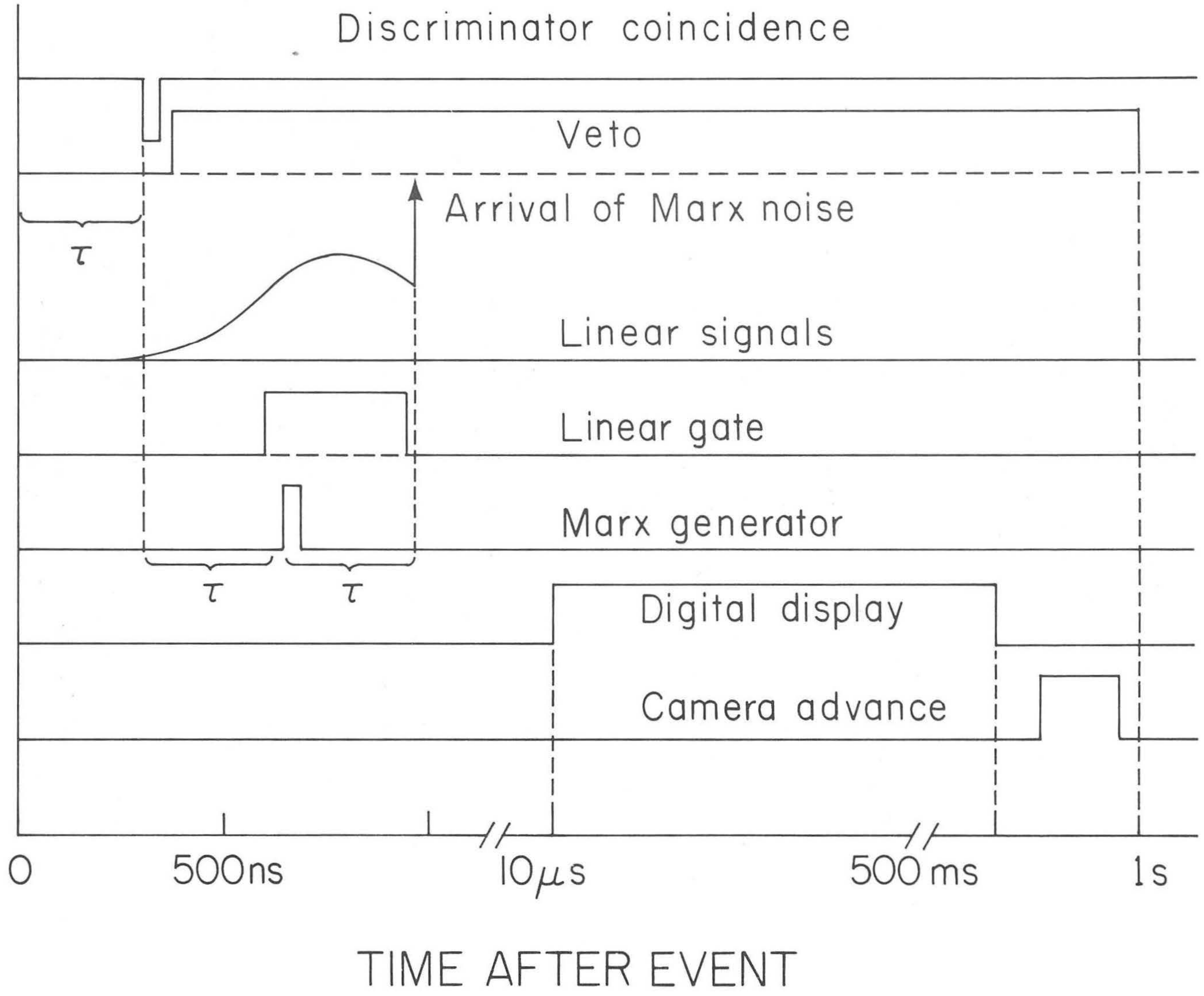

XBL-812-281

Fig. 43

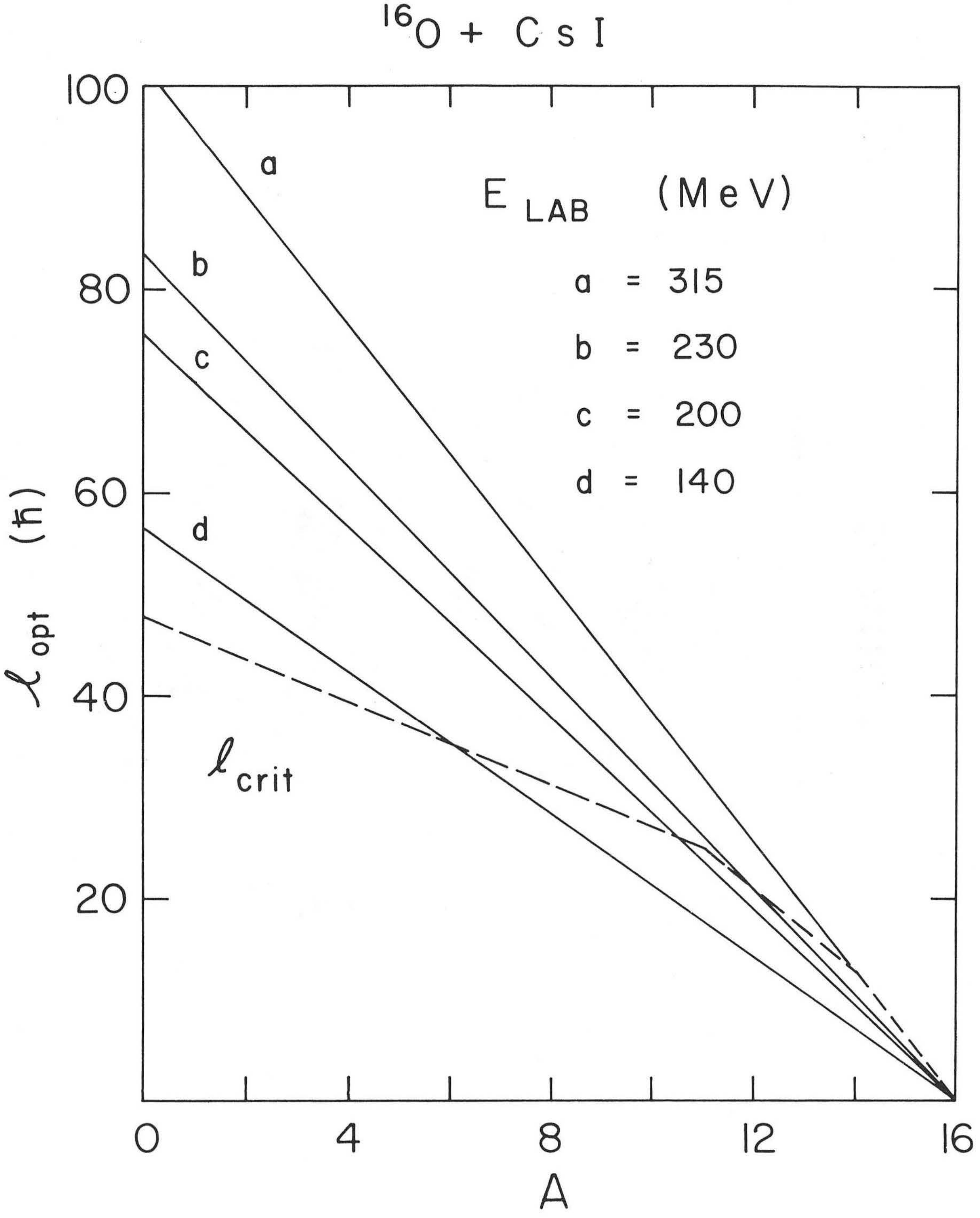

XBL-812-278

Fig. 44

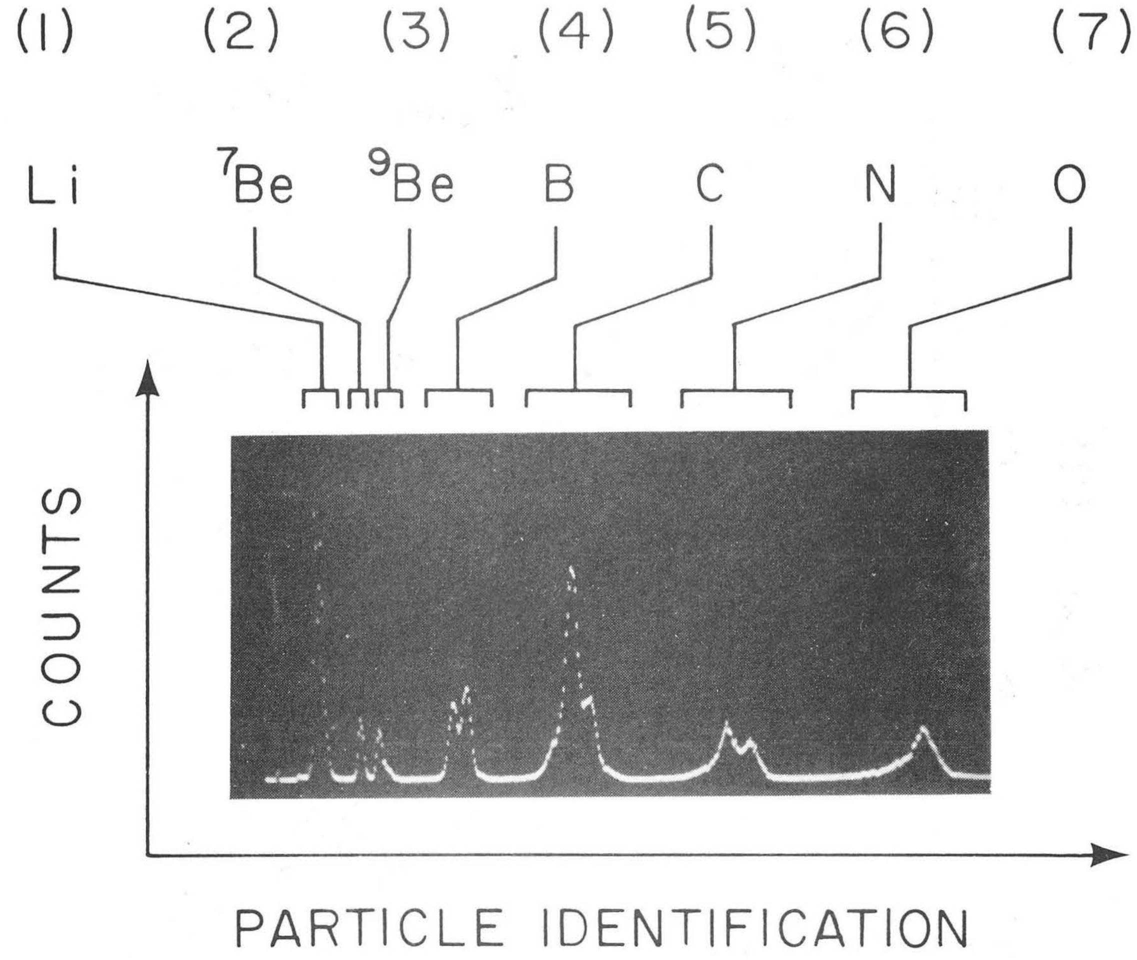

XBB812-2021

Fig. 45

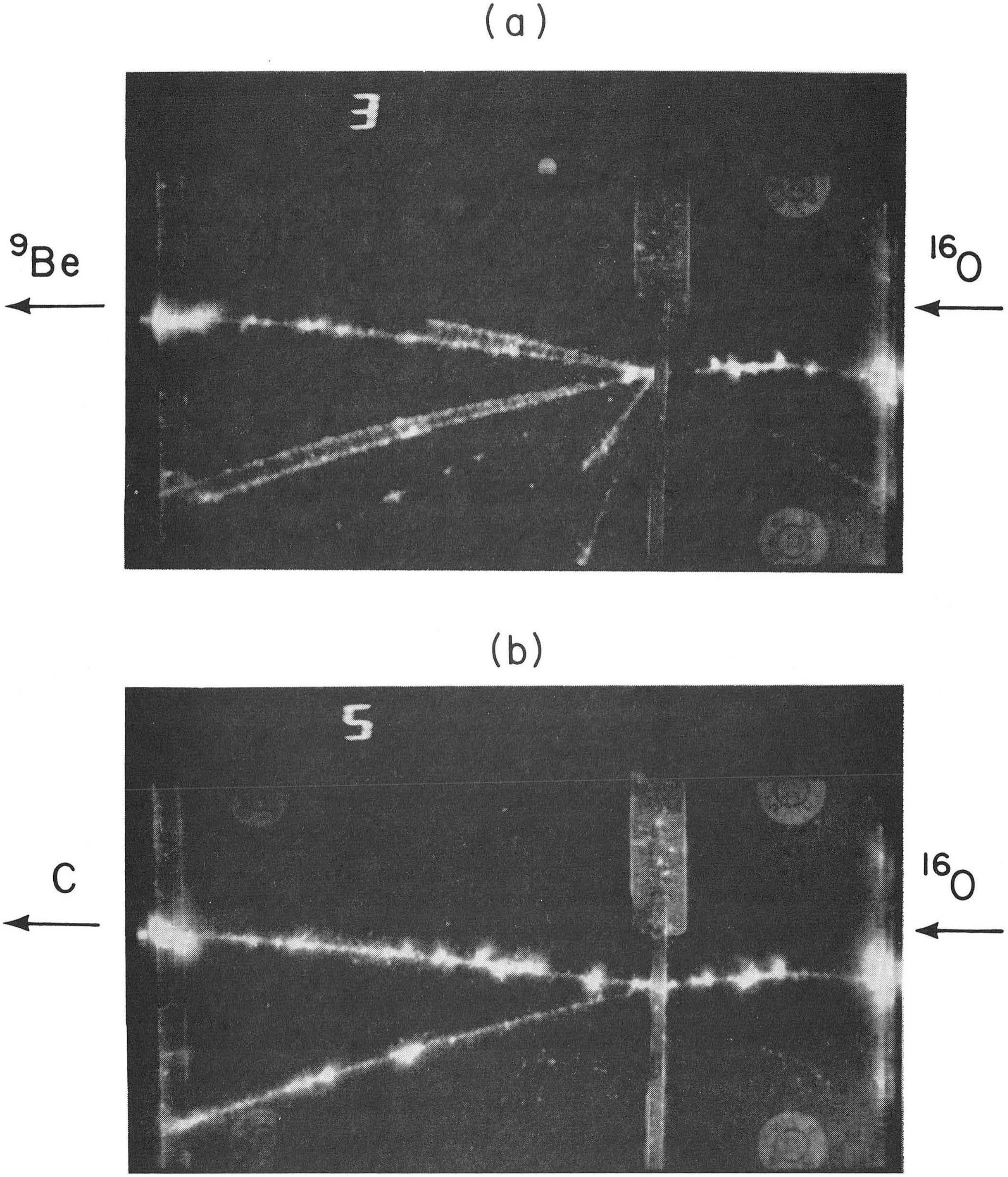

XBB812-2023

Fig. 46

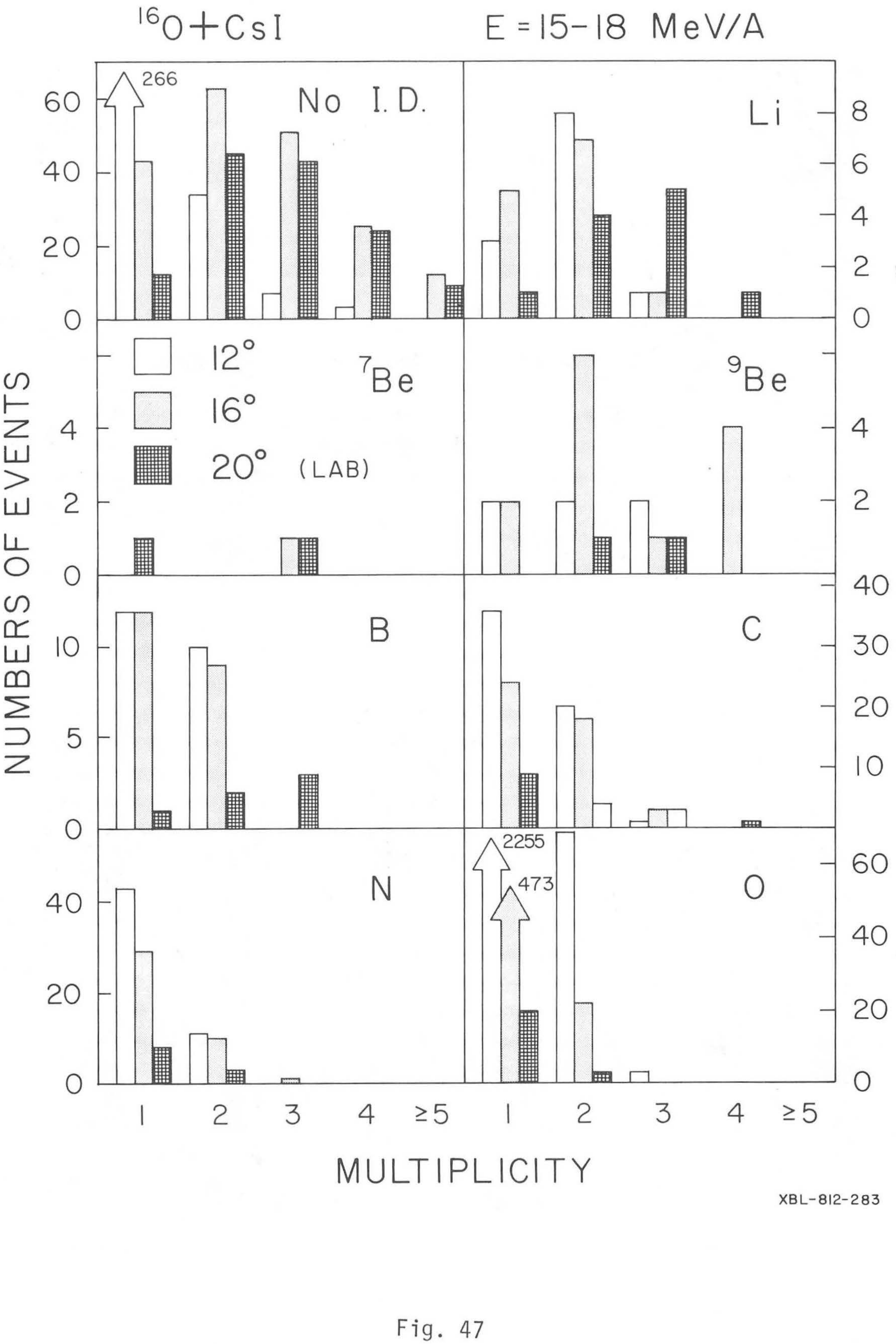
^{16}O+CsI
E = 15-18 MeV/A
No I.D.
266
Li
^{7}Be
^{9}Be
12°
16°
20° (LAB)
B
C
N
O
2255
473
NUMBERS OF EVENTS
MULTIPLICITY
1
2
3
4
≥5
0
20
40
60
2
4
6
8
5
10
30
XBL-812-283

Fig. 47

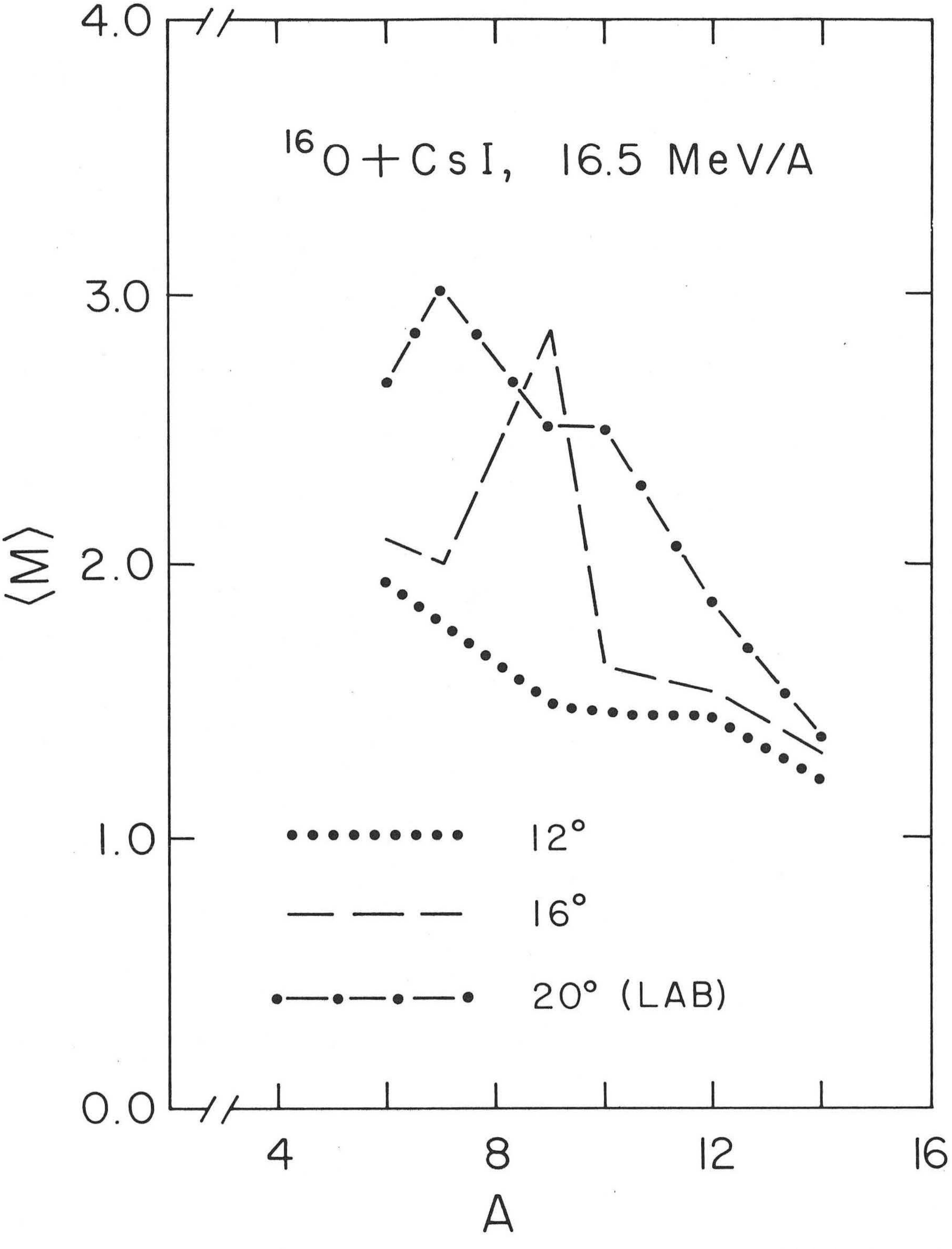

XBL-812-280

Fig. 48

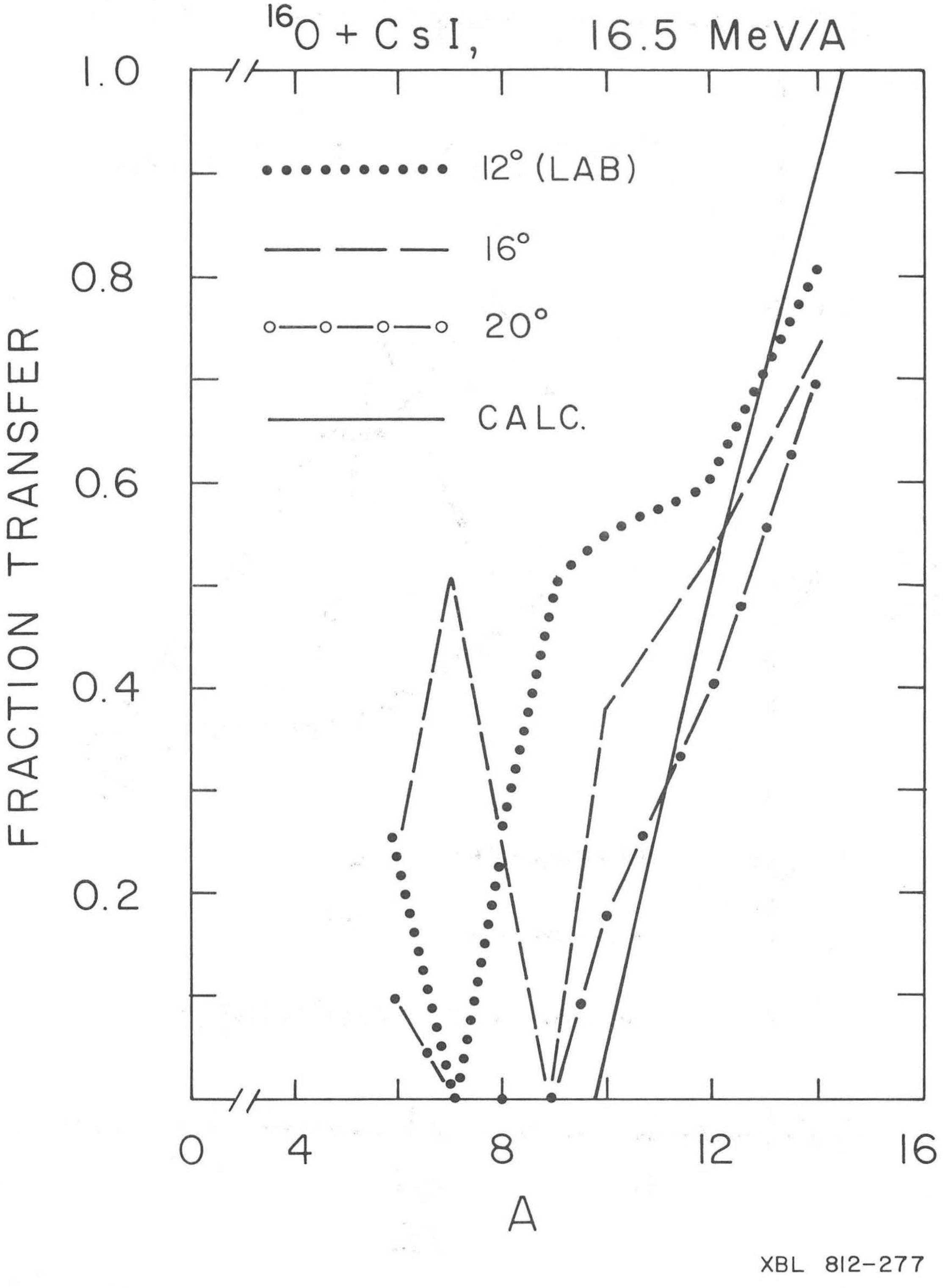

^{16}O + CsI, 16.5 MeV/A
1.0
0.8
0.6
0.4
0.2
FRACTION TRANSFER
12° (LAB)
16°
20°
CALC.
0
4
8
12
16
A
XBL 812-277

Fig. 49

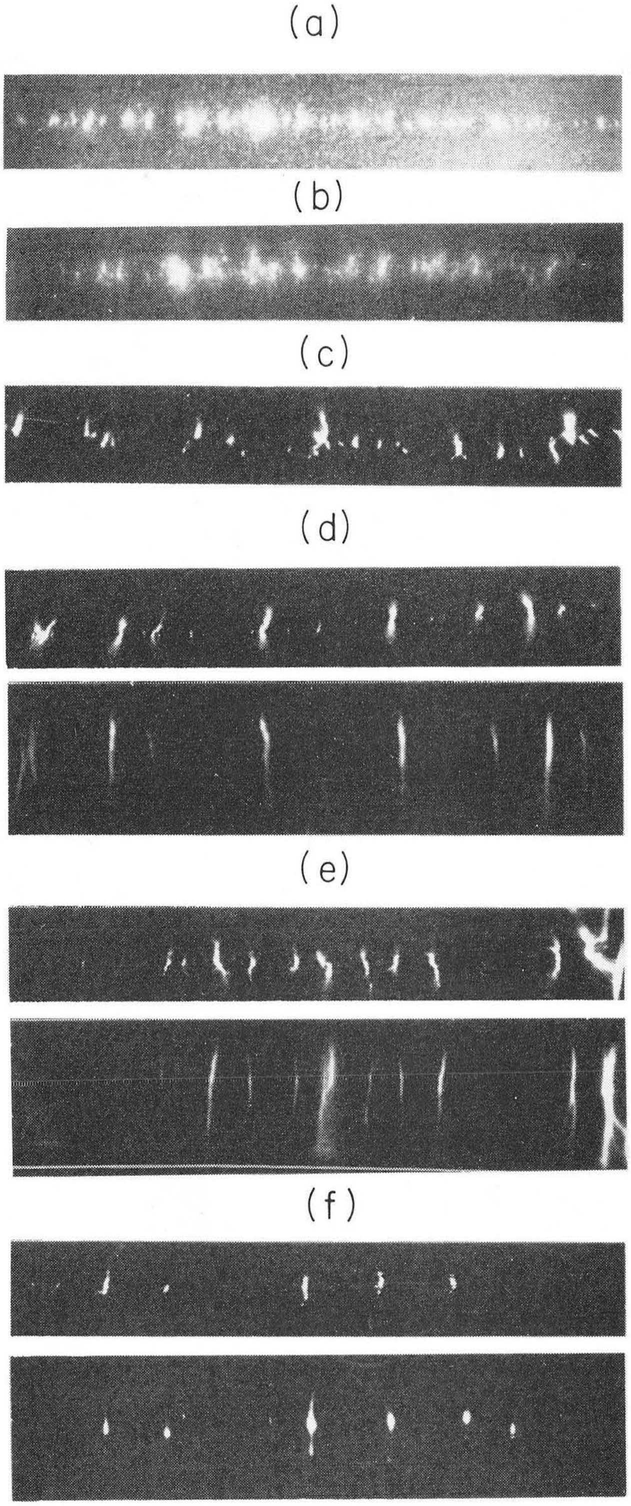

XBB790-13563

Fig. 50

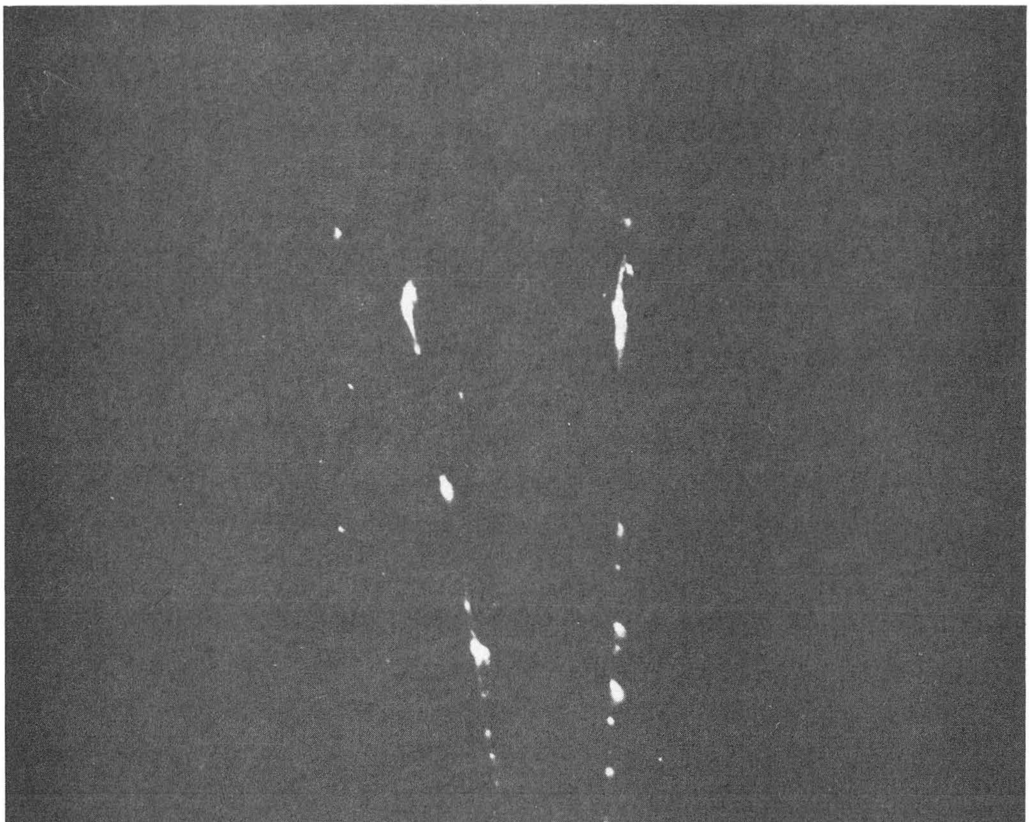

XBB799-12806

Fig. 51

TECHNICAL INFORMATION DEPARTMENT
LAWRENCE BERKELEY LABORATORY
UNIVERSITY OF CALIFORNIA
BERKELEY, CALIFORNIA 94720